Measurements and modeling of air and heat flow in a brick wall cavity

Christopher Hannan

A thesis

In

The Department

of

Building, Civil and Environmental Engineering

Presented in Partial Fulfillment of the Requirements
For the Degree of Master in Applied Science at
Concordia University
Montreal, Quebec, Canada

August 2007

Your file Votre référence
ISBN: 978-0-494-34746-1
Our file Notre référence
ISBN: 978-0-494-34746-1

ABSTRACT

Measurements and modeling of air and heat flow in a brick wall cavity

Christopher Hannan, M.A.Sc.

Rain screen wall systems are effective for control of rain water. The ventilation in the air space of such walls is also expected to play a role in the drying of cladding and control of vapor flows through the wall. For example, wet cladding exposed to solar radiation may subject the wall to inward vapor flow, unless an air cavity short-circuits that vapor flow. Although the role of the air cavity has been previously studied, it is relevant to evaluate more quantitatively the movement of air within the air cavity between the cladding and the backwall.

The effect of wind pressure notwithstanding, convective movement of air in the cavity is the result of buoyancy. Air movement can result from the increased temperature of the cladding due to solar radiation. The first objective of this thesis was the development of a numerical model of air movement driven by the variation of wall temperature with height, taking into account heat transfer by conduction, convection and radiation and mass transfer by diffusion and convection. The model was validated by means of comparison with analytical results from the literature, as well as with two sets of experimental results. The experimental procedures involved the evaluation of the magnitude and direction of the air movement within a large-scale cavity with a uni-directional anemometer and with particle image velocimetry. Once the boundary conditions were known, they were used to determine experimentally the mass transfer coefficients at the surface of wetted brick in the cavity with a horizontal wind tunnel setup. The validated model was used to evaluate parametrically the air movement's effects on heat and moisture flow within the assembly, assuming the brick had wetted by rain water before exposure to the solar radiation. Conclusions were drawn as to the effect of the air movement on the evacuation of heat and moisture from the assembly, based on variation of six parameters.

It was found that the air movement in the cavity plays a significant role in the drying of the cladding by saturation of rain water. As well, under average summer conditions for Montreal, the air velocity in the cavity was found to have an approximate peak of 0.20 m/s, neglecting the effects of wind pressure. The air flow is turbulent at the weephole entrance of the cavity, before becoming laminar within approximately 10 centimeters of flow development. Finally, convective mass and heat transfer surface coefficients increase with air velocity, except for air velocities lower than 0.10 m/s.

ACKNOWLEDGMENTS

I would be remiss not to first thank my supervisor, Dr. Dominique Derome, for her constant support and dedication to my cause. I would never have believed I could have achieved so much without her calm, direct manner leading the way, nor her exemplary salesmanship to convince me this was the path for me in the first place. I add to her voice those of the faculty of Building Engineering, who all had a role to play in helping me achieve my goals in both my Bachelor's and Master's degrees. As I prepare for new challenges in my life, their selfless impartment of knowledge are the reminders of the journey traveled and an outstanding academic program in Building Engineering at Concordia University.

This thesis would not have been possible without the invaluable contributions of a number of people. To Joe Hrib and Rocco Lombardo, whose technical expertise and quality workmanship made for smooth scientific experiments. To Dr. Kamran Siddiqui for the loan of his PIV equipment. To Dr. Hans Janssen, who reminded me that there is indeed always more than one way of reaching a goal. To Adam Neale, whose encyclopedic knowledge of almost everything building envelope enlightened me. To Jason Edelstein, whose friendship and perseverance inspired me. To Marianne Berube-Dufour, Maher Ben Ali and Damien Courbe, whose work behind the scenes was so helpful when it was clear my two hands would not be nearly enough. To my parents, whose unwavering support and pride in my undertakings is always a source of strength in my life. To my siblings and friends, who have always been there when I needed them the most and who taught me not to take myself too seriously. To my wife Shannon, whose advice, love and laughter are more valuable to me than she will ever know. Finally, to my daughter Charlotte, whose pending arrival would be all the motivation I would need to finish. Thank you all.

Table of Contents

List of Tables

List of Figures

Nomenclature

Symbols :

A	elemental area	[m^2]
C	thermal coefficient matrix	
G	moisture coefficient matrix	
I	irradiation component	[W]
L	length	[m]
Nu	Nusselt number	
P	air pressure	[Pa]
Pr	Prandtl number	
R	known thermal value matrix	
R_1	thermal resistance between the cavity and the exterior	[m^2K/W]
R_2	thermal resistance between the cavity and the interior	[m^2K/W]
Re	Reynolds number	
S	storage term	
S	known moisture value matrix	
T	temperature	[K]
V	volume	[m^3]
Y	aerodynamic losses in the cavity	
c_p	specific heat	[J/kgK]
d	diameter	[m]
dm	numerical day of the year	[day]
f	friction factor	
g	vapor flow rate	[kg/m^2]
h	heat transfer coefficient	[W/m^2K]
h	hour angle	[rad]
j	nodal position in x-direction	
k	nodal position in y-direction	
k	thermal conductivity	[W/mK]
lat	latitude	[rad]
p	partial vapor pressure	[Pa]
q	heat flow rate	[W]
r	location factor	
t	time	[s]
v	velocity	[m/s]
x	x position (horizontal)	[m]
y	y position (vertical)	[m]
z	z position (depth)	[m]
z	zenith angle	[rad]

Greek Letters :

α	solar altitude	[rad]
β	tilt angle	[rad]
γ	surface solar azimuth	[rad]
σ	Stephen-Boltzman constant, 5.67×10^{-8} W/m^{2}K^4	
δ	permeability	[kg/s m Pa]
δ	declination angle	[rad]
ε	emissivity	
ξ	moisture capacity	[kg/kg]
ξ	factor of local loss	
ρ	density	[kg/m^3]
θ	temperature	[K]
θ	incidence angle	[rad]
Φ	relative humidity	[%]
Φ	solar azimuth	[rad]
τ	transmittance	[%]
μ	vapor permeability	[ng/Pa.m.s]
ψ	surface azimuth angle	[rad]
ν	kinematic viscosity	[m^2/s]

Indices / Exponants :

∞	top extremity
a	air
avg	average
b	beam direct
cav	cavity
cd	conduction
cv	convection
dg	ground reflected
ds	transmited
e	exterior
H	hydraulic
i	time step in x direction
j	time step in y direction
L	section length
m	mass
on	extra-terrestrial
r	radiation
s	surface
sat	saturation
surf	surface
t-1	previous time step
v	vapor

Chapter 1: Introduction

1.1 Problem Statement

Although cladding systems have been increasingly used since the development of wood frame structures, the conscious integration of rainscreen cladding to building envelopes of residential buildings is more recent. Rainscreens allow effective control of rain and also management of moisture through the building envelope, thus preventing the deterioration of its moisture sensitive constituent materials. Rain control is achieved by the capillary break resulting from the air space and proper water deflection measures (e.g. flashing). In addition, to prevent air pressure differences across the cladding, openings in the cladding have been proven necessary. Depending on the size of the openings, such systems are considered pressure equalized or ventilated.

The effect of wind pressure notwithstanding, convective movement of air in the cavity is due to buoyancy, for example, as the result of the increased temperature of the cladding due to solar radiation. As the air makes contact with the heated interior side of, say, a brick cladding, it is itself warmed and its change in density causes it to rise. The upward moving air leads to fresh outdoor air to be drawn into the bottom weepholes, travel through the cavity, and be released through the upper weepholes. This air movement is said to have the effect of evacuating both heat and moisture from the air cavity, thus reducing the effects of vapor flow across the cavity. Although coupled heat, air and moisture transfer within building envelopes, as well as the role of the air cavity in such wall assemblies has been studied seriously for 50 years, the exact conditions of the air movement in the cavity and the parameters affecting this air movement are not completely known. This project looks at documenting qualitatively and quantitatively the air movement in terms of velocities and type of flow. Once the boundary conditions are clearly defined, an experimental procedure reproducing these conditions can lead to the appropriate determination of heat and mass transfer convective transfer coefficients for the surfaces facing the air cavity.

This study also includes the effect of air movement on the overall hygrothermal behavior of the assembly. The motivations for this study are two-fold. First, from a scientific perspective, this project aims to understand better the movement of air within enclosed spaces as an application of driving potentials and buoyancy, and the interface conditions of the air and the porous materials. Second, from an engineering perspective, a greater understanding of air movement within the cavity can lead to improvement in the design and construction of rainscreens.

1.2 Scope of the Work

This study involves the evaluation of air movement within the air cavity of a one-storey wood-frame residential building with brick cladding and a rainscreen system. This is typical for low-rise buildings such as bungalows.

The study specifically observes air movement due to buoyancy. While wind pressure also has significant effects on this air movement, the variations of air pressure due to wind are quite complex to take into account, unlike other boundary conditions such as outdoor temperature and solar radiation which are easily predictable and may be simplified into sinusoidal functions. Therefore, wind will not be considered except for a simplified parametric analysis in Chapter 7.

The scope of the project involves the evaluation of the temperature and relative humidity profiles within the wall assembly and the determination of the air velocity profile in the air cavity. As well, transfer of heat and moisture to the air at the inside surface of the brick cladding will be studied.

The objectives of the project are:

- to develop and validate a numerical model of air movement in a cladded wall, including heat, air and moisture transports
- to measure the air movement in a large-scale test set-up for validation of the developed model

- to measure the mass transfer convective coefficients for the conditions of the large-scale setup to include in the model.
- through a parametric analysis using the validated model, to determine the effect of certain factors on the air movement in the cavity.

1.3 Methodology

The first step of this project was the development of a control volume model that calculates air movement driven by the air pressure gradient between the top and bottom of the cavity, as well as heat transfer by conduction, convection and radiation, and also mass transfer by diffusion and convection. Once developed, this model was used to evaluate the air movement's effects on moisture flow within the assembly, assuming the brick had been quasi-saturated with rain water before exposure to the solar radiation. For verification of the model, a comparison with analytical results from the literature was done and a qualitative comparison with an on-going CFD study was also performed. Then, the model was validated using the results of large-scale experiments where air movement was determined with an anemometer experiment and, then, by means of particle image velocimetry (PIV). Finally, using the known boundary conditions, the mass transfer coefficients at the surface of wetted brick in the cavity were evaluated by using a horizontal wind tunnel setup to measure appropriate coefficients. A parametric analysis using the validated model looked at the effects of the thickness of the air cavity, the emissivity of the backwall, the initial moisture content in the brick, the intensity of the solar radiation incident on the wall, the size of the weephole vents and wind pressure. Conclusions are made as to the accuracy and applicability of results.

1.4 Outline

The study is subdivided into eight chapters. Findings from previous chapters are applied to further knowledge in the following ones.

In Chapter 2, the literature pertaining to the problem statement is reviewed. More specifically, a general overview is performed by observing the function of the building envelope and the use of air cavities. Next, basic theory and equations in heat and moisture transfer, as well as air movement within the cavity, are reviewed. Finally, previous experimentation in the fields of air flow characteristics, driving influences of air flow, wind pressure effects, ventilation drying and air movement models are discussed.

In Chapter 3, the development of the model is presented. This includes the definition of the functionalities of the model, the description of the physical system represented by the model and an introduction to control volume modeling theory. This is followed by the procedure of calculation for the heat transfer, cavity air velocity and moisture transfer in the wall network Two application examples of the model are performed. The chapter concludes with tables of results provided by the model.

Chapter 4 presents two verification projects for the model. The first involves a comparison of the results of the temperature profile in the cavity to those obtained via an analytically-derived equation from the literature. This is followed by comparison with experimental results of cavity air velocity measured with an anemometer. .

Chapter 5 presents a large-scale model validation experimental study using particle image velocimetry (PIV). The principles of PIV are explained. This is followed by discussion of the experimental setup, procedure and the limitations of the experiment. Finally, results and discussion of the images and air velocity readings are presented.

Chapter 6 discusses an experimental study aimed at a better understanding of mass transfer surface coefficients with a wind tunnel setup. The basic theory behind the determination of the convective heat and mass transfer coefficients is

presented. The experimental setup, procedure and limitations of the experiment are explained. The chapter ends with the analysis of the results.

Chapter 7 presents a parametric analysis of the results generated by the numerical model described in chapter 3. Six basic parameters are varied, and the resulting effects on air velocity in the cavity and the temperature and relative humidity profiles of the wall assembly are documented. An analysis of the results is conducted and conclusions are drawn.

Chapter 8 provides a summary of the findings of the previous chapters, and allows for a summative final analysis to take place. Specific contributions to the research and recommendations for future work are discussed.

Chapter 2: Literature Review

This chapter presents an overview of the literature pertaining to the problem statement. Firstly, a brief review of the functions of the building envelope and a brief description of climatic loads are presented. Secondly, the theory and equations available to calculate heat transfer in a building wall assembly are discussed. This is followed by a review of the theory and equations pertaining to moisture transfer. Fourthly, a state-of-the-art review is performed on air movement in vertical cavities. Finally, previous experiments in the field of cavity air movement are presented.

2.1 General Overview

In this section, the functions of the building envelope in modern residential buildings are presented. The building envelope is defined as the set of walls, roof, windows, doors, etc, that delimits the inside of the building.

2.1.1 Functions of the Building Envelope

The main purpose of the building envelope is to provide a barrier between the outside and inside environment, allowing interior conditions to be controlled to allow optimal comfort for occupants. Hutcheon (1953) lists the several roles the building envelope should fulfill, including controlling heat flow, air flow, light, noise, fire, and rain penetration, among others. The modern brick cladding (single layer masonry) for wood-frame wall assembly was developed mainly for controlling rain penetration. Kumar (1998) states that the air space placed between the cladding and backwall has dual purposes. Firstly, it reduces the wind-induced air pressure differential across the brick cladding, and displaces it to be across the wood-framed backwall, and consequently where no rain water may be present. Secondly, it allows moisture, eventually driven inward through the porous brick, to be evacuated at the bottom of the wall via a drip pan and

weepholes. As such, the cladding acts as a rainscreen, as can be seen in figure 2.1.

A traditional cold-climate residential wall assembly can be composed of:

1. Cladding - e.g. wood shingles, brick, PVC, aluminum siding, etc;
2. Air space;
3. Sheathing and weather resistive membrane; e.g. oriented strand board with spun-bonded polyolefin membrane;
4. Wood studs and glass fiber insulation;
5. Interior finishing and vapor control layer – e.g. painted gypsum board and polyethylene membrane.

Components 3, 4 and 5 make up the back wall. In a brick cladding, the air cavity width may vary from 25 to 40 mm. Vertical joints are left open between every second or third brick in the bottom row of the wall to form weepholes. Similarly, openings in the top of the cladding are vents.

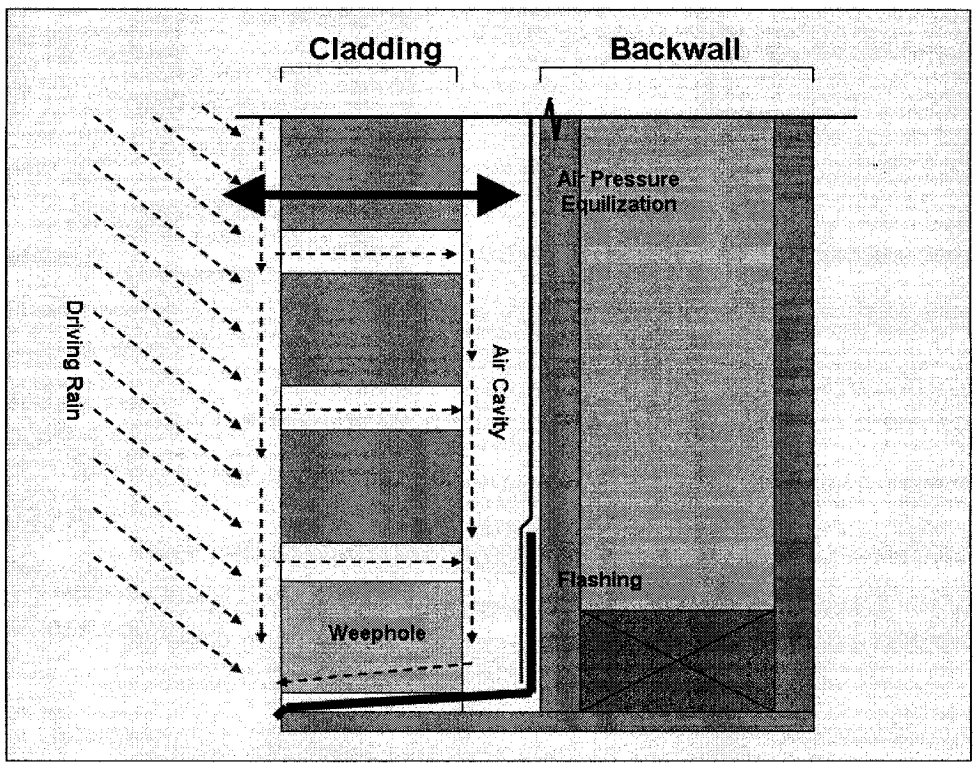

Figure 2.1: Brick-cladded wood frame wall with cladding acting as a rainscreen

2.1.2 Climatic loads and resulting driving potentials

Hutcheon also describes many factors that influence the construction of the building envelope. The geographical location plays perhaps the most important role, as this determines the air temperature (both outdoor and indoor), relative humidity of the air (outdoor vs indoor), air pressure acting on the envelope (outdoor – wind, indoor – stack effect, HVAC), the rain load and the intensity of solar radiation, among others. For example, a building envelope in a tropical climate such as Tampa, Florida, should be designed to sustain the conditions resulting from high relative humidity and outdoor temperature, while one in Edmonton, Alberta will require more consideration for a wide variety of temperatures and relative humidity to provide comfort and durability through four seasons. The aforementioned factors result in driving potentials for heat and moisture transfer through the wall assembly, from areas of high temperature or RH to areas of low temperature or RH.

2.2 Heat Transport

The following is a review of the theory and equations describing heat transfer in terms of conduction, convection and radiation. Kreith (2001) states that, as the three aforementioned processes are relatively independent from one another, the sum of their effects has been demonstrated to accurately describe the transfer of heat in a controlled environment. Thermal storage of building materials is also discussed.

2.2.1 Thermal Conduction

Elementary theory in heat flow by means of conduction is derived from the work of Joseph Fourier (1768-1830) whose study in heat transfer yielded Fourier's Law. This equation is generally accepted to represent heat flow by conduction in any direction.

$$\frac{dq}{dt} = -kA\frac{dT}{dx} \tag{2.1}$$

In this equation, *dq/dt* is the rate of heat flow [W], *A* is the area transverse to the flow [m^2], *dT/dx* is the temperature gradient [°C], and *k* is the coefficient of thermal conductivity [W/m°C]. The negative sign indicates the direction of flow with respect to dT/dx; as such, it is crucial to observe a sign convention established to ensure accuracy of results.

2.2.2 Thermal Convection

Thermal convection takes place when a solid surface in contact with a fluid results in heat transfer from one to the other, provided that the movement of the fluid due to its changes in density is unrestricted. Convective heat transfer coefficients, h_{cv}, are thus defined to describe this phenomenon, as per equation 2.2. For simplicity, it is common to define convective heat transfer coefficients to include the long-wave radiation exchange between the surface and the surroundings. Hutcheon and Handegord (1995) refer to said values to be 8.3 and 34 W/m^2K for interior and exterior facades, respectively, under normal conditions.

$$q_{cv,i} = h_{cv} A(T_s - T_{i/e}) \tag{2.2}$$

In this equation, q_{cv} represents the convective heat transfer [W], h_{cv} is the convective heat transfer coefficient [W/m^2K], T_s is the temperature of the solid surface [°C] and $T_{i/e}$ is the bulk temperature of the fluid [°C].

2.2.3 Thermal Radiation

Radiative exchange is proportional to the fourth power of the temperature of the emitting bodies. Two cases of heat transfer by thermal radiation are considered later in the thesis, radiation exchange between the two surfaces of the cavity and solar radiation on the outside surface of the brick cladding.

Within the cavity, the radiation exchange between the interior surface of the brick and the cavity surface of the backwall are significant contributors to the heat

transfer in the system. In order to calculate this phenomenon, equation 2.3 may be used. Due to the complexity of manipulating temperatures of the fourth power, equation 2.4 presents a linearized version of equation 2.3.

$$q_{r,i} = \frac{A \cdot \sigma \cdot (T_{surf1}^4 - T_{surf2}^4)}{\frac{1}{\varepsilon_{surf1}} + \frac{1}{\varepsilon_{surf2}} - 1} \tag{2.3}$$

$$q_{r,i} = h_r \cdot A \cdot (T_{surf1} - T_{surf2}) \tag{2.4}$$

The radiative heat transfer coefficient h_r *[W/m^{2}K]* from equation 2.4 may be calculated via equation 2.5, which makes use of the average temperature in the cavity.

$$h_r = \frac{4 \cdot \sigma \cdot T_{avg}^{\ 3}}{\frac{1}{\varepsilon_{surf1}} + \frac{1}{\varepsilon_{surf2}} - 1} \tag{2.5}$$

In the preceding formulae, q_r represents the heat transfer due to radiative exchange [W], A represents the area of the facing walls [m^2], σ is the Stephen-Boltzmann constant [5.67 x 10^{-8}], ε represents the dimensionless emissivities of the two facing surfaces, T the surface temperatures of the facing walls and T_{avg} the average temperature of the cavity wall surface [K].

Solar radiation only affects the nodes of the exterior surface of the brick. A full description of the calculation method for solar radiation is taken from Athienitis (1993) and is described in Appendix A. The instantaneous solar radiation, $I_t(t)$, that is incident on the brick wall may finally be defined as the total of its three constituent components, as per equation 2.9. It is expressed in [W] and is dependent on the time, t.

$$I_b(t) = I_{on} \cdot \tau_b(t) \cdot \cos(\theta(t)) \tag{2.6}$$

$$I_{dg}(t) = I_{on} \cdot \sin(\alpha(t)) \cdot (\tau_b + \tau_d) \cdot SR \cdot \frac{1-\cos(\beta)}{2} \quad (2.7)$$

$$I_{ds}(t) = I_{on} \cdot \sin(\alpha(t)) \cdot \tau_d \cdot \frac{1+\cos(\beta)}{2} \quad (2.8)$$

$$I_t(t) = I_b(t) + I_{ds}(t) + I_{dg}(t) \quad (2.9)$$

In the preceding equations, $I_b(t)$ is the radiation caused by the rays directly incident on the wall [W], $I_{dg}(t)$ is the ground reflected component [W], $I_{ds}(t)$ is the diffuse sky radiation [W], I_{on} is the extraterrestrial solar radiation [W], $\tau_b(t)$ is the transmittance for beam radiation, $\tau_d(t)$ is the transmittance for diffuse radiation, $\theta(t)$ is the incidence angle [rad], SR is the reflection ratio taken to be 0.32, $\alpha(t)$ is the solar altitude [rad] and β is the wall tilt angle, taken to be π/2 radian for a vertical wall.

2.2.5 Thermal Storage

Janssens (1998) defines the change of thermal storage of building materials (including air layers between materials) by equation 2.10.

$$\frac{dS}{dt} = \rho c_p V \frac{dT}{dt} \quad (2.10)$$

In this equation, S is the thermal storage [J], ρ is the density of the material [kg/m^3], c_p is the specific heat capacity of the material [J/kgK], V is the volume of the medium [m^3], Δt is the time step [seconds], T is the temperature of the material [°C].

2.3 Moisture Transport

Moisture transfer can be considered to be analogous to heat transfer (Janssens, 1998), as heat transfer variables are replaced by the corresponding variables for vapor transfer. It must be noted that, unlike heat transfer, material properties, e.g. vapor permeability, are not constant but vary with the relative humidity, or moisture content, in the material. Moisture transfer is considered in three distinct sections: diffusion, convection and storage.

2.3.1 Moisture Diffusion

The moisture in the material moves depending on the permeability of the materials under vapor pressure difference. This process is analogous to thermal conduction and follows Fick's Law, and can be expressed as equation 2.11.

$$g_{v,i} = A\mu(\phi)\frac{\delta p}{\delta x} \tag{2.11}$$

Here, $g_{v,i}$ is the mass of vapor transferred over unit time [ng/s·m^2], A is the area of contact [m^2], $\mu(\phi)$ is the vapor permeability of the medium as a function of relative humidity [ng/Pa·m·s], p is the vapor pressure of the medium [Pa] and x is the flow path [m].

2.3.2 Moisture Convection

Moisture transfer by convection can be defined based on equation 2.2 to form equation 2.12. This represents the transfer of moisture at the interface of solid and air.

$$g_{cv,i} = h_m A(p_{v,s} - p_{v,air}) \tag{2.12}$$

In this equation, $g_{cv,i}$ is the mass of vapor transferred over unit time [ng/s·m^2], $p_{v,s}$ is the vapor pressure at the surface of the solid material [Pa], and $p_{v,air}$ is the bulk vapor pressure of the air [Pa]. The convective moisture transfer coefficient, h_m, expressed in [s/m], will be discussed in section 2.4.4.

2.3.3 Moisture Storage

Moisture storage is defined to be the retention of moisture in a material after or during transport by diffusion or convection. The resulting moisture content is a function of the relative humidity and is expressed with a sorption isotherm, determined at steady state conditions. The slope of the isotherm is the capacity of moisture storage of the material, $\xi_i(\phi)$. The change of moisture storage is defined in equation 2.13 (Janssens, 1998).

$$\frac{dS}{dt} = \frac{\rho_i \xi_i(\phi) V}{p_{v,sat}} \frac{dp_v}{dt} \tag{2.13}$$

In this equation, S is the thermal storage [J], ρ is the density of the material [kg/m^3], $\xi_i(\phi)$ is the specific moisture capacity [kg moisture/kg material], V is the volume [m^3], t is time [seconds] and p_v is vapor pressure [Pa] and $p_{v,sat}$ is the saturation vapor pressure [Pa].

2.4 Air Transport in the Cavity

This project looks at air movement in the air space between the cladding and the back wall. Other types of air movement, like unintentional air movement through cracks and joints in the envelope, are not discussed here as the backwall is considered airtight. In this section, first, the difference between natural and forced convection is reviewed. Next, methods of calculation of cavity air velocity and pressure losses within the air flow path are presented. The theory behind the surface convective transfer coefficients is discussed, and finally the equations for heat and mass transport within the cavity are presented.

2.4.1 Natural and Forced Convection

While thermal convection has been defined in section 2.2.2, it is necessary to differentiate between the processes of natural and forced convection. Lienhard (2006) defines natural convection to occur when the effects of buoyancy cause a fluid to displace itself while in contact with a warmer or colder surface. In this case, the heat transfer coefficient, h_{cv}, can be defined as a function of the temperature difference of the two mediums. However, when fluid is forced over a surface by an exterior force as with wind, this may be defined as forced convection. Lienhard further states that in the second case, if the temperature difference is relatively small, h_{cv} is completely independent of temperature.

2.4.2 Air Velocity in Ducts

To determine the precise effects of the heated air passing over the interior surface of the brick on the overall temperature profile in the cavity, it is necessary to first calculate the velocity of the air in the cavity. To this end, Grau and Rode (2007) provide equation 2.14, which is intended to calculate the air velocity in tall cavities and ducts.

$$v_{cav} = \sqrt{\frac{|\Delta P_{cavity}|}{\frac{1}{2} \cdot \rho \cdot \xi_{total}}} \tag{2.14}$$

where v_{cav} is the air velocity in the cavity [m/s], ΔP_{cavity} is the air pressure difference between the top and bottom of the cavity [Pa], ρ is the density of the air [1.20 kg/m^3] and ξ_{total} are the total dimensionless losses experienced throughout the flow path. The full procedure for calculating the losses are shown in section 2.4.3.

Equation 2.15 indicates that the air flow is driven by the air pressure difference between the entrance and exit of the cavity. Grau and Rode state that this air pressure difference is due to both wind-induced pressure and the stack effect, which is the result of the buoyancy of the air. As this study does not consider the effects of wind, the air pressure difference may be calculated via equation 2.15. Air, including water vapor, can be assumed to behave as ideal gases, so the equation is based on the ideal gas law.

$$\Delta P_{cavity} = \rho_a \cdot R_a \cdot \Delta T \tag{2.15}$$

where ρ_a is the density of air [1.2 kg/m3], R_a is the gas constant for air [287.1 J/kgK], and ΔT is the temperature difference between the top and bottom of the cavity [K]. For calculation purposes, the temperature difference is taken at the inlet and outlet of the air flow path, which is located at the top and bottom of the exterior surface of the brick cladding.

2.4.3 Losses along Air Flow Path

Hens (2005) compiled a comprehensive work based on previous studies on the aerodynamic losses that the airflow experiences along a path. Two categories of losses exist within the air flow path: local and friction losses. Friction losses are due to the roughness of the surfaces over which the air passes. They may be calculated via equation 2.16. Local losses are due to air passing into and out of a tube, as well as when the path of the air flow is redirected at a given angle, as per equation 2.17. In order to accurately tabulate these losses, the air flow path must be subdivided into distinct tubular sections.

- Friction Losses: $\Delta P_a = f \frac{L}{d_H} \frac{\rho_a v_a^2}{2}$ (2.16)

- Local Losses: $\Delta P_a = \xi \frac{\rho_a v_a^2}{2}$ (2.17)

In the preceding equations, f is the dimensionless friction loss coefficient, L is the length of the path [m], d_H is the hydraulic diameter of the enclosure [m], ρ_a is the density of air, v_a is the velocity of air, and ξ is the dimensionless local loss coefficient. The loss coefficients may be tabulated by using tables B.1 and B.2 (see Appendix B). The two ΔP_a terms from equations 2.16 and 2.17 are identical to the ΔP_{cavity} term from section 2.4.2. As such, the equations provided to calculate the cavity velocity corroborate each other; in both cases the cavity air velocity is expressed as the square root of the driving air pressure divided by the losses along the flow path.

2.4.4 Non-dimensional Analysis for Convective Transfer Coefficient Determination

As the full procedure for calculating the cavity air velocity has been established in sections 2.4.2 and 2.4.3, it is now relevant to use the velocity as a means of determining the convective thermal and moisture transfer coefficients. Firstly, the heat transfer coefficient h_{cv} [W/m^{2}K] must be determined by the Dittus-Boehler correlation, as shown in the following:

$$h_{cv} = \frac{Nu_L L}{k_a} \tag{2.18}$$

where Nu_L is the localized Nusselt number, a dimensionless number which indicates the ratio of convective heat transfer to the conductive heat transfer that would have occurred under the same conditions., L is the length of the flow path [m] and k_a is the thermal conductivity of air [W/m°C].

Kreith (2001) defines several correlations of the Nusselt number, which depend on the orientation of the fluid flow, the geometry of the surface and other factors. The applicable equation for laminar flow is the following:

$$Nu_L = 0.023 \cdot \mathrm{Re}_c^{0.8} \cdot \mathrm{Pr}^{0.4} \tag{2.19}$$

Here, *Pr* is the Prandl number, which indicates the ratio of momentum diffusivity and thermal diffusivity. For air and most other gases, its value is considered to be 0.7. Re_c is the Reynolds Number, which describes the ratio of inertial to viscous forces acting within a fluid (which determines whether a fluid flow can be defined as laminar, transition or turbulent). Re_c may be expressed by the following equation:

$$\mathrm{Re}_c = \frac{v_a \cdot d_H}{\upsilon_a} \tag{2.20}$$

where v_a is the velocity of the air [m/s], d_H is the hydraulic diameter of the space [m] and υ_a is the kinematic viscosity of air [14.5×10^{-6} m^2/s]. Once the coefficient of heat transfer by convection has been established, the coefficient of moisture transfer [s/m] by convection may be calculated. It is defined by a variation of the Chilton-Colburn analogy (1934), equation 2.21.

$$h_m = \frac{\delta_a(T)\ h_{cv}}{k_a} \tag{2.21}$$

where δ_a is the vapor permeability of air as a function of temperature (1.87×10^{-10} s at 20°C), h_{cv} is the convective heat transfer coefficient [W/m^{2}K], and k_a is the thermal conductivity of the air [W/m°C].

2.4.5 Heat and Moisture Transport by Air Movement

The average air velocity in the cavity having been determined, the heat transfer by air movement [W/m^2] may follow. Working on lightweight roof systems, Janssens (1998) produced a comprehensive review of calculation and assessment methods. He includes heat transfer by air movement in cavities as defined by equation 2.22.

$$\frac{q_{m,j}}{L} = \rho_a c_a d_H v_a (T_{j-1} - T_j) \tag{2.22}$$

where L is the length of heat transfer on the cavity wall [m], ρ_a is the density of the air, c_{pa} is the specific heat capacity of air, d_H is the hydraulic diameter of the cavity (for two infinite parallel planes distanced by 25 mm), v_a is the velocity of the air and T is the temperature at the present and previous location of the air flow [°C]. This equation may also be applied for movement of air within the vents at the top and weepholes at the bottom of the brick cladding, except that the equation for mass transport in the openings is now expressed in the x direction. Janssens states that it is important to strictly adhere to a sign convention in order to ensure accuracy as the vents will undergo the opposite air flow direction effects of the weepholes. The movement of air within the vertical cavity and horizontal weepholes and vents may be visualized in figure 2.2. Janssens maintains that his equations apply for a single location at the center of the air space; as such, only one control volume is considered in the horizontal direction for the cavity and in the vertical direction for the openings despite the non-uniformity of the air flow in both cases.

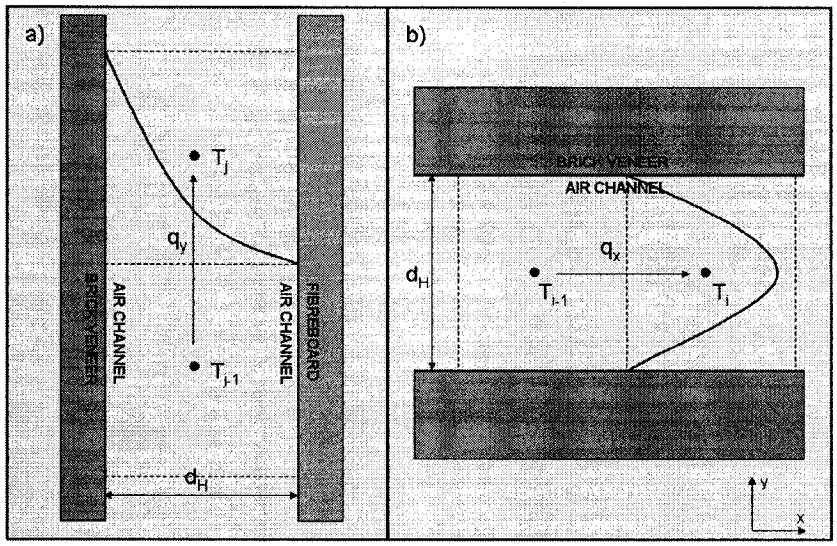

Figure 2.2: Schematic representation of the temperature profile in the a) air cavity and b) weepholes

Moisture transport by air movement in the cavity and weepholes is analogous to equation 2.22, forming equation 2.23.

$$g_{m,j} = \rho_a \xi_a v_a (P_{j-1} - P_j) \tag{2.23}$$

The term ξ_a refers to the moisture capacity for air, which is assumed to be constant at 6.1 x 10^{-6} kg/kg/Pa, while *P* refers to the vapor pressure at the present and former locations of the air flow [Pa].

2.5 Past Experimentation in Cavity Air Movement

Many field and laboratory studies have been accomplished in the field of airflow within brick cavity walls. However, few have fully evaluated the specific situation of the effects of air movement on the drying of wall assembly cladding. This section reviews past experimentation that has a bearing on this study. Firstly, studies on the characteristics of air flow are presented. Next, experimental research pertaining to the driving potentials that induce air flow are discussed, followed by specific studies on wind pressure on brick cavity walls. A state-of-the-art on ventilation drying is presented and finally some existing models and computational methods are presented.

There has been much debate within academic circles as to the merits of cavity ventilation. Most academics and industry observers contend that venting the cavity allows for the evacuation of moisture that may be brought in via rain water pressure, vapor diffusion or other means (TenWolde 1992). However, some believe that venting a cavity can lead to ice formation due to undercooling and thus deterioration of the wall assembly during certain wintertime conditions, as Zheng (2003) determined, however this was primarily found in roof cavities. There are therefore conditions under which cavity ventilation may be beneficial, and others under which it may be less so.

2.5.1 Air Flow Characteristics

Straube *et al.* (2004) completed a research report on the performance of sheathing membranes for ASHRAE in which a review of the theory and mechanics of air flow in rainscreen walls is presented. Among their findings, they developed equations and schematic representations to represent the path of air as it passes through the cavity. Figure 2.3 displays the trajectory of air through the cavity, where the terms *w* and *h* refer to the width and height of the weephole/vent openings, respectively. Their findings seem to indicate that, as air passes through the lower weepholes, the path widens and spreads to approximately the halfway point between the openings, then air travels through the cavity and exits through the vent opening. Their experimentation also shows that a significant portion of the air follows a direct vertical path between two vents. The conclusions of their report were that (1) it could be shown that small flows of air can transport significant quantities of water vapor out of the cavity and (2) air flow through an air space can reduce heat flow through the cavity, although significant air flows are required for this to occur.

It is therefore crucial to understand the mechanics of air flow in order to accurately model its movement through the cavity. Specifically, the turns and obstructions to the flow must be considered.

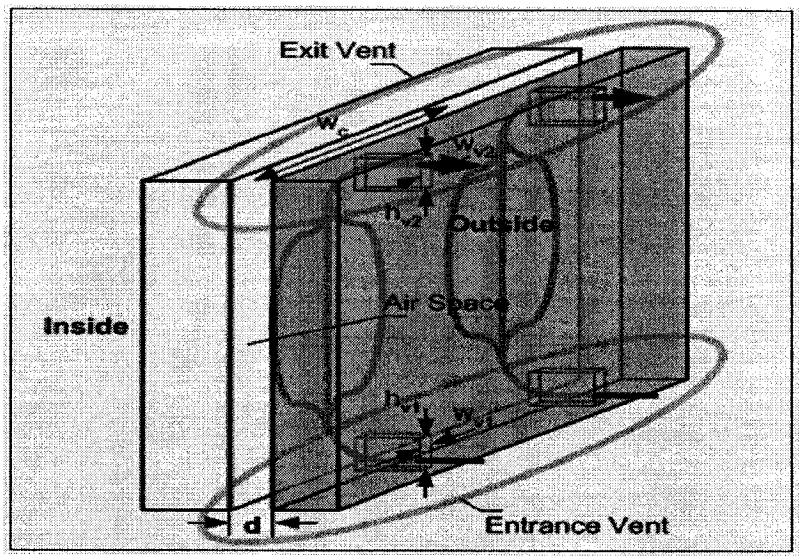

Figure 2.3: Path of air flow through the weepholes and the cavity (as per Straube et al., 2004)

2.5.2 Driving Influences of Air Flow

Kunzel and Mayer (1983) performed a comprehensive study involving field testing of air movement behind large instrumented cladding panels on a three-storey building. Among their conclusions, it was found that ventilation drying of the wall assembly was mostly influenced by wind pressure, solar-induced buoyancy, and solar radiation. Solar radiation increased the temperature of the cavity air and therefore induced a higher volume of air displacement. With low wind speeds of 1 to 3 m/s, average air velocities of 0.05 to 0.15 m/s were measured in the cavities. They also concluded that sufficient cavity ventilation prevented the occurrence of moisture flow across the air cavity and the resulting condensation on the backwall in most cases. Finally, they observed that, if the cladding or backwall has low vapor permeance, or if the cladding is not relatively airtight, air movement in the cavity has a much less significant effect on moisture transport.

The possible economic ramifications of driven air flow were also considered. Guy and Stathopoulos (1983) conducted an analytical study on energy consumption and reduction due to buoyancy-driven ventilation within claddings. They did not consider the effects of wind pressure. Their findings suggest a significant cooling load savings during the summer by allowing for large venting

areas of the cavity. Also significantly reducing the cooling load was the reduction of the emissivity values of the cavity wall surfaces. Unfortunately, the effects of cavity ventilation had the opposite effect in the wintertime, as cooling of the cavity walls resulted in increased heating loads. As a result, annual energy consumption was largely unchanged.

Another factor to consider is solar radiation. Straube and Burnett (1998) have shown that the temperature of air in the cavity can be increased from 10°C to 30°C above the ambient air temperature due to solar radiation. The buoyancy effect created will drive the air flow. Therefore, they conclude that outdoor air moving through the cavity will more likely remove moisture from the cavity rather than carry in more from the outside.

Radiation occurring between the facing surfaces of the cavity also has an effect on heat transfer and airflow. While not observing specifically brick veneer wall assemblies, Lauriat and Desrayaud (2006) observed air movement through partially enclosed cavities with semi-transparent cladding and a temperature differential caused by solar radiation. The radiative exchanges between the facing walls were found to decrease the difference in the average temperatures of the vertical walls. Radiation tends to significantly decrease the temperature of the hot wall while the increase in temperature of the cold wall is less important. They conclude that the radiation exchanges occurring between the two facing walls of the cavity are required for accurate calculations.

It is therefore clear that solar-induced air buoyancy, wind pressure, solar radiation and radiation exchanges within the cavity have a role to play in driving the air flow through the weepholes and the cavity.

2.5.3 Wind Pressure and Cavity Air Velocity

One of the first experiments conducted in this field occurred in Germany in the early 1970's. Schwarz (1973) studied an 18-floor apartment building by installing open-jointed panel cladding on the exterior walls with the objective of measuring

the velocity of the air flow within the cavity. Given low wind speeds of 0 to 8 m/s, he measured cavity air velocities ranging from 0.2 to 0.6 m/s. Most interestingly, on the leeward side of the building, where wind speeds were small or insignificant, cavity air velocities were found to be relatively stable at 0.2 m/s.

Later, Fazio and Kontopidis (1988) performed a field test relating cavity pressure in rain screen walls to the surrounding wind pressure. A small experimental testing station was constructed with a brick rainscreen and wood studs. The cavity was not subdivided into compartments. It was found that equalization occurs between the cavity pressure and the wind pressure when the cladding has only cracks and no vent holes. The relationship does not hold when uniformly distributed openings are added. However, when one specific hole is placed with proper sizing, pressure equalization can be restored within 10% across the cladding, such as a 100 by 130 mm hole for a 20 m^2 wall. TenWolde *et al.* (1986) argued that such a pressure equalization was required to prevent or at least deter water from being driven inward into building wall assemblies.

Sandin (1993) performed a study of ventilation drying in masonry veneer wall systems. His original intent was to prove that wind was the primary ventilation mechanism. However, as his research showed, ventilation rates during periods when the cladding was warmer than the outside air were almost always higher than when the cladding was at the same temperature as the outside air. He also found that wide, ventilated air spaces had a tendency to reduce moisture transport inward to the backwall of brick wall assemblies.

The preceding research shows that wind pressure does have an effect not only on ventilation drying but also a significant effect on the air velocity within the cavity.

2.5.4 Ventilation Drying

As air passes through the cavity, its contact with the inside of the brick causes moisture to be evaporated into the air by moisture convection. The moving air

then evacuates it from the cavity via the upper vents. Hens and Fatin (1995) made several observations regarding air flow in cavities of brick veneer walls. Summarizing a series of field, laboratory and theoretical studies for the climatic conditions of Belgium, their conclusions were twofold: that ventilation of the air space had little to no effect on the heat transfer of the air space, and that it was difficult to clearly define the benefit of ventilation in terms of the removal of moisture from the wall assembly. As a result, they recommended continuing including air spaces in brick cladding wall constructions, but mainly for their drainage purpose. Conversely, Straube and Burnett (1995) completed a study for the Canadian Mortgage and Housing Corporation that same year that concluded that ventilation could provide a significant drying potential and could even bypass the vapor resistance of other types of cladding.

Shortly thereafter, Salonvaara *et al.* (1998) studied wall cavity ventilation between the sheathing and different types of sidings. Their findings indicate that, for summer conditions, the backwall of assemblies with no cavity ventilation demonstrated an increase in moisture content, while in ventilated walls, there was indeed a slow drying effect in the bottom part of the backwall. Their conclusion was that ventilation within cavities does indeed assist in the drying of the backwall during summer conditions, except if the exterior cladding has a low vapor permeance. That same year, Straube and Burnett (1998) state in an experimental study that, in normal walls, the ventilation drying rate is governed by the ventilation flow rate, and not by the ability of wetted backwall materials to evaporate moisture into the air space. They also state that current construction practices should ensure an adequate amount of ventilation. They recommend slightly larger, unobstructed cavities and larger vent areas.

More recently, Hansen *et al.* (2002) performed a field study in which they determined that the outdoor air has a role to play in the drying of wall assemblies with air cavities. They observe that the higher the moisture content of the outdoor air, the greater the risk of that outdoor air transmitting that moisture into the cavity and backwall. Their conclusion was that wood-frame walls with no

cavity ventilation demonstrated an inferior performance in terms of the moisture content in their backwall than walls with cavity ventilation.

While most research is in relative agreement that air movement in cavities can have drying effects on the brick and backwall, there has been little study on the quantification of air flow, even for summer conditions.

2.5.5 Models and Computational Analysis

Many computational models have been developed in recent years to observe cavity air flow situations. Landon and Campo (1999) observed, using a computational model, various closed cavity configurations to determine the velocity of air as it passes along one heated wall. They found that, due to natural convection alone and without the influence of outside air, that ambient air passing along a wall heated to 137°C reached 0.0791 m/s along the heated wall for a tall rectangular cavity.

Stovall and Karaziogis (2005) produced a computational fluid dynamics (CFD) study to predict whether an increase in cavity depth would increase the air flow through the space. The results of their study found no significant difference in the mass flow rates between cavity depths ranging from 19 to 50 mm. On the other hand, they found that doubling the ventilation slot height doubled the air flow rate, showing that the ventilation slot size is the controlling factor for the range of cases they considered. They also concluded that the natural convection within the air cavities, driven by the temperature difference between the cavity walls and the outside air, was a very significant factor driving the ventilation flow.

It should be noted that existing hygrothermal analysis software, such as CHAMPS (BEESL, 2007), have implemented air transfer functions in cavities with simplified numerical methods. This trend indicates that the effects of air movement in cavities is becoming increasingly important in heat and moisture transfer analysis, and that more computational models and research in this field is expected in the upcoming years.

2.6 Conclusion

The latest work related to air movement and transport within building envelope cavities was summarized. A review of past experimentation involving the characterization of air flow, the effect of different parameters including wind, the drying of brick by ventilation of the cavity and current software available was presented.

This literature review indicates that the study of air velocity within a building envelope cavity is not new and has been on-going for some time. The functions of the cavity are known: to equalize the air pressure, to provide a capillary break for inward-driven rain water and to allow some air movement. There have been many field experiments to study in particular wind pressure and ventilation drying of building wall assemblies with air cavities. Heat, air and moisture transport modeling of the hygrothermal performance of the envelope is moving towards integrating air movement in the cavity. .

Less known are the conditions of the buoyancy of air within the cavity, as well as its role in evacuation of heat and moisture from the assembly. This is one function of the air cavity where more knowledge is required. Also of interest is the study of the movement of air within the cavity, its specific path, velocity under specific conditions and type of flow. Since a lot of work looked at walls designed to control outward vapor flow and winter conditions, it would appear useful to study inward-driven vapor flow and summer conditions as a specific condition. Finally, the coefficients of convective transfer of moisture at the brick/air interface in the cavity are not well known, especially in terms of air velocity and flow development. This study attempts to contribute by studying these issues in particular. This is done with a combination of numerical modeling, analytical analysis and laboratory experimentation.

Chapter 3: Model Development

This chapter describes the development of a model to determine air movement within brick veneer cavities. The chapter begins with the objectives of the work. This is followed by an introduction to the physical system represented by the model, including assumptions. Then, the method chosen to discretize the situation into control volumes is explained and the methods of calculation are presented with two examples. Finally, model results for the given situation are presented, and analysis is conducted.

3.1 Objectives of the Work

The main objective is to develop a numerical model of air movement in the cavity of a brick-cladded wall, including all heat, air and moisture transports. This model is implemented for a set of given conditions, using several assumptions. Within that context, many other objectives are sought. Firstly, it is desired to determine the temperature distribution throughout a wall assembly and especially within the cavity itself. This will allow the evaluation of the evacuation of heat from the assembly by the cavity air movement. Secondly, the profile of relative humidity in the brick and cavity will be sought to determine the effect of air movement on the movement of moisture out of the assembly. Finally, the determination of the air velocity in the cavity itself is of interest to see if it has an effect on the previous two objectives. As can be seen in figure 3.1, the cavity ventilation can theoretically reduce the amount of heat and moisture driven into the brick cladding. As such, it will be of interest to quantify this phenomenon.

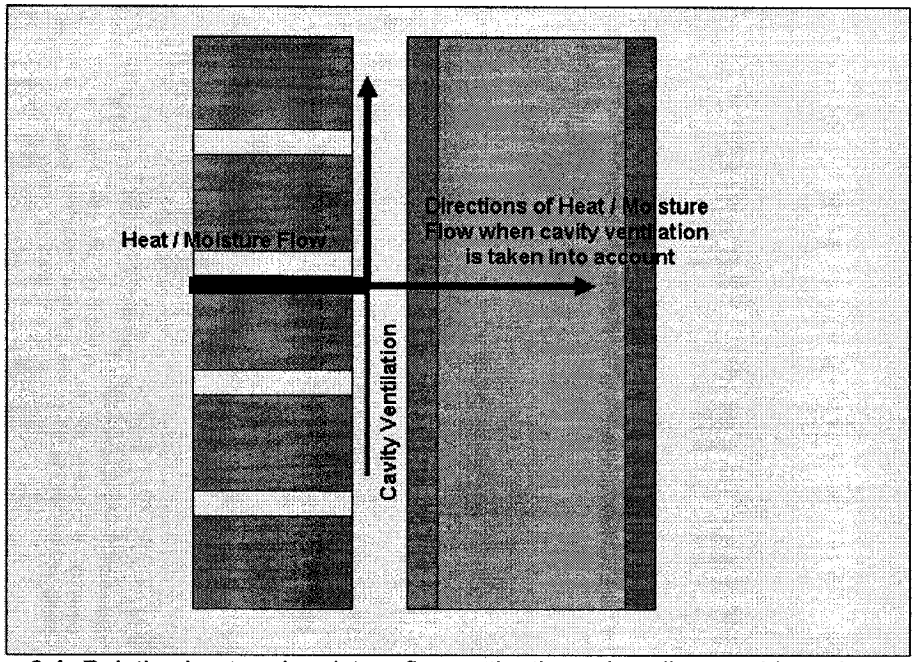

Figure 3.1: Relative heat and moisture flow paths through wall assembly under summer conditions

3.2 Model Characteristics

This section presents the general flow of air, heat and moisture through the wall composition, the initial situation and conditions for which the model were developed, the main assumptions of the model, and its physical geometry including the material properties, dimensions and characteristics.

3.2.1 Flows through Wall Assembly

As the air in the wall assembly cavity is heated via the brick by exterior conditions (outdoor temperature and solar radiation), its density decreases, and the air in the cavity tends to rise. To replace the rising air, fresh outdoor air is drawn into the lower weepholes, which becomes the air path inlet. Once the air reaches the top of the cavity, it exits via the upper vents, which become the air path outlet. This situation is schematically represented in figure 3.2. As the air is heated, its global velocity increases and some of the hot air will be evacuated. If the wall was wetted by rain prior to exposure to solar radiation, the moisture driven out of the brick layer may also be evacuated along with the air transport. A possible representation of the air flow path in the wall cavity is through the use of a series

of tubes, see Figure 3.2. Such representation allows to conveniently model the pressure losses of the air experience along its trajectory. The driving potential for air movement along its path is the air pressure differential due to buoyancy.

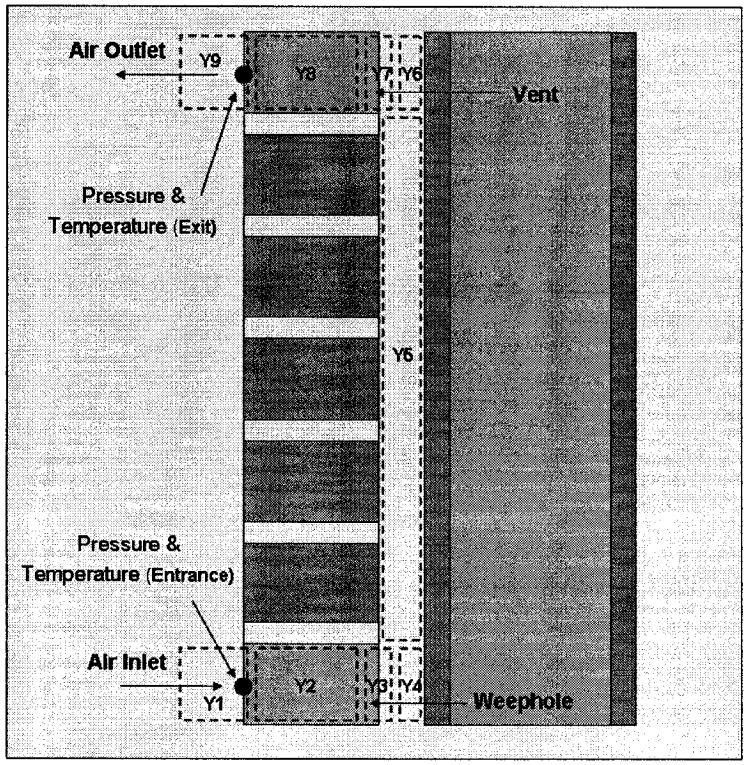

Figure 3.2: Schematic of air through the wall assembly

3.2.2 Boundary Conditions

The base case to be analyzed is located in Montreal, Quebec, Canada. The month of July is selected as it is the summer month with the highest outdoor temperatures and high magnitude of solar radiation. Figures 3.3, 3.4 and 3.5 demonstrate the steady-periodic sinusoidal functions used as boundary conditions for outdoor temperature, solar radiation and relative humidity, respectively, for a typical 48-hour period. The outdoor temperature and relative humidity vary from a high of 26°C with 50% RH during the afternoon to a low of 15°C with 80% RH overnight. Solar radiation achieves a peak of 1000 W/m^2 on a south-facing wall. Interior conditions are maintained constant at 23°C with 40% relative humidity. These parameters were inferred from the study of meteorological data for Montreal in July. The brick is assumed to be saturated to

a level of 50% of capillary saturation. Using a sorption curve (Kumaran 2002), this moisture content is found to be the equilibrium moisture content at a relative humidity of 99.93%. This value is set at the beginning of the first day of testing with no further wetting afterward.

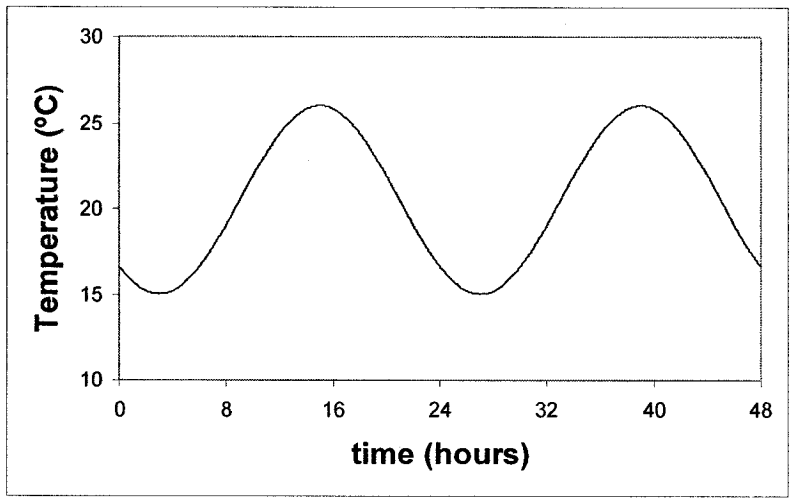

Figure 3.3: Outdoor temperature profile for a typical 48-hour time average period for Montreal in July

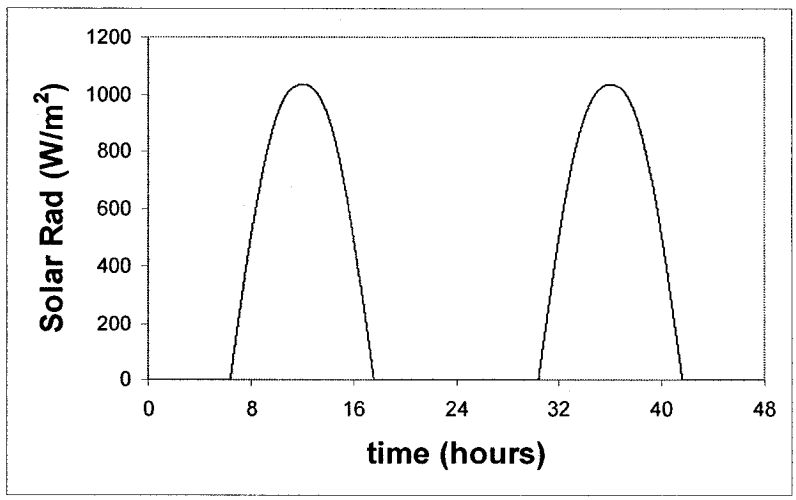

Figure 3.4: Solar radiation profile for a typical 24-hour time average period for a south-facing wall in Montreal in July

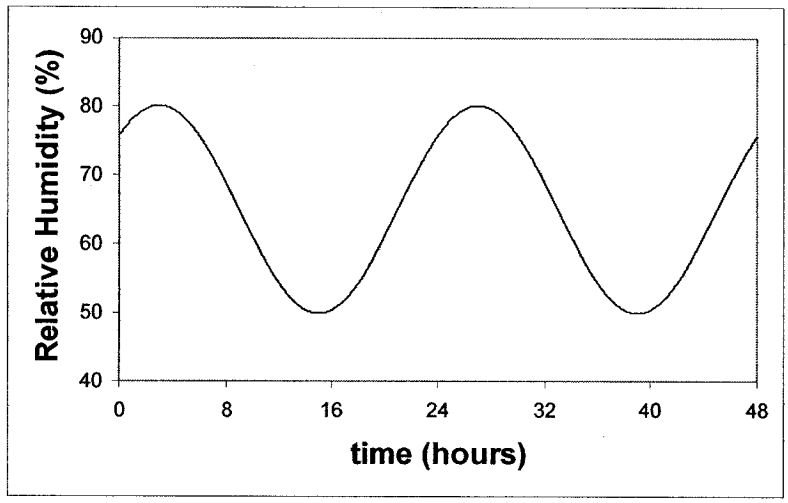

Figure 3.5: Outdoor relative humidity profile for a typical 48-hour time average period for Montreal in July

3.2.3 Model Assumptions

The modeled wall assembly is one that would be found in one-storey residential buildings with brick cladding and wood-frame structures, such as the bungalow seen in figure 3.6. This simple geometry is retained; however, larger or more complex geometries may be effectively modeled in future studies. As well, an average bungalow may or may not have its cavity open to the attic; it is assumed here to be closed to reasonably limit the scope of the study. As mentioned above, it is convened that the movement of the air in the cavity be the result of only natural convection by buoyancy of air, as this natural process occurs in a more predictable manner than wind. A coupling with weather data to include wind pressures could be done as an extension of the discussed project. Another assumption made is that there is no influence from neither the top nor the bottom of the assembly in terms of heat or moisture. As such, there is no heat transfer considered from the ground, nor from the roof. As well, no moisture uptake from the ground, or leaks or runoff from the roof are calculated. Such moisture sources are exceptional cases and fall beyond the scope of the objectives of this study. Yet another assumption is that the backwall and the cladding, aside from the vent openings, are considered to be airtight. This is to prevent losses of air pressure and the premature release of air from the air flow path. As a consequence of this, the brick wall is considered to be composed solely of brick,

and differences of material properties that would have resulted from the addition of mortar between the bricks are discarded. Finally, the relative humidity profile to be calculated is only performed for the brick and air cavity, leaving out the materials of the backwall. This also means that the relative humidity of the interior environment is not considered. This is to spare desorption computations for the materials of the backwall not required as the moisture is driven from the outside. As well, this last simplification significantly reduces the already considerable time required to perform numerical simulations.

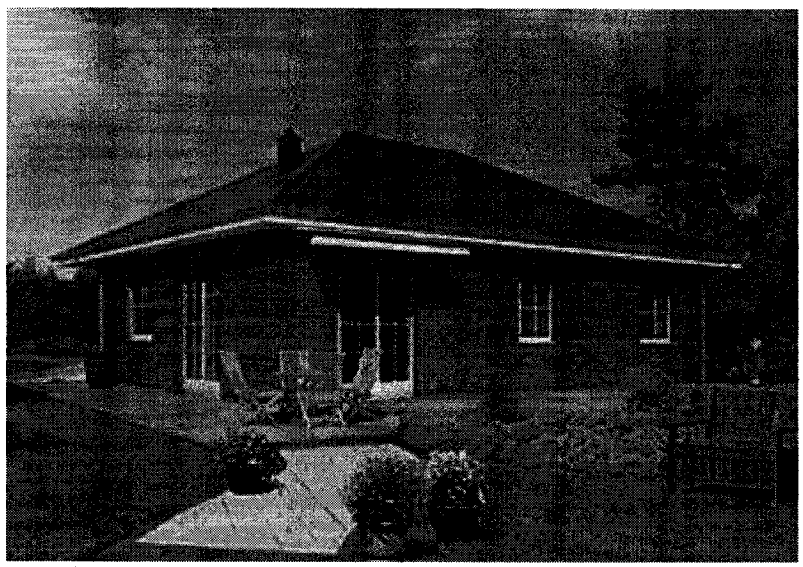

Figure 3.6: Typical bungalow residential building with brick cladding (CREA, 2006)

3.2.4 Wall Geometry and Characteristics

The wall assembly used is composed of several layers of materials, which is common for most brick veneer wood-frame residential buildings in North America. The cladding consists of clay brick of 90 mm thickness. This is followed by the air cavity of a thickness of 25 mm. The backwall then separates the air cavity from the interior of the building. It consists of wood studs of dimensions 39 mm by 89 mm placed at 400 mm center to center. Between the studs, glass fiber batt insulation of thickness 89 mm is inserted. On the cavity side of the wood stud/insulation layer, there are panels of fiberboard of 12 mm thickness. On the indoor side, there are panels of gypsum board, also of 12 mm thickness. There are three weepholes placed on the bottom of the assembly and

three vents placed at the top (with spacing of 2 bricks between the center and the side openings, or 400 mm center to center), with openings of 10 mm by 55 mm. The wall has a height of 3.0 m, typical for one or two story residential buildings, such as bungalows. As the evaluation of the situation is only two-dimensional, a depth of 1.0 m is considered. The emissivity of both the brick and backwall, for purposes of calculating the radiation exchange, are taken as 0.9. The transmittance-absorptance of the brick, for solar radiation calculations, is assumed to be 0.7.

The material properties used in the calculations are found below, including density, thermal conductivity, specific heat, vapor permeability and moisture storage capacity. Table 3.1 schedules the values used in the model for each building material for heat transfer. Table 3.2 displays the equations used in moisture transfer for the material properties which are dependent on relative humidity. All values listed are based, directly or approximately, on the work of Kumaran (2002). In particular, the moisture storage capacity of brick is defined as the slope of the sorption curve of brick. In these tables, Φ represents relative humidity [%], R_v is the gas constant for water vapor [461.5 J/kgK], and T_K is the temperature [K].

Table 3.1

Building Material Thermal Properties (Kumaran, 2002)

Building Material	Density [kg/m^3]	Thermal Conductivity [W/mK]	Specific Heat [J/kgK]
Brick	1980	0.4200	840
Air Space	1.2	0.0240	1000
Fiberboard	320	0.0535	1880
Wood Stud	460	0.0904	1900
Insulation	30	0.0400	840
Gypsum	625	0.1600	870

Table 3.2

Building Material Moisture Properties (Kumaran, 2002)

Building Material	Vapor Permeability [kg/m·s·Pa]	Desorption Curve [kg/kg]	Moisture Storage Capacity [kg/kg]
Brick	$4 \cdot 10^{-12} \exp(0.0036\phi)$	• Φ = 0.989 to 0 : $4.55 \cdot 10^{-2}(\phi)$ • Φ = 0.9993 to 0.989 : $1 \cdot 10^{-33} \exp(0.7322(\phi))$	• Φ = 0 to 0.989 : $4.55 \cdot 10^{-2}$ • Φ = 0.989 to 0.9993 : $7.322 \cdot 10^{-34} \exp(0.7322(\phi))$
Air Space	$\frac{2.88 \cdot 10^{-5}}{R_v \cdot T_K}$	N/A	$6.1 \cdot 10^{-6}$

3.3 Methodology

The model includes a series of steps to calculate the cavity air velocity, temperature profile and partial vapor pressure profile, which is then converted to the relative humidity profile. In this section, the methodology is presented. Firstly, the discretization of the wall assembly into the computational domain is explained. This is followed by the calculation procedures for both heat and vapor transfer. Finally, an explanation of the application of control volume theory for the model is given, and specific examples within the model computational domain are presented. The implementation of the model was done without recourse to pre-existing code and was developed in Matlab language.

3.3.1 Computational Domain

The computational domain can be defined is the discretization under consideration for calculation by the model, both in space and time. The two-dimensional domain is discretized, i.e. subdivised into control volumes. The properties of the each control volume are assigned to its node. The wall assembly is evaluated at a total of 500 nodes, including 50 in the air space itself

and 5 in each weephole or vent channel through the brick. As can be seen in figure 3.7, the horizontal dimension of the wall assembly is subdivided into 10 columns, which is to allow for an increment ratio of any two adjacent nodes of less than 2.5. By trial and error, this subdivision of the computational domain was found to be optimal in terms of computation time and number of cells.

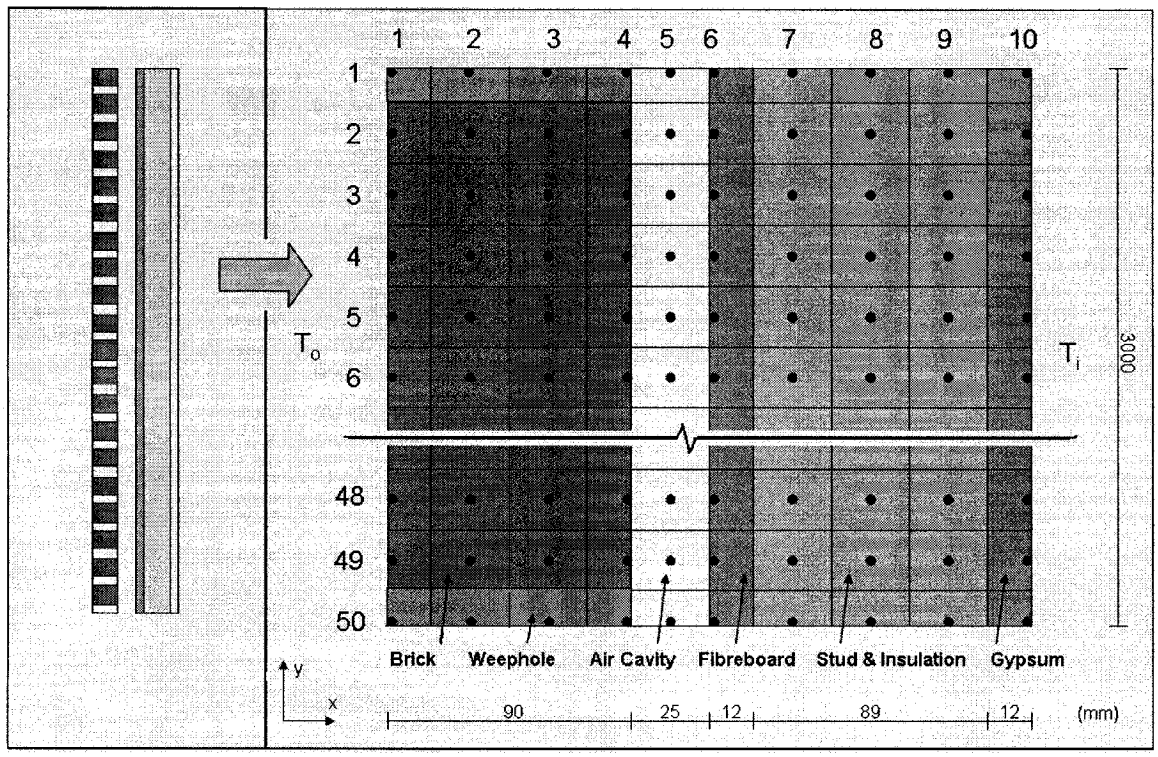

Figure 3.7: Nodal positions and wall assembly configuration (not to scale)

In terms of time discretization, also by trial and error, it was determined that a 10-second time interval was both brief enough to allow convergence of iterations, but long enough to alleviate potentially time-consuming repeated computations. The temperature and later vapor pressure profiles are determined at each nodal position. However, as will be shown, the cavity air velocity plays an important role in the nodal temperature matrix. The process is iterative, as initial temperature and velocity values are assumed before calculations commence.

3.3.2 Calculation of Temperature Profile

The model is first initialized with the control volume dimensions, building material properties and heat fluxes as a result of interior, exterior and solar radiation conditions. The initial nodal temperature values are assumed, and an initial cavity air velocity is assumed to be close, but not equal to 0 m/s. From the temperature profile, the air pressure at the inlet and outlet can be calculated, and, from the velocity, the dimensionless Reynolds and Nusselt numbers can be determined. The Reynolds number is used to calculate the friction losses in the cavity, while the Nusselt number is required in the correlation to determine the coefficient of convective heat transfer within the cavity. With values for the losses and the driving air pressure difference, a new cavity air velocity is established using equation 2.14. The temperatures at all nodes is then calculated by the procedure outlined by the algorithm shown in figure 3.8. With a first temperature matrix in place, the cavity inlet and outlet air pressures are again calculated. The process continues to iterate until the difference of air velocity at the entrance inlet for the last two iterations is less than 10^{-5} m/s. Once that iteration condition is satisfied, the second condition, i.e. assuring that, at the corresponding cavity air velocity, the calculated temperature matrix is within 10^{-5} degrees Celsius of the assumed or previous condition, must also be met. Once both conditions are satisfied, it is assumed that an accurate representation of the nodal temperatures at a given time step has been achieved. The entire process will then be repeated for all subsequent time steps. Figure 3.8 demonstrates this process in a more visual fashion by means of a flow chart.

3.3.3 Calculation of Vapor Pressure Profile

Once the temperature profile is determined, the vapor pressure profile may be calculated with less expansive computations for the same time step. Initial relative humidity values are assumed for all nodes of the assembly, with the brick assumed to be initially saturated and the cavity having approximately the same relative humidity as the outdoor air. From the nodal temperature profile calculated previously, the saturation vapor pressure of each node can be

determined for all time steps. With the relative humidity and saturation vapor pressures known, the partial vapor pressure profile for the first time step is calculated. With the known relative humidity and temperatures, two relative humidity dependent properties can be determined at all nodes: vapor permeability and moisture storage capacity. From the known convective heat transfer coefficient and vapor permeability of the air, the coefficient of convective moisture transfer may then be calculated by correlation. With these values in place, the partial vapor pressure is recalculated for all nodes by the procedure outlined in figure 3.9. Once this new matrix has been established, the new partial vapor pressures, divided by the known saturation vapor pressures will yield the new relative humidity profile. From this, the vapor permeabilities, moisture storage capacities and surface moisture transfer coefficient are recalculated and a final partial vapor pressure matrix may be calculated. The process is then repeated for each successive time step.

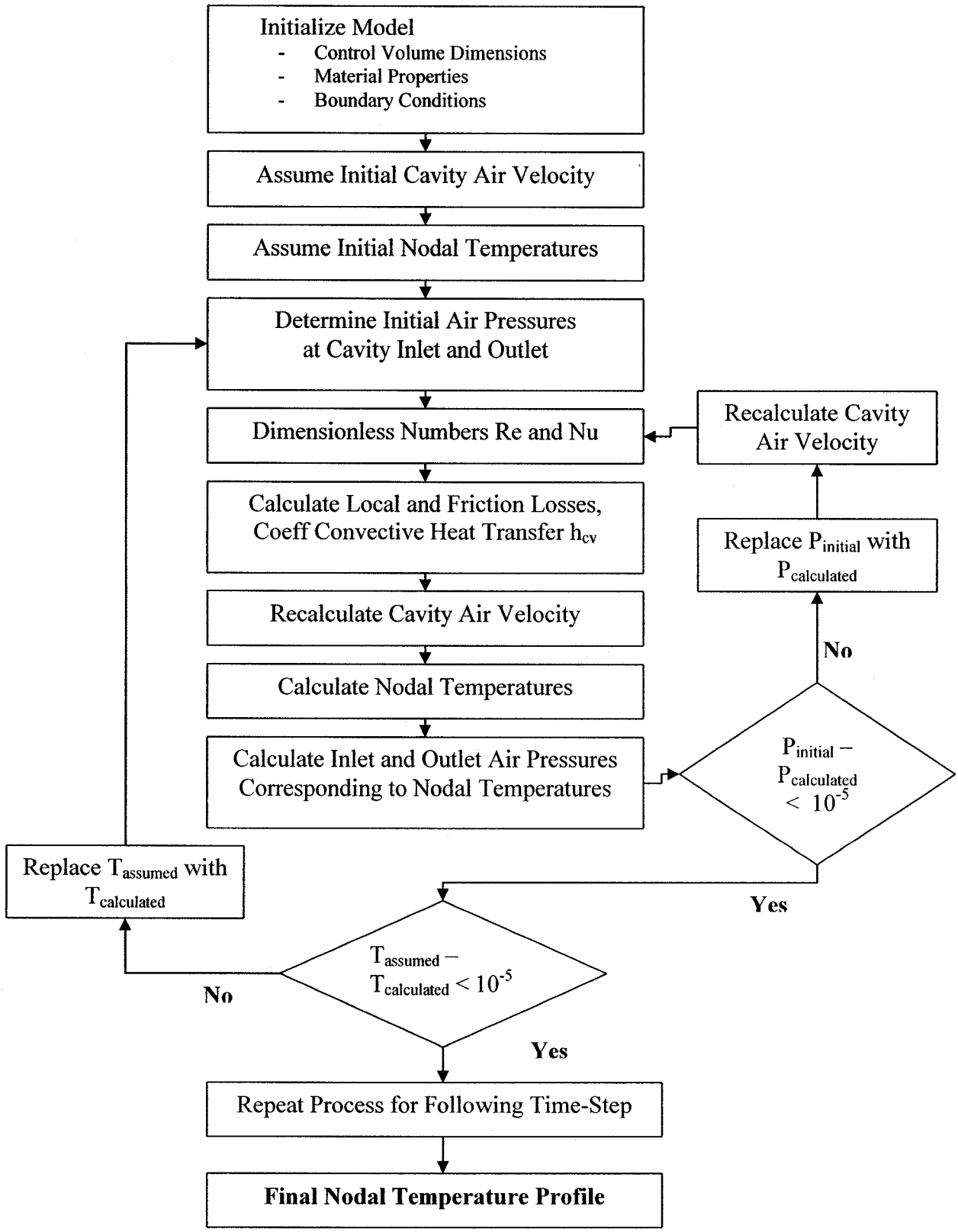

Figure 3.8: Algorithm of procedure for calculation of nodal temperature profile.

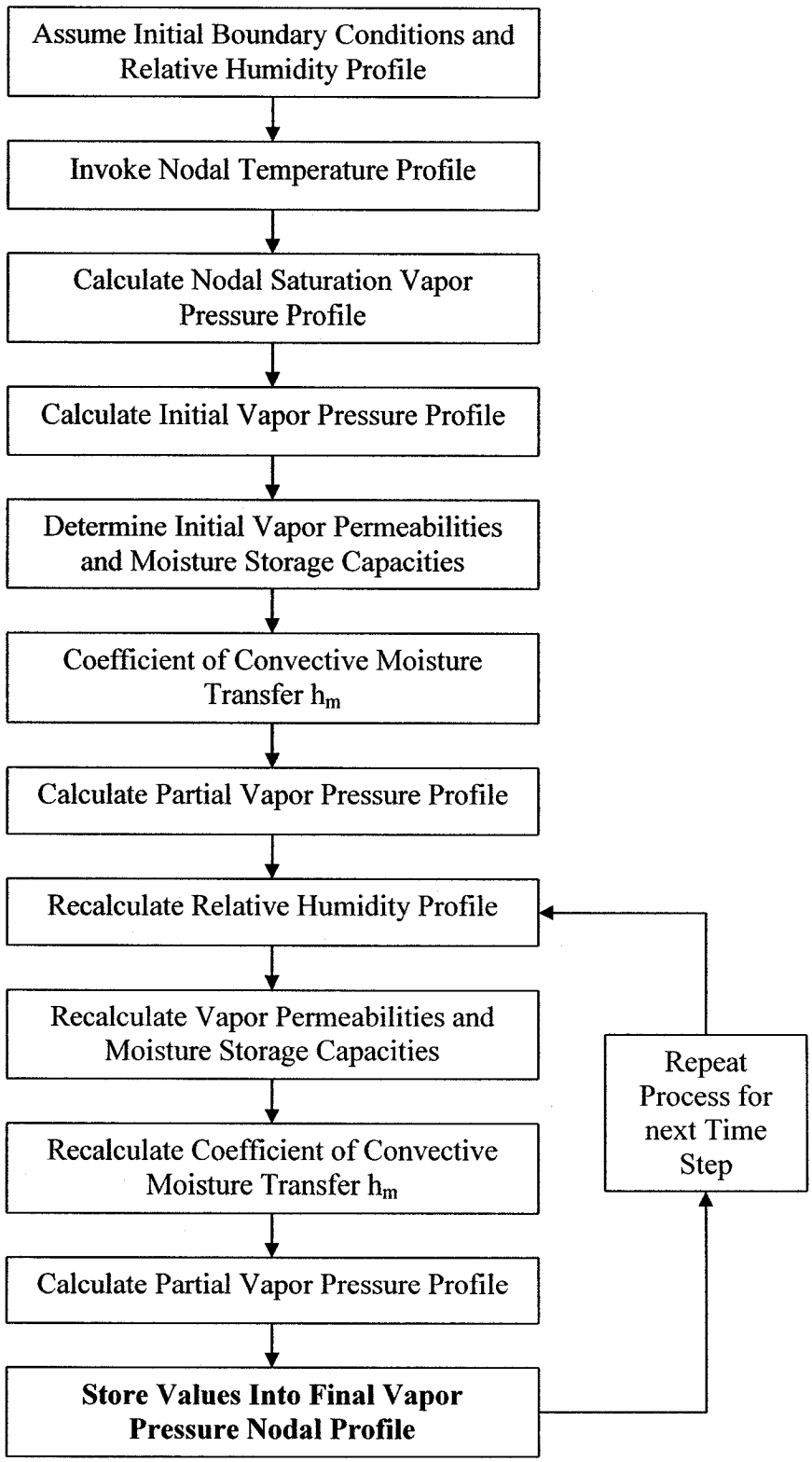

Figure 3.9: Algorithm of procedure for calculation of nodal partial vapor pressure profile

3.3.4 Energy and Mass Balance Equations

With the calculation procedures for the temperature and partial vapor pressure profiles in place, the equations that represent these phenomenon and the methodology behind their utilization are now presented. Most heat and moisture transfer phenomena can be described using differential equations, equations for which the derivative of a variable is a function of the variable itself. These equations are continuous, but numerical analysis requires discretization, or subdivision into a nodal network, of the computational domain. Each node encompasses the properties of the control volume, or delineated area within the computational domain, that it represents. The control volume method is used to approximate the continuous results to the nearest relevant decimal at set time intervals, while minimizing errors.

The control volume method is well suited for the application studied here, although it is not the only method that could have been considered, and was chosen for the model due to the rectangular nature of the wall assembly, as well as the reduced complexity of computations. Morton (2005) recognizes three methods of discretization: implicitly, explicitly, and by the Crank-Nicholson method. Let us consider a heat transfer equation where the heat flow Q is a function of time t and space x, keeping in mind that moisture transfer equations are analogous.

$$Q = f(t, x) \tag{3.1}$$

By discretizing the computational domain into j rectangular control volumes and n time steps, where j and n are integers, and by defining the difference between two consecutive space points to be Δx and two consecutive time points to be Δt, we may evaluate the heat balance at each time and space interval, by applying a space-time calculation method. The control volume height may be considered to be Δy, and the width Δz. For this study, the method used is the implicit method. Morton (2005) explains that, with the implicit method, a backward time difference at time (n-1) and a central difference for the space derivative at position j will

yield the following recurrence equation, in one dimension (if only thermal conduction is considered):

$$\frac{k\Delta y\Delta z}{\Delta x}(T_{j+1}^{n}-T_{j}^{n})+\frac{k\Delta y\Delta z}{\Delta x}(T_{j-1}^{n}-T_{j}^{n})=\frac{q_{j}^{n}-q_{j}^{n-1}}{\Delta t} \tag{3.2}$$

We may then evaluate the temperature T at each position at time n by rearranging equation 3.2 into a system of linear equations, such that:

$$\left(\frac{k\Delta y\Delta z}{\Delta x}\right)T_{j-1}^{n}-2\left(\frac{k\Delta y\Delta z}{\Delta x}\right)T_{j}^{n}+\left(\frac{k\Delta y\Delta z}{\Delta x}\right)T_{j+1}^{n}=\frac{q_{j}^{n}-q_{j}^{n-1}}{\Delta t} \tag{3.3}$$

According to Morton (2005), this method has proven to be quite numerically stable and convergent for a wide-range of time steps. It is the most relevant method for use in the model as all temperatures, as opposed to heat flows, will be calculated in a system of equations based on material properties, time steps, special distances and the previous temperature at a given node. After initial temperature conditions are assumed, the system of equations can converge and calculate temperatures with good accuracy. The other two methods, explicit and Crank-Nicholson, are relevant for other applications but have been deemed not most suitable for the heat and vapor transfer model developed here.

The model evaluates heat flows and temperatures in two-dimensions, x and y. All references to the third dimension, z, are purely to ensure that volumetric terms or transverse area components in constitutive equations are respected, but the depth of the system in the model is always assumed to be unitary. A representation of the two-dimensional nature of the model and the variables used can be seen in figure 3.10.

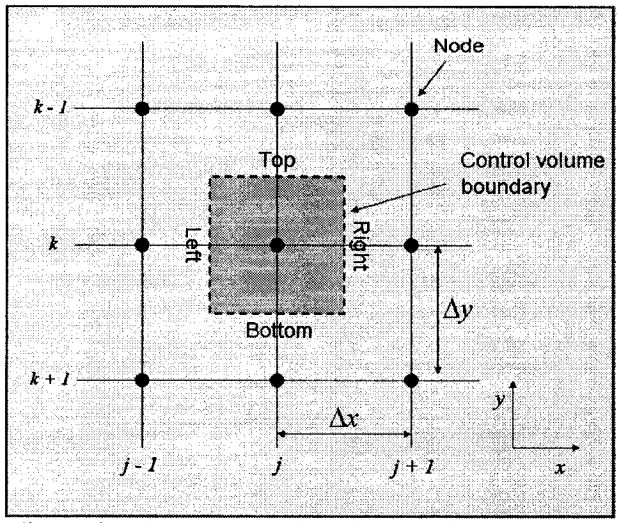

Figure 3.10: Two-dimensional representation of the nodal network (as per Kreith, 2001)

As for the computational aspect, the bi-dimensionality of the model requires some adjustment to the equations derived using the implicit finite-difference method. A second set of terms to reflect the second dimension will therefore be added. We implement the second spatial dimension *y* with a difference in distance between nodes *Δy*, as well as an integer *k* to reflect the number of nodes in the y-direction. The positions of each node must be redefined from one dimension to two. For example, the central node in the equation is redefined from *j* to *(j,k)*. Again, considering only thermal conduction, equation 3.2 now becomes:

$$\frac{k\Delta y\Delta z}{\Delta x}(T^n_{(j+1,k)} - T^n_{(j,k)}) + \frac{k\Delta y\Delta z}{\Delta x}(T^n_{(j-1,k)} - T^n_{(j,k)}) + \frac{k\Delta x\Delta z}{\Delta y}(T^n_{(j,k+1)} - T^n_{(j,k)}) + \frac{k\Delta x\Delta z}{\Delta y}(T^n_{(j,k-1)} - T^n_{(j,k)}) = \frac{q^n_{(j,k)} - q^{n-1}_{(j,k)}}{\Delta t} \quad (3.4)$$

In the one-dimensional calculation, the heat flow at the central position, q_j, was calculated along with the heat flows in the two positions directly preceding and succeeding it, as per equation 3.3. As equation 3.4 is expanded to isolate each individual heat flow, the additional two terms reflect the heat flows to the top and the bottom of the central node. This operation yields:

$$-\left(\frac{2k\Delta y\Delta z}{\Delta x}+\frac{2k\Delta x\Delta z}{\Delta y}\right)T^{n}_{(j,k)}+\left(\frac{k\Delta y\Delta z}{\Delta x}\right)T^{n}_{(j-1,k)}+\left(\frac{k\Delta y\Delta z}{\Delta x}\right)T^{n}_{(j+1,k)}$$
$$+\left(\frac{k\Delta x\Delta z}{\Delta y}\right)T^{n}_{(j,k-1)}+\left(\frac{k\Delta x\Delta z}{\Delta y}\right)T^{n}_{(j,k+1)}=\frac{q^{n}_{(j,k)}-q^{n-1}_{(j,k)}}{\Delta t} \quad (3.5)$$

Due to the transient nature of the model, the concept of thermal storage must be introduced. For a given time step, thermal storage may be expressed by equation 3.6, which takes into account the temperature of building material *i* at both the present time step *n* and previous time step *(n-1)*.

$$\frac{q^{n}_{(j,k)}-q^{n-1}_{(j,k)}}{\Delta t}=\frac{\rho_i c_i \Delta x\Delta y\Delta z}{\Delta t}(T^{n}_{(j,k)}-T^{n-1}_{(j,k)}) \quad (3.6)$$

Equation 3.5 can be rearranged to be in terms of the temperature values for the five relevant volumes (the central volume and its four adjacent volumes), taking into account the thermal storage on the right-hand side of the equation, as per equation 3.7.

$$C_1T^{n}_{(j,k)}+C_2T^{n}_{(j-1,k)}+C_3T^{n}_{(j+1,k)}+C_4T^{n}_{(j,k-1)}+C_5T^{n}_{(j,k+1)}=\frac{\rho_i c_i \Delta x\Delta y\Delta z}{\Delta t}(T^{n}_{(j,k)}-T^{n-1}_{(j,k)}) \quad (3.7)$$

The coefficients C are described in Appendix C. Equation 3.7 may be further simplified to create the final matrix from which all nodes will be calculated. Since the coefficients C do not change from one time step to the next, they may be expressed in a permanent square matrix [C] having the number of nodes N of the computational domain in both rows and columns, as in N x N. It should be noted that the [C] matrix is constant because thermal conductivity is considered constant, thus independent of moisture content. The temperatures for each subsequent time step may be calculated in a matrix {T} which will be calculated at each time step, and will have dimensions of 1 x N. Finally, the thermal (or moisture) storage terms, as well as all heat fluxes as a result of the boundary conditions, may be summed into another permanent matrix on the right hand side of the equation, called [R], which will also have dimensions of 1 x N. This

creates equation 3.8, which will be iterated at each time step until an accurate solution is reached. This iteration is necessary as the boundary conditions are assumed for the first iteration, as explained in section 3.2.2.

$$[C]\{T\} = [R] \tag{3.8}$$

In terms of vapor transfer, it must be noted that, unlike heat transfer material properties that are taken to be constant, vapor permeability and moisture storage are functions of the relative humidity at each node of the network. As such, the complexity of the calculation is somewhat augmented.

As the brick will be initially considered to be saturated by rain water, the storage difference of moisture is considered first, by equation 3.9.

$$\frac{g^n_{(j,k)} - g^{n-1}_{(j,k)}}{\Delta t} = \frac{\rho_i \xi_i(\phi^n_{(j,k)})\Delta x \Delta y \Delta z}{\Delta t \cdot p^n_{v,sat}} (p^n_{v(j,k)} - p^{n-1}_{v(j,k)}) \tag{3.9}$$

In this equation, the moisture capacity term, $\xi_i(\phi)$, can be defined as the slope of the sorption isotherm for the material in which the node is found. It is a function of the relative humidity ø at the given node. The sorption isotherms and their derivatives are adapted from the work of Kumaran (2002). The terms p_v and $p_{v,sat}$ refer to the vapor pressure and saturation vapor pressure [Pa] of the node at the given time steps. The moisture stored by the brick can move by diffusion dependent on the permeability of the materials and local vapor pressure differentials. These phenomena are modeled by equations presented in Chapter 2. Along the format of equation 3.7, moisture movement is described as:

$$\begin{aligned} &G_1 p^n_{v(j,k)} + G_2 p^n_{v(j-1,k)} + G_3 p^n_{v(j+1,k)} + G_4 p^n_{v(j,k-1)} + G_5 p^n_{v(j,k+1)} \\ &= \frac{\rho_i \xi_i(\phi^n_{(j,k)})\Delta x \Delta y \Delta z}{\Delta t \cdot p^n_{v,sat}} (p^n_{v(j,k)} - p^{n-1}_{v(j,k)}) \end{aligned} \tag{3.10}$$

The coefficients G are fully described in Appendix C. Equation 3.10 may be further simplified in the same manner as equation 3.8 to yield:

$$[G]\{p_v\} = [S] \tag{3.11}$$

where [G] is an N x N matrix, [S] is the right-hand side 1 x N matrix, and the vapor pressure matix $\{p_v\}$, of size 1 x N, may then be calculated in the same manner as the temperature matrix {T} described previously.

Figures 3.11 and 3.12 illustrates the conditions for nodes at the exterior and interior surfaces of the brick. The full equations for both heat and vapor transfer for these two conditions are in Appendix C. As a final assumption, the latent energy required for the phase change of moisture is not included in these conditions.

In summary, so far in this chapter, the heat or vapor transfer phenomenon affecting each node are determined, the discretized equations are written, the equations are rearranged in terms of individual temperatures or pressures, and the coefficients relating to each temperature or vapor pressure are entered into the matrices described in equations 3.8 and 3.11. Once all of the nodes of the assembly have been considered, the right-hand matrix [R] or [S] is multiplied with the inversion of the [C] and [G] matrices. The product is the temperature and partial vapor pressure profiles, or matrices {T} and $\{p_v\}$. The partial vapor pressures may then be converted into the profile of relative humidity for the given time step.

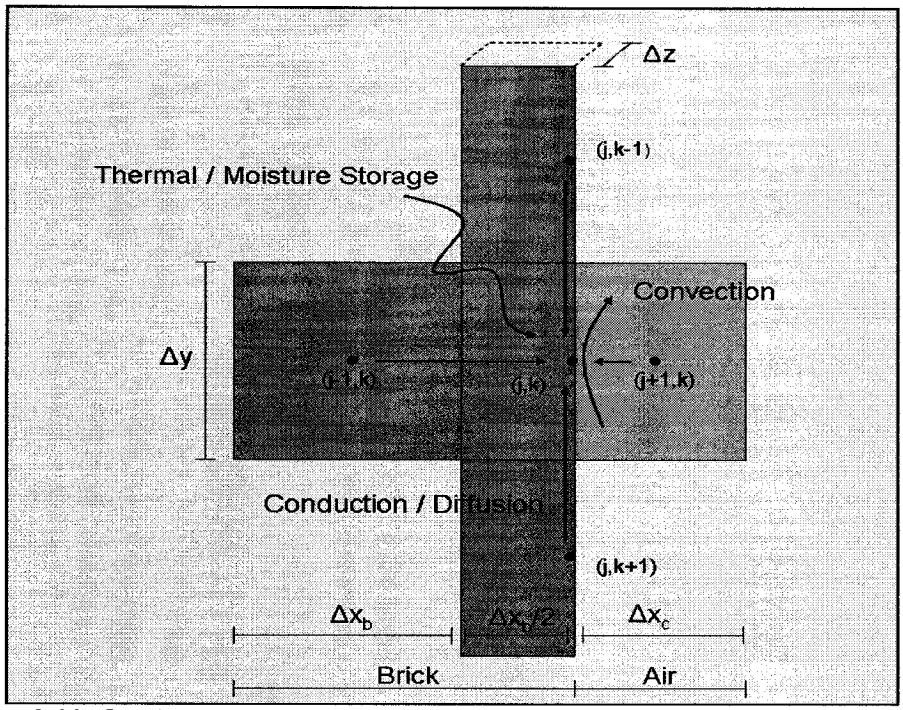

Figure 3.11: Graphical representation of heat and mass balance for brick surface node

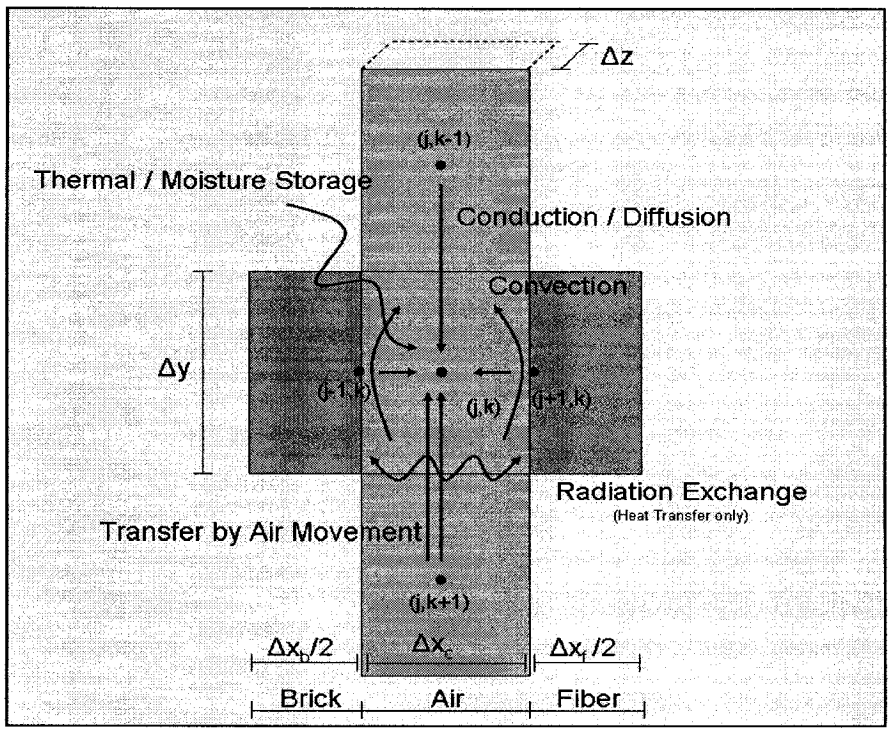

Figure 3.12: Graphical representation of heat and mass balance for air cavity node

3.4 Model Results

In this section, some simulation results are presented. Figure 3.13 demonstrates the temperature profile for the surfaces of material across the assembly and for the cavity air at a height of 1.50 meters. Figure 3.14 shows the cavity air velocity during a typical 48-hour loading period. Figure 3.15 allows the visualization of the relative humidity profiles during a 10-day cyclic loading period with conditions identical to those described previously. Finally, figure 3.16 shows the profile of relative humidity over height within the cavity only. In all cases, the boundary conditions are as described in section 3.2.2. The loading is cyclical for heat transfer, while the brick is considered wetted at the beginning of the testing period, with no subsequent rainfall. Under these conditions the maximum driving air pressure reaches a peak of approximately 3000 Pa.

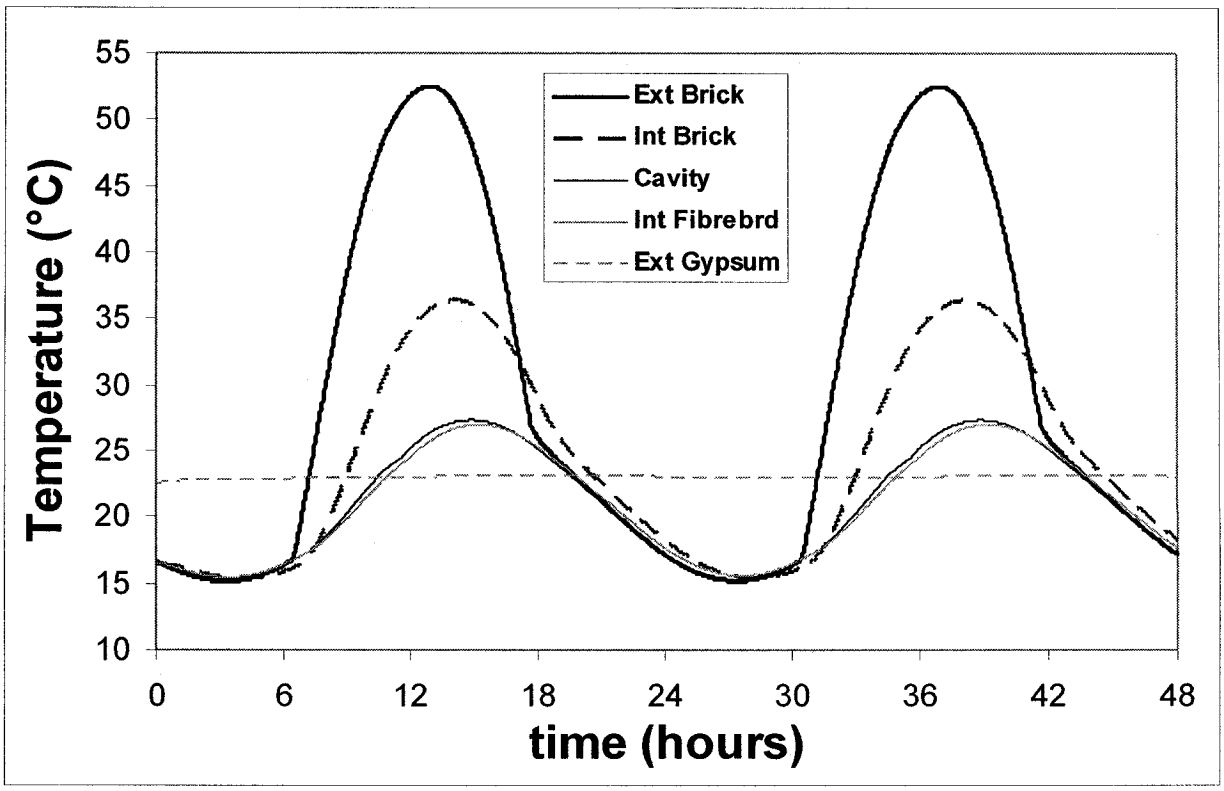

Figure 3.13: Temperatures at wall assembly surfaces and within the cavity for typical 48-hour period.

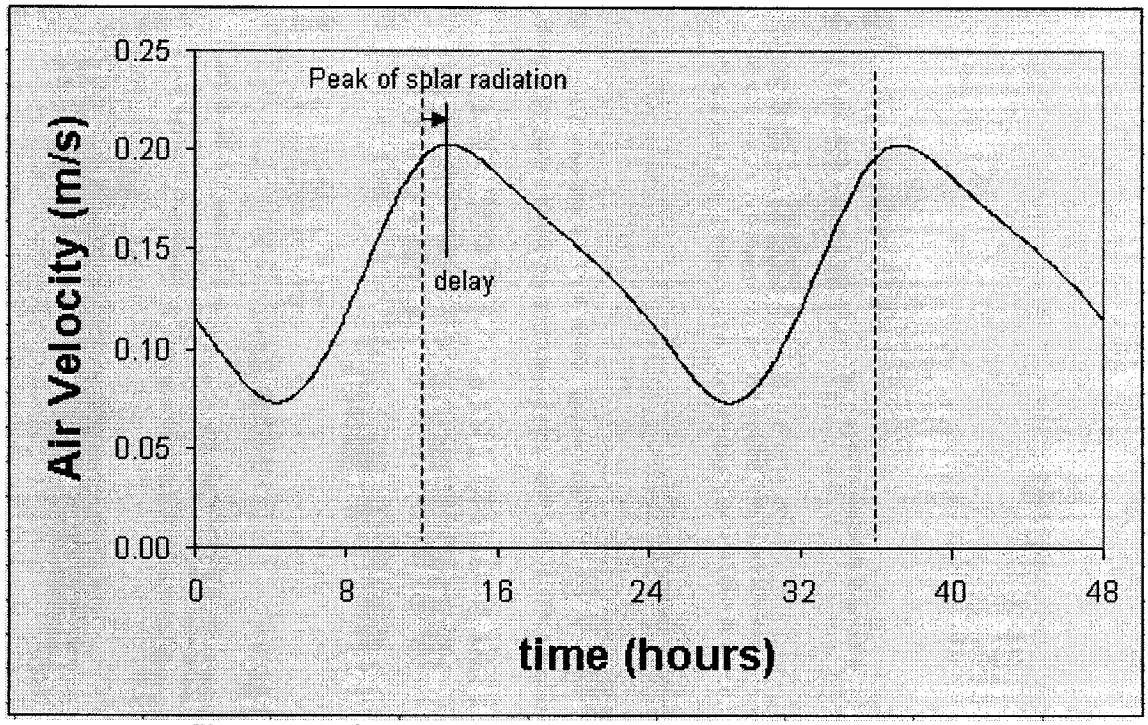

Figure 3.14: Cavity air velocity for a typical 48-hour testing period

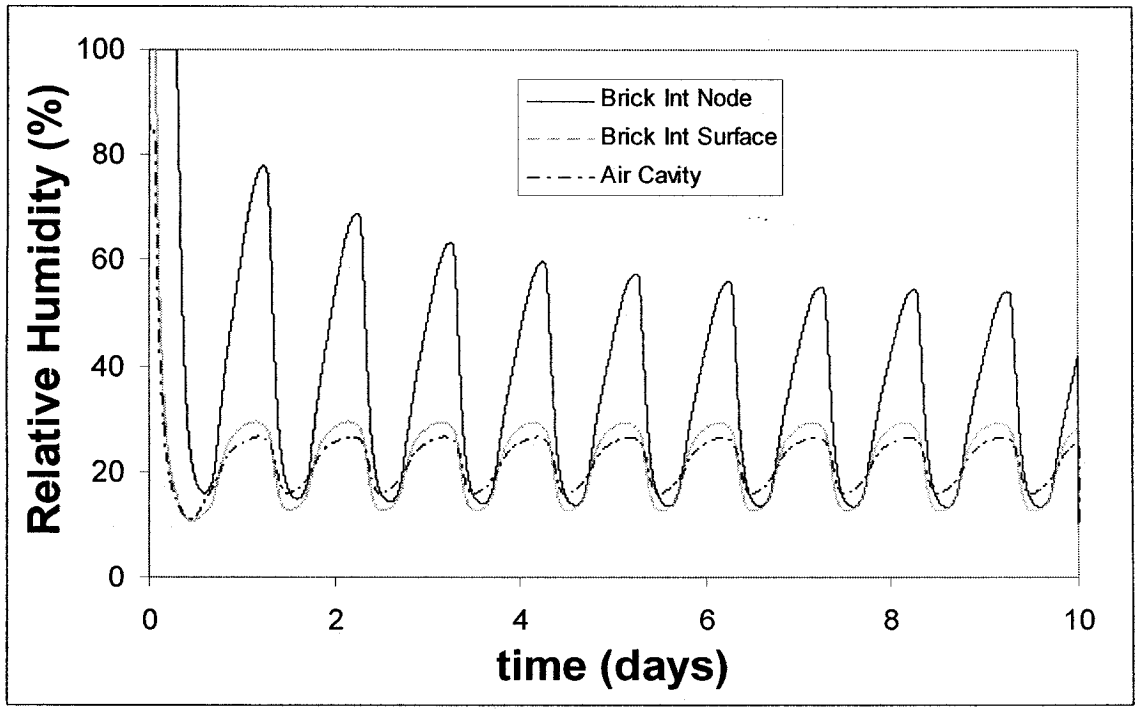

Figure 3.15: Relative humidity at an interior brick node, cavity-side brick surface and in the cavity air over 10 days at a height of 1.5 m, given an initial relative humidity in the brick of 99.93% with no subsequent rainfall).

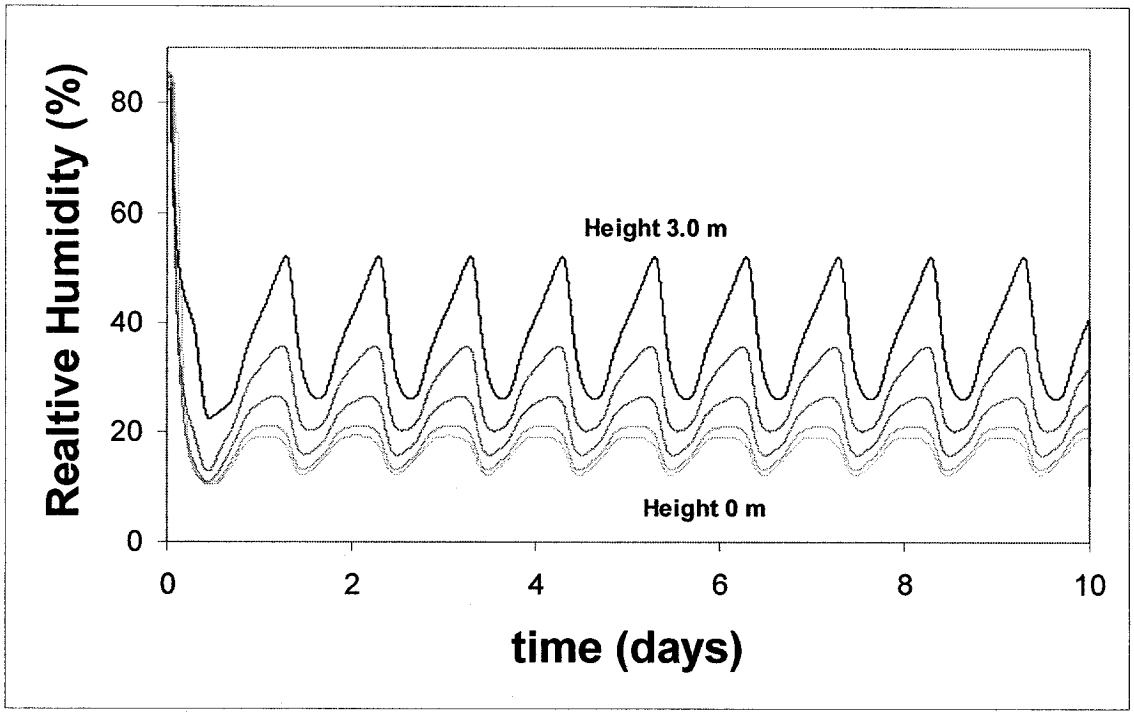

Figure 3.16: Relative humidity versus height within cavity at intervals of 0.75 m, given initial air relative humidity is 85% with no subsequent rainfall.

3.5 Analysis of Results

Figure 3.13 demonstrates the temperature profile throughout the wall assembly on all surfaces, as well as the cavity air temperature for a typical 48-hour testing period. It is clear that the solar-radiation exposed outside surface absorbs a tremendous amount of heat, then transfers much of this heat through the assembly. The delay between the curve peaks is to be expected as due to the heat capacity of the brick. It is also important to note that the temperature of the surface of the fiberboard does not vary significantly from that of the cavity air, indicating that a significant quantity of heat has been evacuated from the cavity by air movement.

Figure 3.14 demonstrates the cavity air velocity for a typical 48-hour testing period for the given conditions. The profile demonstrates clearly the peak of the velocity to occur at the same time as the peak of the interior surface temperature.

This is a result of the air pressure difference being maximal at that time and therefore driving the air flow.

Figure 3.15 demonstrates the relative humidity profile for the given set of conditions over a period of 10 days to allow for drying of the brick. An internal brick node, a cavity surface brick node and the cavity itself are shown. These values are taken at the central node within the network, all at a height of 0.75 m. It may be noted that while the relative humidity in the cavity and at the brick surface remains relatively stable, the brick dries significantly.

Figure 3.16 demonstrates the relative humidity profile at height intervals of 0.75 m from bottom to top of the cavity. While the temperature in the cavity increases slightly with height (see section 4.1), there is a significant accumulation of moisture in the air before it exits the cavity. It may be presumed that a significant quantity of moisture is evacuated along with the air.

3.6 Conclusion

This chapter has reviewed the entire process of the development of the numerical model. The objectives, the assumptions, the characteristics, the methodology and equations, the results and some analysis of the model were all presented. The results, however, require verification to be considered to accurately reflect the real-life scenario. The following two chapters present projects aimed at the verification of the numerical model. In Chapter 4, two initial projects are presented to which model results will be compared.

Chapter 4: Initial Model Verification

This chapter presents two projects that were used for the verification of the model results. These projects allowed the validation research to continue with the particle image velocimetry project (Chapter 5), with knowledge that the model results were reliable. The first project involves the comparison of the temperature profile within the cavity with analytical results from equations from the literature. The second project involves the evaluation of the air velocity within the cavity of a large-scale setup using an anemometer.

4.1 Analytical Equations Project

One means of verification of model results is by comparing said results to those obtained from analytical equations derived in the literature. Hens (2005) developed a set of equations that can provide a profile of the cavity air temperature.

4.1.1 Verification with Analytical solution

Hens (2005) provides the following equation to determine the cavity temperature in terms of height:

$$\theta_{cav} = \theta_{cav,\infty} - (\theta_{cav,\infty} - \theta_{cav,0}) \exp\left(\frac{-z}{b_1}\right) \tag{4.1}$$

where $\theta_{cav,\infty}$ is the temperature at the top of the cavity [°C], $\theta_{cav,0}$ is the temperature at the bottom of the cavity [°C], z is the height under consideration [m] and b_1 is a coefficient that may be calculated as:

$$b_1 = \frac{\rho_a c_{p,a} d_H v_a}{h_{cv}(2 - C_1 - C_2)} \tag{4.2}$$

where ρ_a is the density of air [1.2 kg/m^3], $c_{p,a}$ is the specific heat of air [1000 J/kgK], d_H is the hydraulic diameter of the cavity [0.025 m], v_a is the velocity of

the air [m/s], and h_{cv} is the convective heat transfer coefficient [W/m^{2}K]. The coefficients C_1 and C_2 may be calculated by the following:

$$C_1 = \frac{h_{cv}\left(h_{cv} + h_r + \frac{1}{R_2}\right) + h_r h_{cv}}{D} \tag{4.3}$$

$$C_2 = \frac{h_{cv}\left(h_{cv} + h_r + \frac{1}{R_1}\right) + h_r h_{cv}}{D} \tag{4.4}$$

In these equations, R_1 is the thermal resistance of the brick cladding [m^{2}K/W], R_2 is the combined thermal resistance of the backwall [m^{2}K/W], h_r is the radiative heat transfer coefficient [W/m^{2}K], and the coefficient D may be calculated by equation 4.5.

$$D = \left(h_{cv} + h_r + \frac{1}{R_1}\right)\left(h_{cv} + h_r + \frac{1}{R_2}\right) - h_r^2 \tag{4.5}$$

It is to be noted that all assumptions used in the model, as well as the boundary conditions presented in Chapter 3, are used in the preceding analytical equations. The same temperature and cavity air velocity conditions, over time, used in the model were applied here.

4.1.2 Comparison of Results

Equation 4.1 (and its subordinates) was used to calculate the temperature profile within the cavity at 0.33 m intervals from the bottom of the cavity (0 m) to the top (3 m). Figure 4.1 demonstrates the results yielded from Hens' analytical equations. Figure 4.2 demonstrates the model results for the same intervals and conditions. Comparisons between the two can be drawn to determine the reliability of the model results for heat transfer. It should be noted that since the values of the curves are very close, only peak temperatures of the first day of loading are shown to improve visibility. As for the discrepancy between the curve forms, it appears the exponential nature of Hens' formula causes larger

temperature differences at the successive heights before the peak and smaller ones after the peak as opposed to the model's more even distribution.

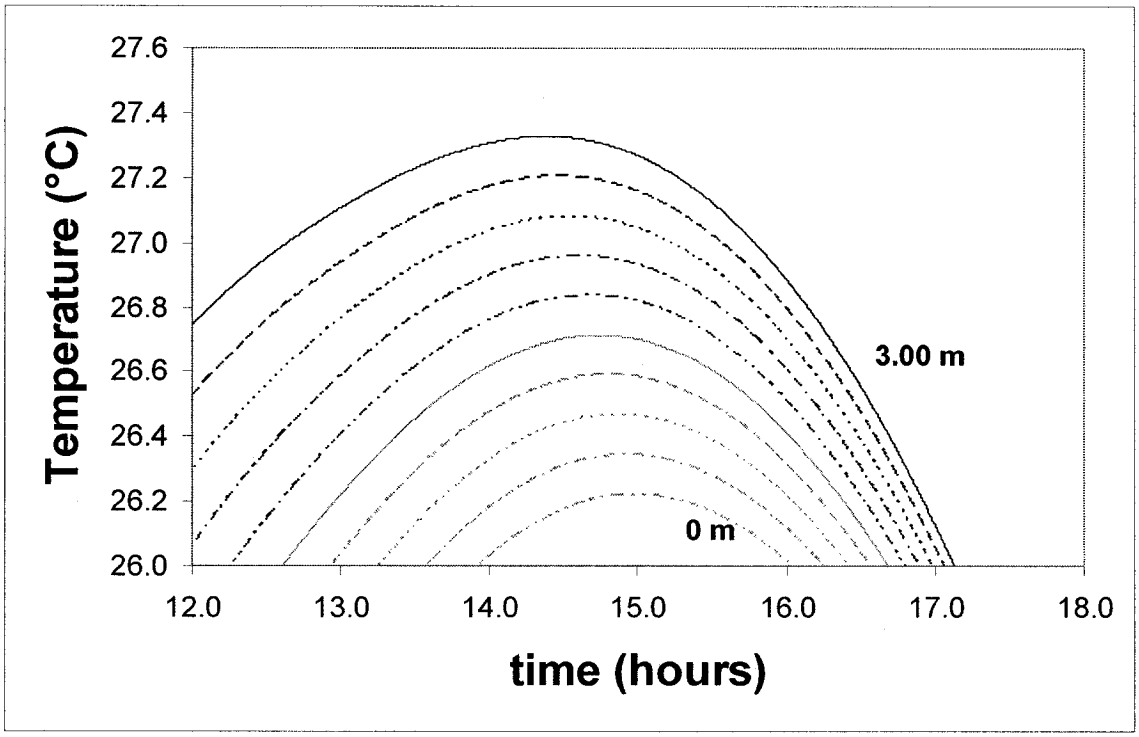

Figure 4.1: Maximum temperatures (°C) at 0.33 m intervals from the bottom to the top of the cavity during the first day (analytical results based on equations 4.1 to 4.5).

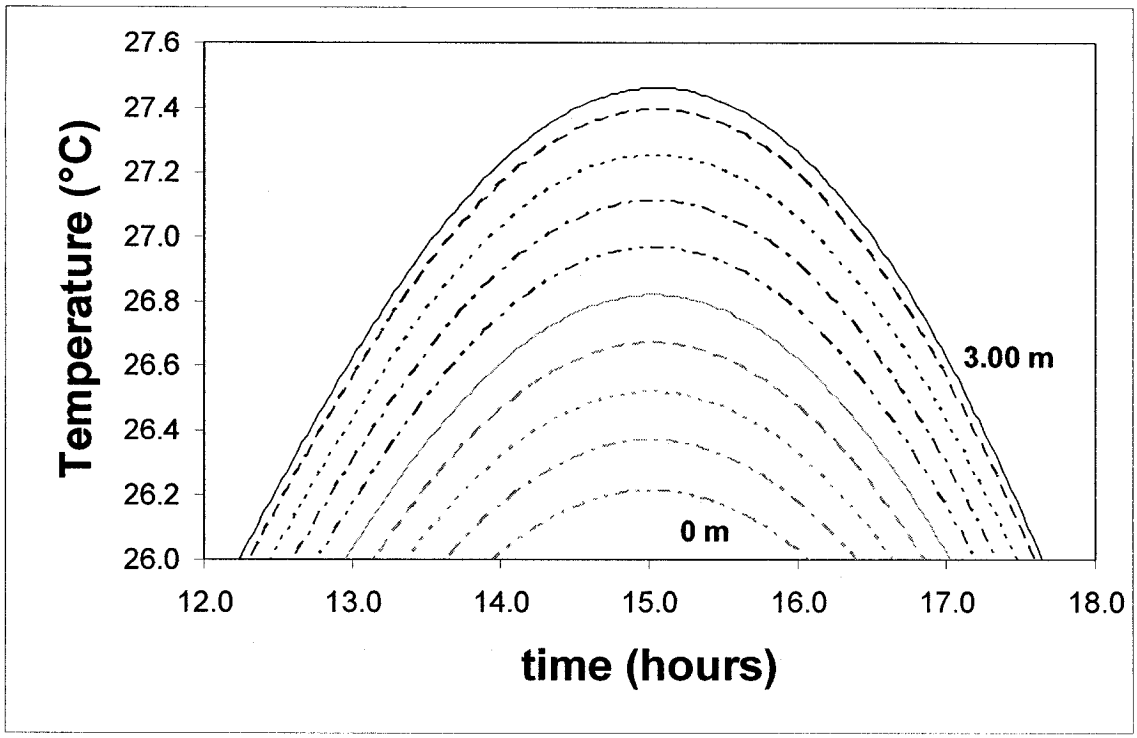

Figure 4.2: Maximum air temperatures (°C) at 0.33 m intervals from the bottom to the top of the cavity during the first day (model results).

While the shape of the curves is different, some trends observed between the two figures are in relatively good accordance. The maximal values are obtained at the same time, approximately 15:00, while the temperature at the base of the cavity is the same at 26.2°C. The maximum temperature is slightly lower, at 27.3°C from 27.5°C, which represents an error of 0.7%. The distribution of the curves in the cooling phase is also quite comparable. The variation in results during the heating phase reflects the exponential nature of the analytical equation, while the model equations create a more even distribution. It is therefore reasonable to conclude that the model results are comparable to those obtained analytically, at least during the peak and cooling phases.

4.2 Anemometer Experiment

The second project involved the evaluation of the cavity air velocity at three heights within a large-scale experimental setup. The velocity was measured using a uni-directional anemometer that was inserted into the cavity air flow. By

applying the law of conservation of mass, the values obtained at each given time interval should be approximately the same within the range of experimental error.

4.2.1 Experimental Setup & Procedure

This experiment was a precursor to the large-scale particle image velocimetry experiment which is the focus of Chapter 5. As such, the experimental setup was the same for both experiments, and therefore will be explained more in detail in section 5.2. For the purposes of the anemometer experiment, figure 4.3 allows a visualization of the setup used. A test hut with controlled interior conditions is sealed with an insulated backwall. A brick wall is then placed in front of the backwall with the 25 mm air cavity maintained between them. Both walls are held suspended in place by gantry cranes and counter-weights. The cavity is sealed on all sides by a polyethylene sheet, with three small holes punctured on the side to allow the anemometer to be inserted into the cavity for measurements. The solar radiation is simulated by means of heat lamps maintained in a large, open box placed directly in front of the brick wall. The interior of the box is lined with aluminum foil to prevent excessive absorption of heat by the box's wood frame. Infrared thermography was used to verify the lamps configuration provides a uniform heat flux on the wall.

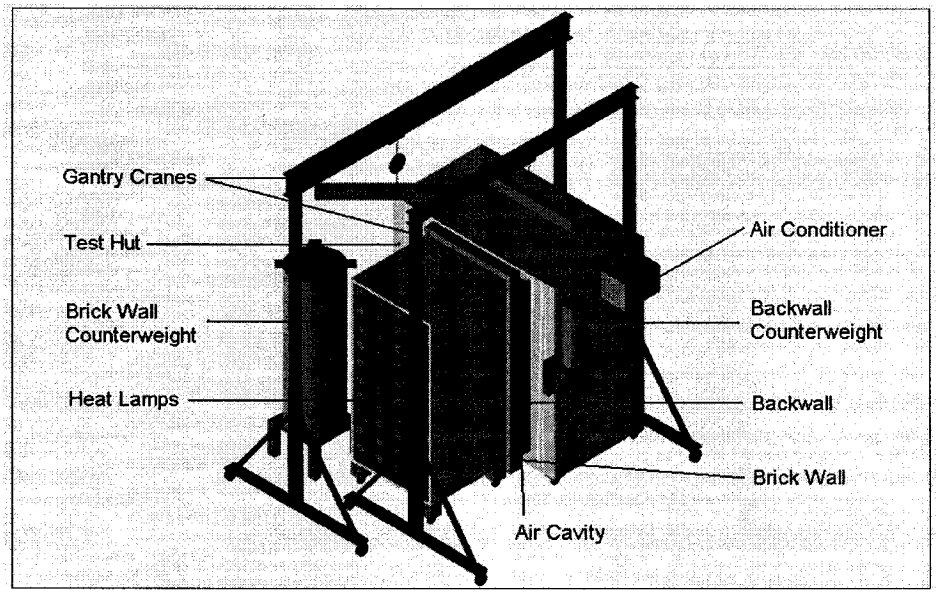

Figure 4.3: Experimental setup for cavity air velocity evaluation with the anemometer (Edelstein, 2007)

The anemometer used for the experiment is a VeleciCalc brand no. 8346 with a specified accuracy of 0.015 m/s or 3%, whichever is smaller. It functions with a hot-wire tip which must be placed perpendicular to the air flow direction. The anemometer is shown in figure 4.4. Velocity measurements are taken at three heights in the cavity, at 300 mm, 1200 mm and 2100 mm from the bottom of the brick wall, which has a total height of 2.4 m. The measurements are taken every 30 minutes for a 15-hour testing period, the first 8 hours of which the heat lamps are turned on to simulate solar radiation. The air velocity is measured in the air flow in the cavity, along a vertical lines joining a bottom weephole and a top vent, described previously. This is in accordance with the findings of Straube *et al.* (2004) where the tubular nature of the air flow path was previously presented. Thermocouples are placed within the wall assembly to monitor the temperatures of the outside brick cladding surface, the cavity-side surface of the brick and the cavity-side surface of the fiberboard. A thermocouple is also placed on the indoor side of the backwall to monitor interior conditions, which are constant at 16°C. The laboratory temperature varied between 21 °C and 24 °C during the test. The positions of the thermocouples and the anemometer are shown in figure 4.4.

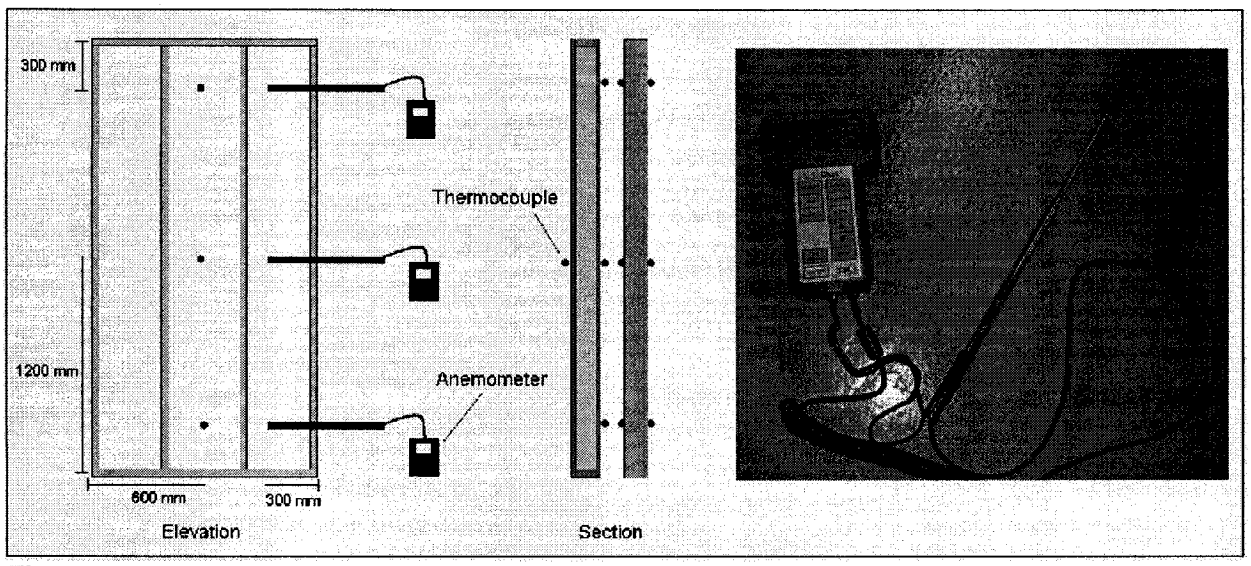

Figure 4.4: Placement of thermocouples and anemometer within wall and picture of anemometer used for experimentation.

4.2.2 Comparison of Results

The results obtained from the experiment are shown in figure 4.5, while the results obtained from the model for identical conditions can be seen in figure 4.6.

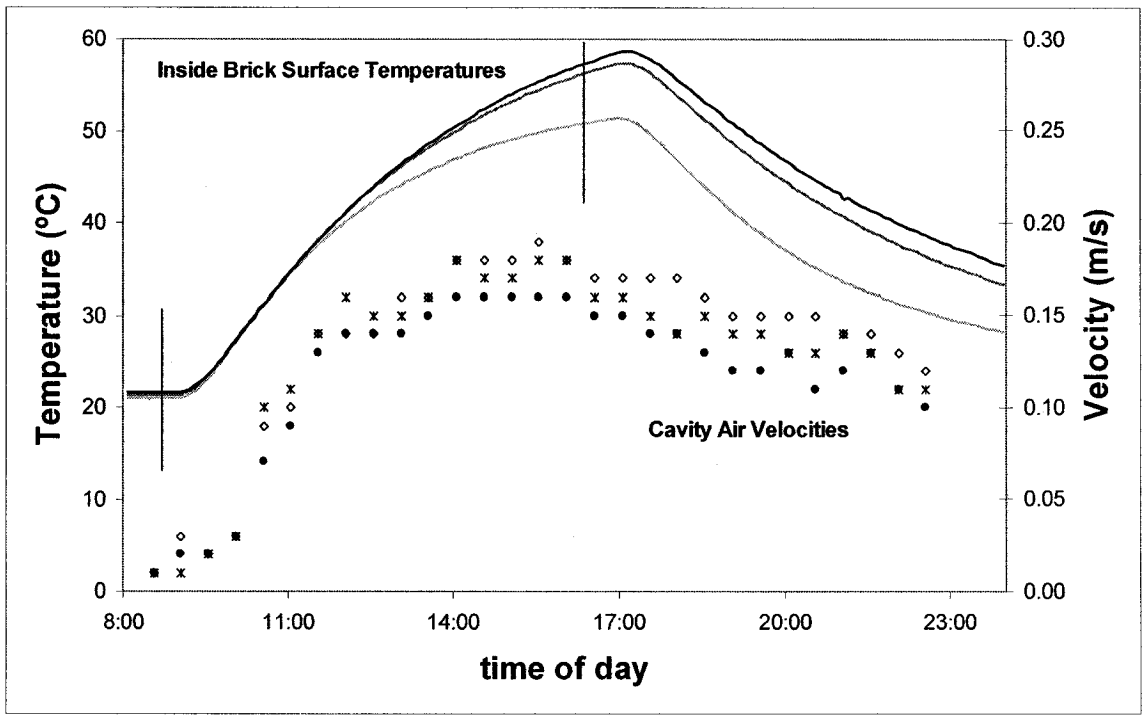

Figure 4.5: Anemometer experimental results. The full dots represent measurements at the bottom of the cavity, hollow dots the top of the cavity, and x marks the center of the cavity

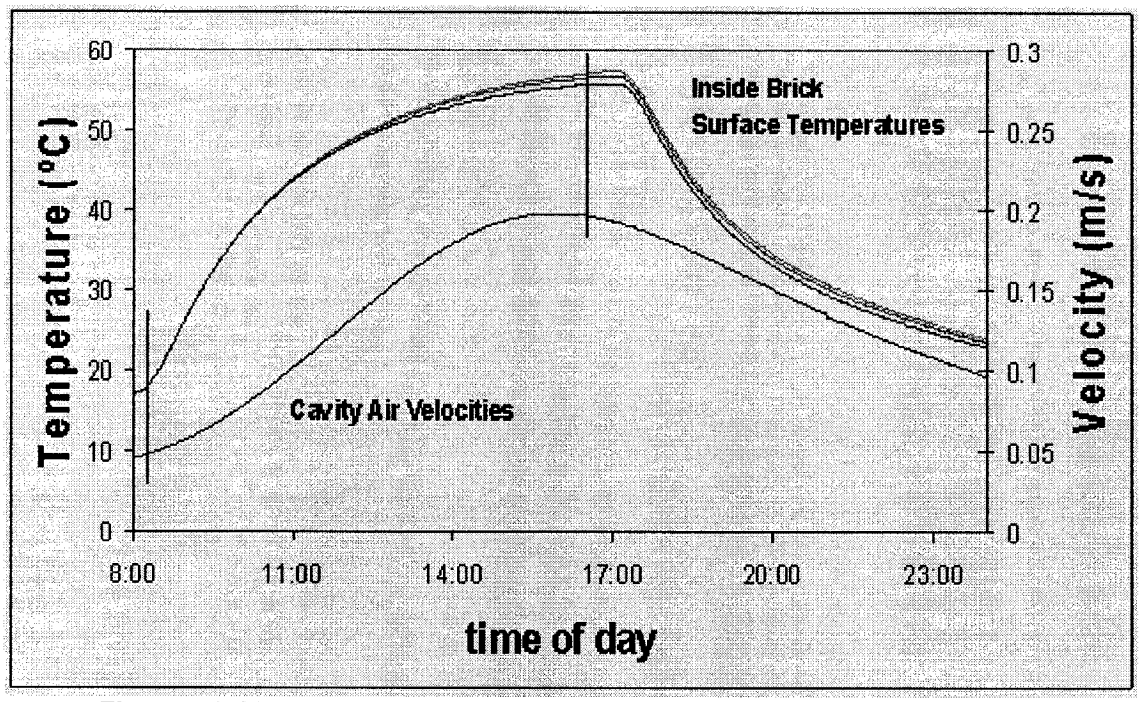

Figure 4.6: Model results for conditions identical to the anemometer experiment.

The laboratory conditions, test hut conditions and the inside brick surface temperature are input in the simulation to allow comparison of simulation and experimental results. .To do this, a constant solar radiation load was maintained from 8:00 to 17:00 to replace the sinusoidal input used in the previous chapter. As shown in Figures 4.5 and 4.6, both the experimental and model inside brick temperature curves achieve a similar peak value before descending precipitously when the lamps are removed. The velocities measured by the anemometer, although not all exact to one another at each testing time, are within a reasonable margin of error. For example, the peak measurement of 0.21 m/s at 16:00 compares to the peak modeled measurement of 0.20 m/s at the same time, for an error of about 5%., keeping in mind that the anemometer error is 3%. Some discrepancies can be attributed to some air pressure losses, e.g. due to exfiltration through the brick wall or through the small holes in the polyethylene barrier used for testing. The trend demonstrated by the experimental velocities nevertheless shows very good accordance with those obtained by the model. It was also noted that it took approximately 2 to 3 hours of heating of the wall by

the lamps for any significant velocities to be measured within the cavity. This information would be used to develop the procedure for the PIV experiment in Chapter 5.

Other alternative investigations with the anemometer experiment yielded interesting results. At certain locations and times, the anemometer was turned by 90 degrees to measure transverse velocities perpendicular to the flow. Low magnitude readings, of approximately 0.01 to 0.03 m/s, were measured in this direction, especially at the bottom location. This would seem to indicate a small region of turbulent flow near the bottom weepholes. This will also be further investigated in Chapter 5.

Finally, the anemometer was moved inward and outward within the cavity by a few centimeters to measure the air velocity on either side of the central air flow that runs between the weepholes. As expected, there was a steep drop in air velocity as the anemometer was moved from one side of the flow to the other. This would indicate that the flow path representation derived by Straube (as shown in section 2.5.1) is a correct assumption for modeling.

4.3 Conclusion

This chapter has presented two verification projects to support the model results from Chapter 3. The analytical equation project permitted favorable comparison of the model results for cavity air temperature, under certain conditions. The anemometer results provided a good fit to compare the model cavity velocity to that in a large-scale experimental setup. With the magnitude of the results and general characteristics of the air flow known, it is possible to proceed to a larger-scale verification project. The next chapter discusses verification of the model with qualitative and quantitative study of the air flow in the cavity by means of particle image velocimetry.

Chapter 5: Particle Image Velocimetry

This chapter presents the next experimental project completed to evaluate the movement of air within the cavity using Particle Image Velocimetry (PIV). The principles of PIV are presented first, followed by the experimental setup and procedure. The limitations of PIV applied specifically to this project are then discussed. Finally, the experimental results are presented, followed by analysis and conclusions.

5.1 General Methodology

A study of air movement within a tall, thin enclosure would not be complete without the visualization of the air movement, as well as an experimental determination of the velocity of the flow field. The technique of Particle Image Velocimetry is selected to provide these two types of data. Adrian (2005) defines PIV as "the accurate, quantitative measurement of fluid velocity vectors at a very large number of points simultaneously". In this section, the four stages of PIV will be discussed: seeding, illumination, recording and post-processing. An illustration of this methodology can be seen in figure 5.1.

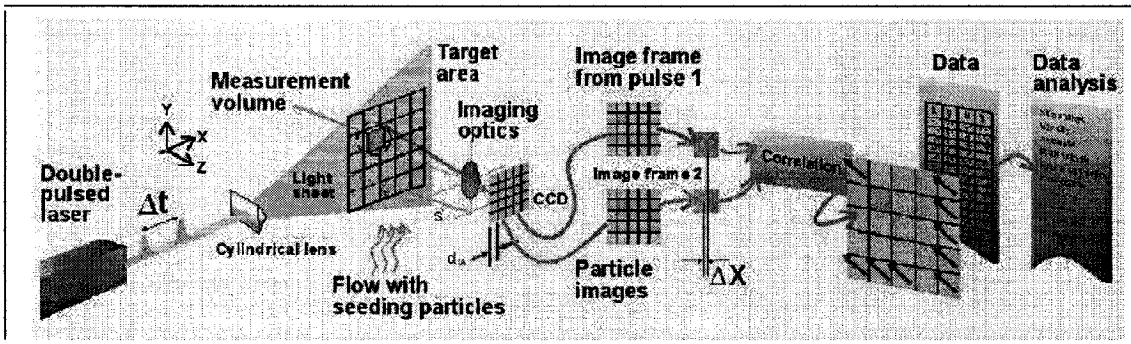

Figure 5.1: Methodology of particle image velocimetry (Chabot and Grooten, 2006)

5.1.1 Seeding

In order to view an air flow path within an enclosure, the air must be "seeded", or loaded with small and light particles that can be illuminated by a light source and

visualized by a camera. Thus, PIV measures the velocity of the tracer particles that accurately follow the flow. While PIV as a technique is now over 20 years old, it traces its development to earlier techniques, such as laser Doppler anemometry (Adrian, 2005). At that time, a compromise between the reduction of particle size to improve flow tracking and increasing the particle size to improve the scattering of light became necessary (Melling and Whitelaw, 1973). Melling (1997) also states that, in general, larger particles will give stronger signals to the camera. However, it is also true that, for relatively low velocity experiments, such as the one presented here, a larger sized particle may not be adequately carried by the air flow, or may alter the flow itself as it may not be neutrally buoyant. Common seeding particles for air flow measurements include oil or water droplets, smoke, fog, or tracer gas, depending on the application.

5.1.2 Illumination

According to Dantec Dynamics (2005), illumination of the flow field must always be perpendicular to the recording device, or camera. Illumination is almost always done by means of a laser-emitting device. Most often, a mirror placed at a 45 degree angle to the laser-emitting device redirects the light field to the desired measurement region in the flow field. The light sheet is produced by placing a divergent optical lens between the laser and the mirror. The illumination itself occurs as a series of pulses, similar to a stroboscopic light. The velocity of the flow field can thus be established by dividing the distance traveled by a particle by the known time between pulses. The light pulses must have short pulse durations to ensure the particles do not move significantly during illumination, thereby freezing the motion of the seeding particles.

5.1.3 Recording

The recording of the flow field is completed in sets of image-pairs, with an exact, predetermined, time-separation between them. The camera and laser must therefore be synchronized to a pulse-timer that will allow images to be recorded as the light pulses are engaged. The recorded images are then transferred via

an image acquisition card (frame grabber) to the computer. A large sample of images is usually taken as to allow for greater accuracy of results. This is especially important if the seeding is not uniform, and/or if a high degree of precision must be obtained for the velocity of the flow field. A particular precaution must be taken during the recording period: as a laser is being employed, it is important to avoid contact with the stream of light and to wear laser safety glasses. A final step that must be taken before the camera is moved is to record a calibration marker, such as a ruler, tape measure or any other object for which the exact width or length is known (see figure 5.2 for this experiment). This marker will be used in the post-processing phase to determine the distance traveled by particles between the two images of a pair by converting the values from pixels to the length units.

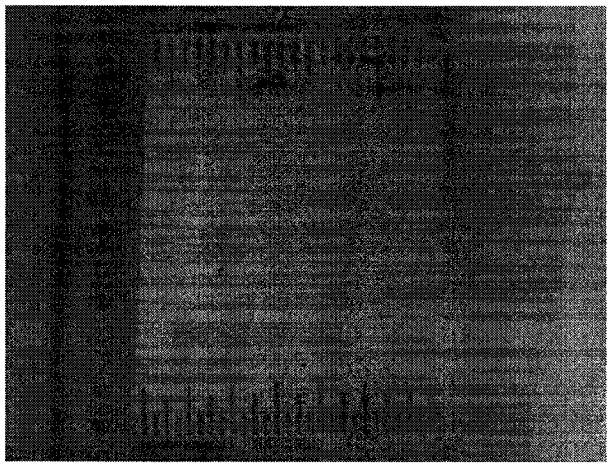

Figure 5.2: Image Calibration Marker for PIV Experiment

5.1.4 Post-Processing

Once the complete set of data is recorded, the final stage of PIV is the post-processing and analysis of the images. Procedures for post-processing may vary depending on the desired measurement region, type of flow, etc.; therefore the description here is specific to this study. Firstly, the best and most representative images, where individual particles can be clearly seen in formation, must be selected. Generally, images having "noise" or excessive light are excluded, as well as images for which little to no flow is visible. Next, the

images are cropped so that only the region of study can be seen. The program will then read the images and determine the correlation from between the image pair.

In most PIV programs, the correlation is done by comparing each section of the grid, usually 16 or 32 pixels squared, to the corresponding section of the grid of the second image of the pair. This can be visualized at the center of figure 5.1. The general movement of the particles in each region of the vector map is then established numerically. This produces what is commonly known at the particle displacement grid. Once the distance traveled by particles from one frame to the next is known, these values are divided by the preset delay (in the case of this study, 1 millisecond). As such, the vectors of the velocity field may be established. Further programs may calculate the x and y components of the air velocity. Figure 5.3 demonstrates an example of a vector map.

Programs also exist to eliminate aberrations, or "bad" vectors from the field that tend to skew the results. In these cases, vectors inconsistent with their surroundings are replaced by a median value of their surrounding vectors. It should be noted, therefore, that large areas devoid of particles must not be considered to prevent large errors as the program will recognize either a value of zero or an exceedingly high value for these areas. In this study, most images have few to no particles above their initial entry into the cavity. As such, the upper regions of the images are not considered in the analysis.

Once the velocity field has been established and corrected, the calculation of the average velocity for the entire field can be completed. This is done by calculating the magnitude and direction of the air velocity at each location of the matrix and making a global average for the field.

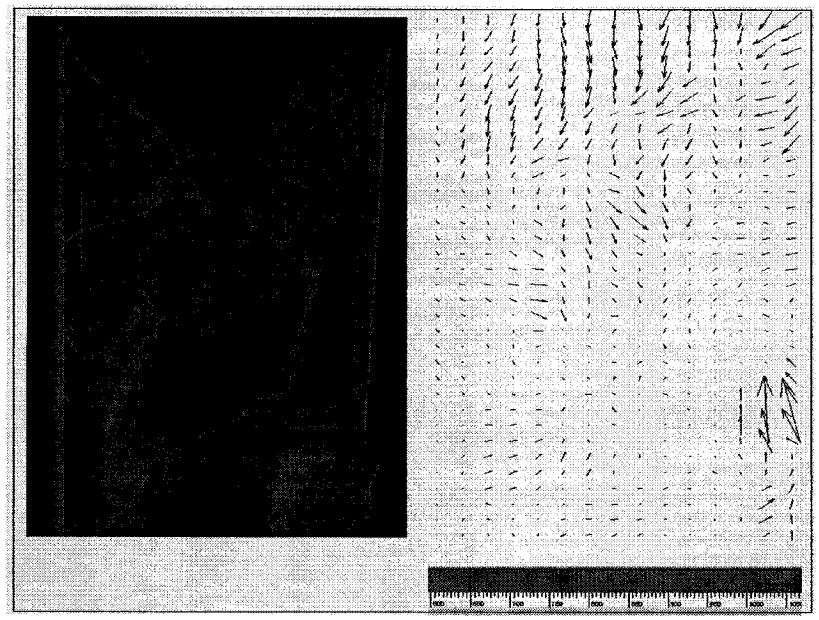

Figure 5.3: Image with corresponding vector map (Chabot and Grooten, 2006)

5.2 Experimental Setup

In this section, the experimental setup for particle image velocimetry is described. The wall setup used will be discussed, followed by the modifications made for PIV, and finally the PIV equipment that were added to the setup.

5.2.1 Wall Assembly Setup

The experimental setup used for the PIV experiment is the same as for the anemometer experiment discussed previously. The setup is located in a laboratory with ambient conditions. The brick wall, 2.40 meters in height by 1.35 meters in width, is constructed within a supporting steel frame. The clay bricks have a thickness of 90 mm and bonded with cement mortar. The backwall is composed of a weather barrier, a fiberboard panel of 12 mm thickness, a wood stud/batt insulation layer of thickness 89 mm, a polyethylene vapor barrier and an interior gypsum panel of 12 mm thickness. Between the cladding and the backwall, small wood spacers maintain a 25 mm air cavity width. The cavity is closed by a loose-fitted but airtight polyethylene sheet. Three weepholes are bored into the bottom and top of the wall, for a total of six, with two bricks of

spacing between each. These holes, approximately 10 mm by 55 mm in dimension, are the only areas of the cavity exposed to the laboratory conditions. Solar radiation is simulated on the outside surface of the brick by means of an optimally-placed array of 40 heat lamps placed within a reflective box. Thermocouples are placed at the top, middle and bottom of three surfaces, the outside brick surface, the inside brick surface, and the weather barrier surface. As well, relative humidity sensors are placed in the lab to monitor the exterior conditions, as well as inside a test hut, which is sealed to the backwall to maintain constant interior conditions. A data acquisition system is installed to tabulate the results as the experiment progresses. Figure 5.4 shows the wall setup as well as the wall as it undergoes heating by the simulated solar radiation.

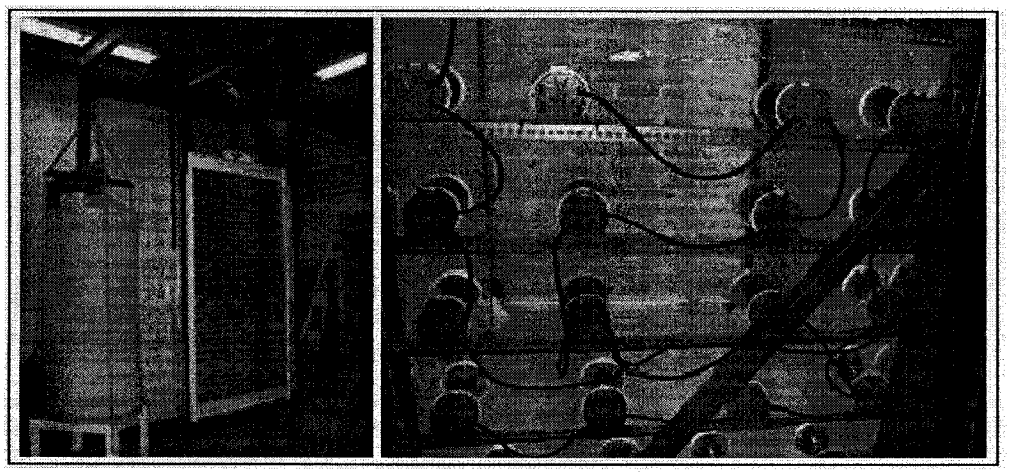

Figure 5.4: Wall assembly setup and simulated exposure to solar radiation

5.2.2 Setup modifications for PIV

Modifications to the wall assembly had to be carried out to allow for the installation of PIV equipment as well as for clear visualization of the images. Both the brick wall and back wall are maintained suspended in the air by gantry cranes to allow for the mirror to be placed below the cavity. As well, evenly spaced slots had to be cut out of the steel frame so that a clear visualization could be made of the entire 25 mm width of the cavity. Previously, part of the cavity had been obscured by the flange. Each of the slots was outfitted with a thin plexiglass window to allow for optimal viewing of the cavity during the

experiment. Finally, a layer of polystyrene insulation had to be placed on either side of the backwall for its width equal the width of the steel frame. This served a dual purpose: to avoid heat transfer from the backwall to the outside, as well as to ensure a flush side of the wall on either side of the cavity to facilitate the installation of the polyethylene and the plexiglass windows. The PIV equipment setup can be visualized schematically in figure 5.5. Figure 5.6 demonstrates a weephole that had been bored into the wall, as well as a view of the cavity with the polyethylene cover, the slot in the steel frame and the plexiglass window.

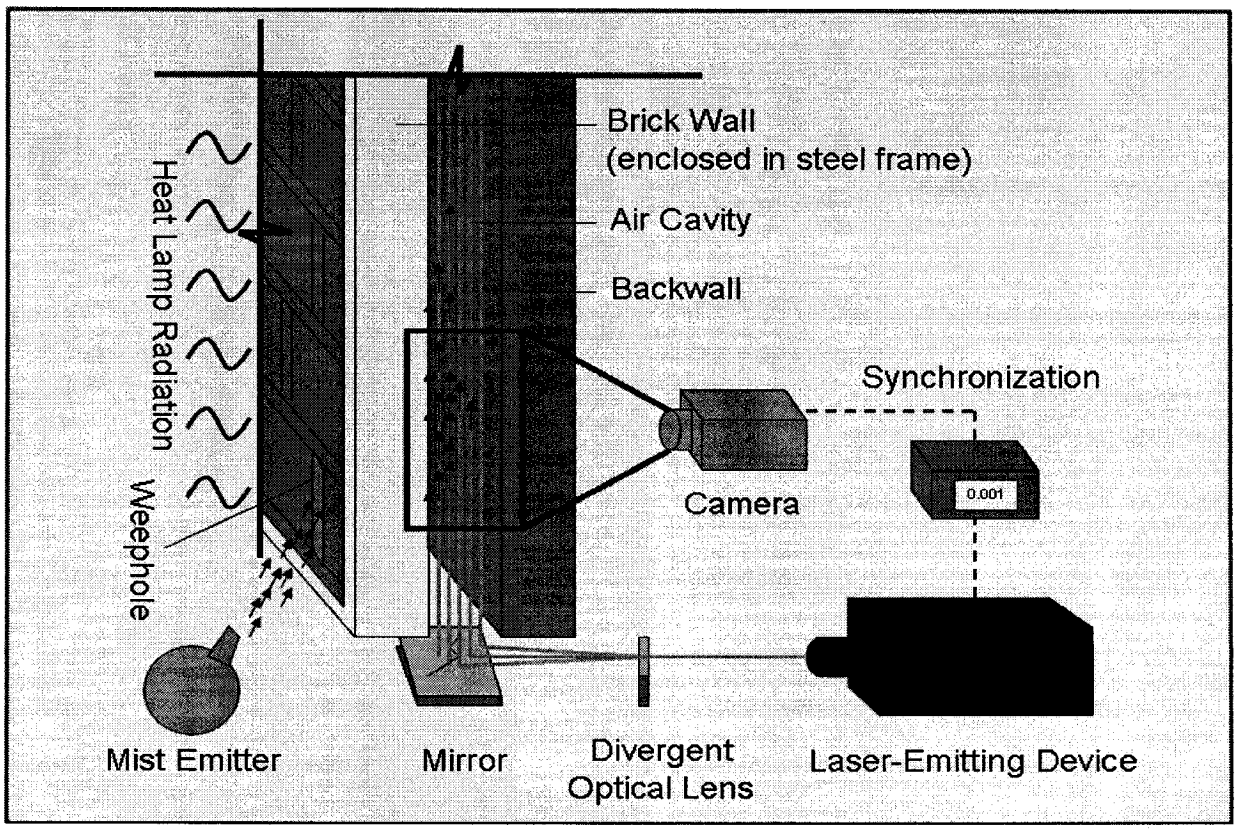

Figure 5.5: Schematic representation of the PIV experiment set-up

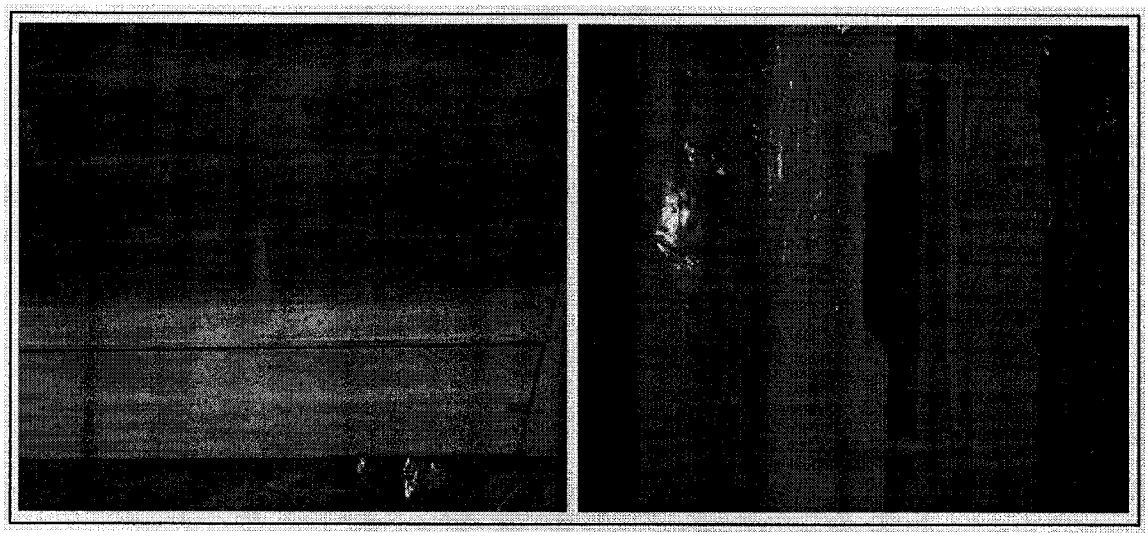

Figure 5.6: Lower brick wall weephole and cavity visualization slot

5.2.3 PIV Equipment Setup

The actual setup of PIV equipment can be done completely externally to the wall assembly. Experience has shown that the closer the air flow is to the camera, the clearer the images will become. Therefore, seeding of the air flow will be done with water vapor that is drawn into the wall via the bottom right weephole. The mist emitter is placed below the heat lamp box, and the nozzle is equipped with a PVC pipe that releases the mist near the weephole, but not directly in front of it so as to allow the flow to be undisturbed. The mirror is placed under the wall, and optical lenses are placed between the laser and the mirror to create the light sheet across the cavity. The camera is placed perpendicular to the cavity in front of the lowermost slot, which allows the flow to be visualized from the cavity-side of the weephole. The camera is connected to a computer that acts as a data-acquisition system. It should be noted that the data acquisition of the PIV is independent of the data acquisition for the thermocouples and relative humidity probes. The camera and laser are also connected to a box that synchronizes the shutter of the camera with the pulse of the laser. Pictures of the final PIV setup are shown in figure 5.7.

Figure 5.7: Experimental setup of PIV and close-up of the airflow seeding

5.3 Experimental Procedure

The anemometer experiment demonstrated that it would take approximately 2 to 3 hours after exposing the wall to the heat lamps for appreciable air velocities to develop within the cavity. Therefore it was decided that images would be taken starting at the third hour of exposure until the eighth hour, with intermediate measurements taken at every hour in between. There would thus be a total of six (6) testing periods. For each testing period, the following experimental procedure was followed:

- Ten (10) minutes before the test, the power generator for the laser is turned on to warm up;
- The laboratory lights are turned off;
- The mist emitter is checked to ensure the mist is being property drawn into the wall in sufficient quantities for adequate seeding of the flow;
- Laser safety glasses are put on;
- Just before the test, the synchronization box, connected to both the camera and the laser, is turned on and an image-pair delay time of 1 millisecond is selected;
- The software program "Videosavant" is initialized, the shutter mode for the camera and the proper configurations are verified;

- The time of the test and the image number of the first image frame of the test are noted (the frames follow sequentially from one test to the next);
- The camera is plugged in;
- The control signal manager is updated;
- The camera mode is set to live;
- Laser 1 (for the first image of the pair) and Laser 2 (for the second image of the pair) are turned on;
- The "record" button is engaged and the experiment runs for approximately 50 seconds. The program records 30 frames per second. Thus, 1500 images (or 750 image-pairs) are recorded with time differences of 1 millisecond from the first to the second image of the pair.
- When the test is complete, the lasers are placed on standby, then turned off along with their power generator;
- The synchronization box is turned off;
- The camera is unplugged to prevent overheating.

Once the six tests were completed after eight (8) hours of exposure, the lamps were turned off. The 9000 images collected (or 4500 image-pairs) were then exported for analysis. Due to a limited seeding area, analysis was done for only the bottom weephole, which would provide data for the first 8.5 centimeters of flow development in the cavity.

5.4 Errors and Limitations

PIV, by its nature, induces certain specific errors that need to be taken into account when analyzing the results. Two important sources of these errors are presented: perspective and parallax error. There are also two unexpected limitations to the experiment that could not be immediately corrected relating to the seeding vapor: evaporation and inconsistency.

5.4.1 Perspective Errors

According to Dantec Dynamics (2005), a perspective error occurs when particles have an out-of-plane movement. This only occurs for particles that are close to the border of the image. The camera will record a different distance than traveled in reality, and the vector produced will therefore be erroneous. Perspective errors can be seen schematically in figure 5.8.

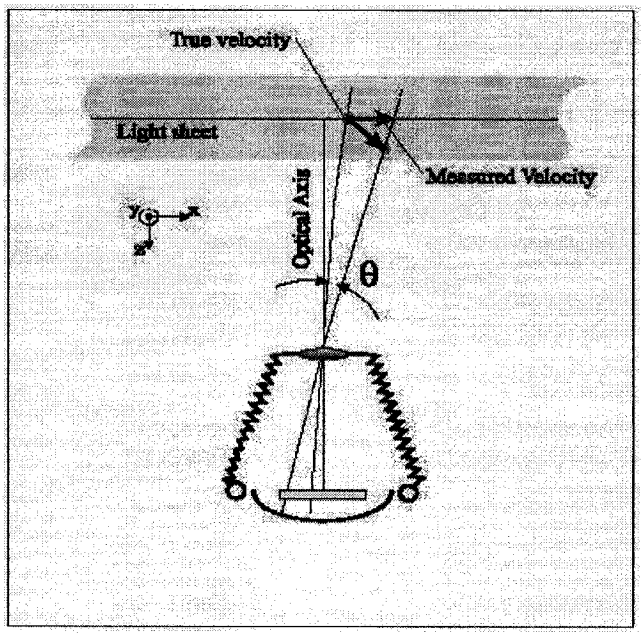

Figure 5.8: Perspective errors (Dantec Dynamics, 2005)

5.4.2 Evaporation of the Seeding Mist

The major limitation encountered was the evaporation of the seeding mist due to the high temperatures observed in the cavity. Temperatures as high as over 60°C were recorded on the inside surface of the brick, which caused almost all water particles to disperse and therefore become almost invisible to the camera, even with the benefit of the laser for illumination. The original intent of the experiment was to repeat this process for five (5) different heights along the cavity. Due to this limitation, it was impossible to visualize any flow above the bottom window, despite some effort at the second-lowest window. Future experiments will undoubtedly have to overcome this limitation and determine a more optimal seeding of the air flow.

5.4.3 Inconsistency of the Seeding Mist

By its nature, the mist emitter produces mist in an intermittent fashion. As such, at some moments there is an overabundance of mist pulled into the weephole, at others, none at all. Over the course of the 30-second testing period there was always an adequate amount of seeding. However, of the 1500 images produced during the time period, only a select few demonstrated particles clearly enough for good analysis. In many cases, the images were overly lightened due to excessive seeding. In others, there were no visible particles at all due to no mist being pulled into the wall at that particular instant. Overall, this limitation was overcome; however it did require careful and judicious selection of clearly seeded image-pairs.

5.5 Experimental Results

The most defining image-pairs that were recorded during each of the six (6) testing periods were selected. The final testing period, at 8.0 hours of exposure, is presented in table 5.1. The other five (5) testing periods, from 3.0 hours of exposure to 7.0 hours of exposure, can be seen in Appendix D. Table 5.2 and figure 5.9 provide summative results for all testing periods. The temperatures of the surface of the exterior and interior side of the brick, as well as on the interior cavity side of the backwall are also displayed for comparison. Two image-pairs were selected to be displayed for each testing period. The post-processed velocity vector map for these selected image-pairs is also shown. As the velocity map is a correlation between the image pairs, there is only one velocity map per set.

Table 5.1: Test Period 6

8.0 Hours of Heat Lamp Exposure

	Exterior Brick	Interior Brick	Cavity Backwall
Surface Temperature	61.76°C	57.45°C	39.22°C

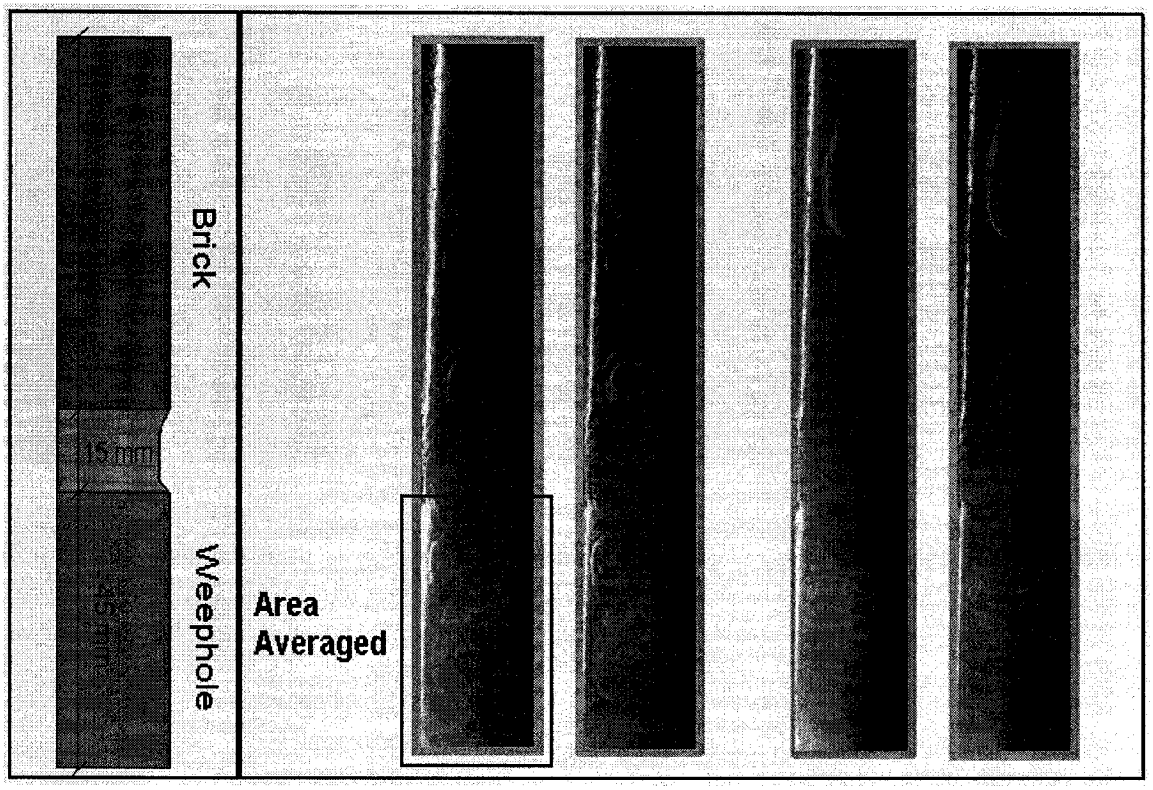

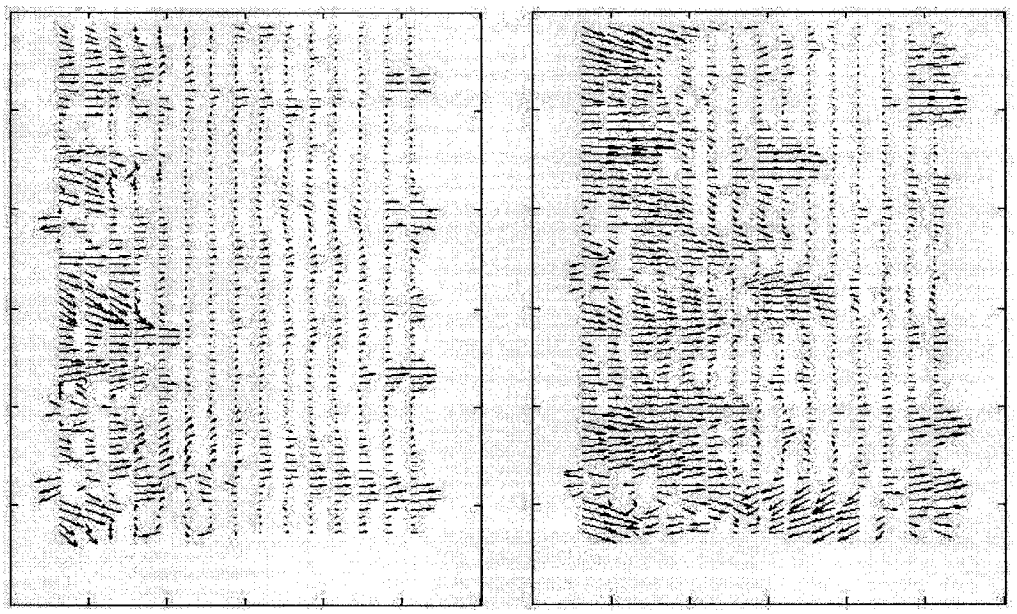

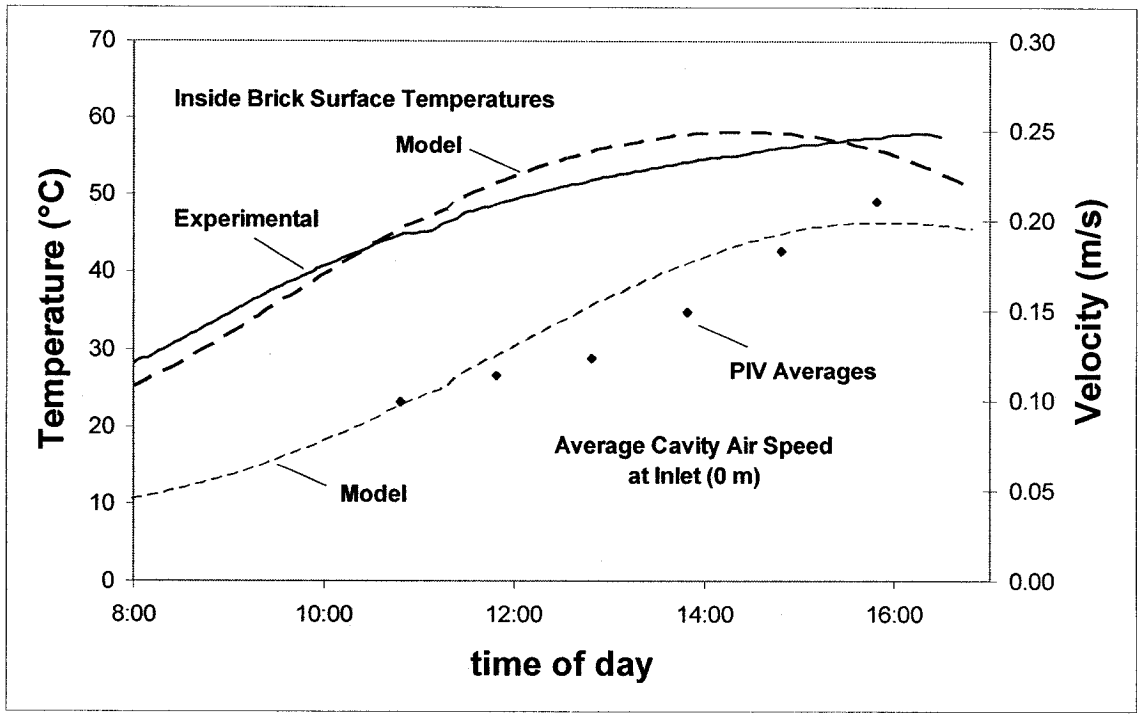

Figure 5.9: Comparison of PIV average air velocity results to model results for equivalent conditions.

Table 5.2: Summary of Average Results for PIV

	Velocity (cm/s)	Angle (degrees)	Corrected (degrees)	quantity of tests	Vectors	Total
Test 1	9.9125	94.787	4.787	8	975	7800
Test 2	11.378	97.872	7.872	8	1080	8640
Test 3	12.359	95.668	5.668	8	975	7800
Test 4	14.912	90.479	0.479	8	975	7800
Test 5	18.338	97.038	7.038	8	705	5640
Test 6	21.059	95.045	5.045	8	975	7800

It must be noted that only the visible seeded area of the cavity is calculated in the map; therefore the black area at the top of each cavity is not shown on the vector map. The average cavity air velocity results at each of the testing periods is presented, but these were calculated from particles selected from a wide cross section of the best 8 of the 750 image-pairs per testing period. In table 5.2, the

total number of vectors for each of the eight tests is presented, as well as the total of that number multiplied by eight. This is the total number of vectors that were used for the calculation of the average of the magnitude and direction of the velocity for each testing period. That number is dependent on the amount of visible flow in the selected tests. The ambient conditions of the laboratory were noted to be at approximately 24°C and 50% RH throughout all tests. The interior test hut conditions were maintained at approximately 16°C with relative humidity measurements varying between 70% and 80% throughout all tests.

5.6 Analysis of Results

The images displayed for the six tests all have a defined characteristic: a tendency for the air flow to be highly turbulent upon its entry into the cavity, followed by a transition to a more laminar state. As the bottom third of each image on the left hand side is the weephole entrance, the air flow passing through it turns immediately into small vortices that scatter within the cavity at unpredictable rates and locations. These are clear signs of turbulent flow. However, as the air begins to be driven up the cavity wall, the pattern tends to straighten out and take on an increasingly leveled-out, zigzag pattern. As this occurs, the flow is becoming increasingly laminar, and it can best be visualized on the first image-pair of test 4, the second image-pair of test 5 and the second image-pair of test 6.

The interior brick surface temperature does not seem to have a significant effect on the behavior of the air, as the general form of the air flow in the images does not change significantly from one test to the next. This could potentially be due to the relatively modest increase of about 12°C of the inside surface temperature of the wall over the course of the 6 tests. The velocity vectors have a general upward tendency. As the original PIV images were produced in the horizontal direction, the angles of the air flow had to be corrected by subtracting 90 degrees to their original value. As can be seen in table 5.2, the average vector at each test period is displaced at angles ranging from 0.5 to 7 degrees from the

horizontal. This is to be expected as the air velocity is entering the cavity horizontally from the left and is only beginning to move in a generally upward direction. Even still, the zigzag pattern taken by the air flow at greater heights would probably not produce vectors perfectly vertical.

The average velocity values taken from the PIV vectors fit well into the modeled air cavity velocity curve, as can be seen in figure 5.9. To achieve this comparison, the model was adjusted to simulate the laboratory testing conditions. While the magnitude of the average of all velocities of the 5640 to 8640 vectors of each test does not necessarily fully represent the flow characteristics, it does indicate a net increase in air velocity with the increase of temperature due to solar radiation. As such, as the solar radiation is reduced after the eighth hour of exposure, the maximum velocity measured during the test, 0.21059 m/s, is the maximum that can be achieved under the lab testing conditions. This is in good accordance with the 0.20 m/s calculated by both the model and the measured during the anemometer experiment.

5.7 Conclusion

This chapter has presented a large-scale experiment to determine the magnitude, direction and pattern of the flow within air cavities. The main objective of the chapter was to further verify the results of the model, which it does with relatively good accordance. This chapter has allowed for the characteristics and magnitude of the air flow to be known. This knowledge was required to proceed to the next step, i.e. the determination of the surface mass and heat coefficients. As such, chapter 6 focuses on further understanding of the role of the interior surface of the brick in the transfer of heat and moisture to the air of the cavity. As such, the link will be established between the brick and air flow. More specifically, the surface coefficients for a wind tunnel situation closely resembling the model will be evaluated.

Chapter 6: Surface Coefficients Experimental Determination

This chapter presents the surface coefficient evaluation by means of a wind tunnel. As the air flow conditions are now known, they can be used to determine experimentally the convective heat and mass transfer coefficients, in order to compare and update those used in the model. A wind tunnel setup was constructed specifically for this experiment. The objective is to measure the loss of mass of wetted brick samples over a given period of time at specified air velocities. Some basic theory on surface coefficient experiments is presented, followed by the experimental setup and procedure. The errors and limitations of the experiment are discussed, followed by the results of the experiment and analysis of those results.

6.1 General Overview

As air passes over saturated samples of brick, heat and moisture is transferred by convection. In the wind tunnel experiment, samples of brick are weighed continuously as air at a specified velocity will be passed over it. The loss of moisture mass from the brick yields the rate of mass flow, as the air takes on moisture. In this section, the governing equations and their application for the experiment are explained.

6.1.1 Governing Equations

This principle is governed by equation 6.1, is based on the equation for convective moisture transfer first discussed in Chapter 2.

$$G_y = h_m \cdot A \cdot (p_{v,surf} - p_{v,air}) \tag{6.1}$$

where G_y is the mass flux perpendicular to the material surface [kg/s], h_m is the convective mass transfer coefficient [s/m], A is the area of contact [m^2], $p_{v,surf}$ is the vapor pressure at the surface of the brick, assumed to be the saturation

vapor pressure [Pa], and $p_{v,air}$ is the vapor pressure of the air passing over the brick [Pa]. Once the mass transfer coefficient is known, the heat transfer coefficient may be determined by the Chilton-Colburn analogy first presented in Chapter 2, but repeated here.

$$h_m = \frac{\delta_a(T) h_{cv}}{k_a} \tag{6.2}$$

where δ_a is the vapor permeability of air as a function of temperature [1.87 x 10^{-10} s at 20°C], h_{cv} is the convective heat transfer coefficient [W/m^{2}K], and k_a is the thermal conductivity of the air [0.024 W/mK].

6.1.2 Application of Equation to Experiment

As the objective of the experiment is to determine the surface coefficients, the term h_m of the equation is the variable. As such, the mass flux is determined by the rate of mass loss from brick samples as the air passes over them in kilograms per second of testing. The air vapor pressure at the surface of the bricks is determined by the temperature of the brick surface. As we assume the air layer immediately above the brick to be saturated (100% relative humidity), the vapor pressure may be determined by:

$$p_{v,sat}(\theta) = 611 \cdot \exp\left(\frac{22.44\theta}{272.44+\theta}\right) \quad \text{if } \theta \leq 0°C \tag{6.3}$$

$$p_{v,sat}(\theta) = 611 \cdot \exp\left(\frac{17.08\theta}{234.19+\theta}\right) \quad \text{if } \theta > 0°C \tag{6.4}$$

In equations 6.3 and 6.4, θ is the temperature of the surface of the brick [°C]. Finally, the vapor pressure of the air passing over the brick is considered to be the average of the vapor pressure measured before and after the samples, at the inlet and the outlet of the wind tunnel. Since only the temperature and relative humidity will be measured at both locations, the partial vapor pressure may be obtained by the following:

$$p_v = p_{v,sat} \cdot \phi \tag{5.5}$$

where $p_{v,sat}$ may be obtained using the measured temperature and by equation 6.3 or 6.4 [Pa], and Φ is the measured relative humidity [%].

6.2 Experimental Setup

The wind tunnel used for the experimental setup was specifically designed for this experiment. The main section of the setup is constructed of plexiglass, which has the property of very low vapor permeability. This is essential as only the bricks must lose their mass of moisture without interference from the wind tunnel itself. Figure 6.1 shows the dimensions of the wind tunnel. The cross section of the tunnel 385 mm in width and 25 mm in height. The left section of the wind tunnel is called the tray portion, where bricks samples are placed. The right section is called the flow development portion, where the air flow is drawn into the tunnel with ambient conditions and where it becomes laminar. It was considered that bricks samples were not required throughout the flow development length as this would have minimal to no effect on the air flow development pattern.

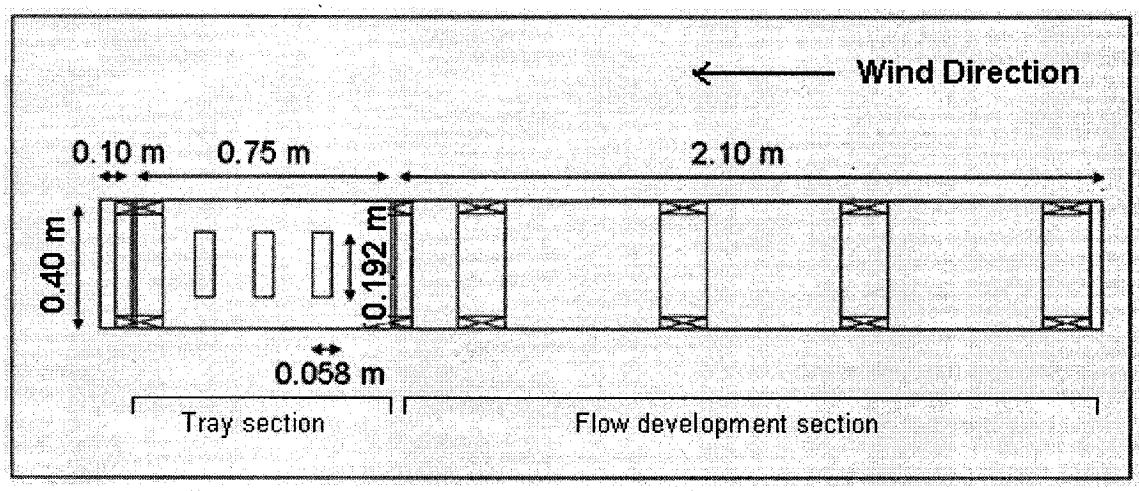

Figure 6.1: Base dimensions of the wind tunnel experimental setup.

Several measurement devices are included in the setup. Figure 6.2 shows a sketch of the complete setup of the experiment. For visibility purposes, the front ledge of the setup and the plexiglass top are not shown. Those pieces are crucial to maintain the seal in the tunnel and allow the air to pass through without losses or interruption. The tunnel is sealed on all sides by plexiglass, and care was taken to prevent leakage of air by well-designed joints. A fan contained within a rectangular box casing is placed above a flow redirection box, which is required to ensure that the flow spreads throughout the cavity as uniformly as possible. This will be described in more detail shortly. The fan acts in negative pressure, therefore air is pulled through the system from the flow development section, over the brick samples, through the fan and out the fan vents. As such, the inlet is considered to be on the flow development side of the brick samples, while the outlet is on the fan side of the samples.

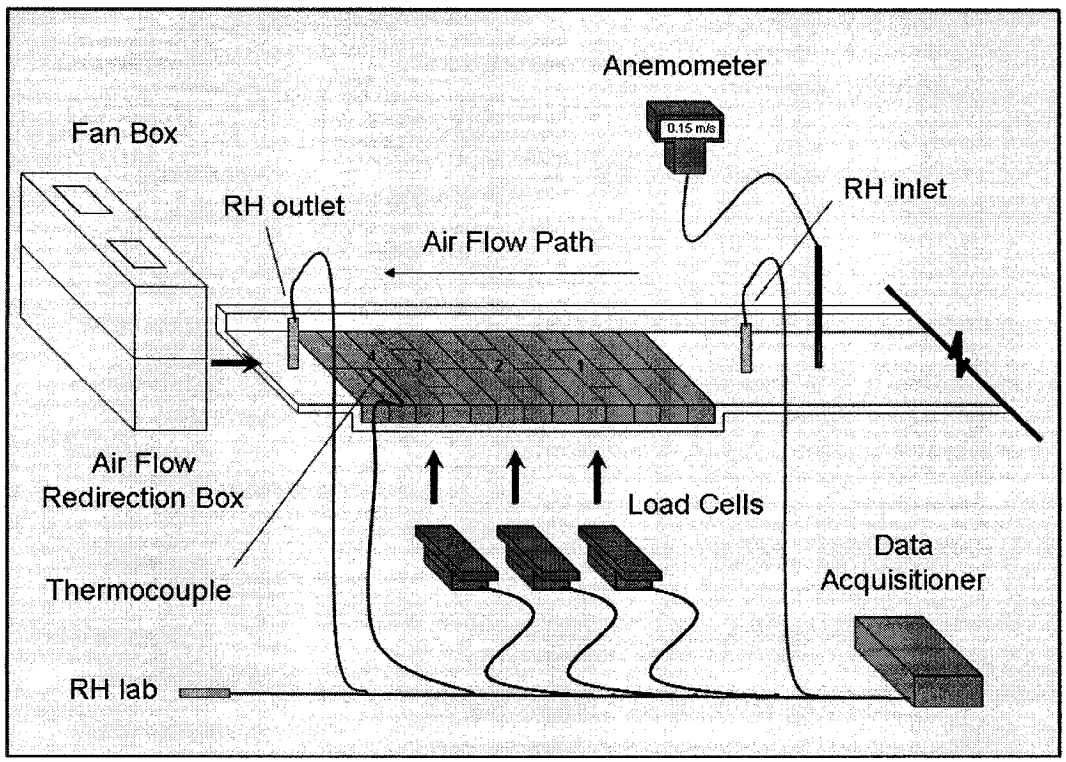

Figure 6.2: Schematic of wind tunnel experimental setup

Brick samples were cut from regular bricks to avoid the circular voids commonly found in bricks to prevent overflow of mortar during construction. These air voids would cause inconsistencies in results, and therefore were eliminated to allow only solid, uniform material to be evaluated. As can be seen, 26 samples were cut from 13 bricks (on either side of the voids) into samples of approximately 26 mm in height, 58 mm in width and 194 mm in length. Four (4) of these samples are used for the analysis; the remainder are placed in the lowered tray section of the tunnel permanently. Three (3) samples, numbered 1, 2 and 3 in order from inlet to outlet, are used for moisture mass loss measurements with load cells connected to a data acquisition system, while the remaining sample, number 4, is connected to a thermocouple so that the surface temperature of the bricks is known. The four measurement samples were coated on their four sides with paraffin wax to prevent movement of moisture in the transverse direction. These samples were measured precisely, and their characteristics are compiled in Table 6.1. The table includes their dimensions, volume, dry mass, and the amount of moisture required to be saturated to 99.93% RH (considered to be 105 kg of moisture per cubic meter of brick volume or 50% of capillary saturation).

Table 6.1

Characteristics of Brick Samples

Brick Number	Dimensions L x W x H [mm]	Volume [m^3]	Dry Mass [g]	Moisture Required [g]
1	196 x 58 x 26	2.956×10^{-4}	590.25	31.04
2	194 x 57 x 26	2.875×10^{-4}	597.07	30.19
3	192 x 58 x 26	2.895×10^{-4}	587.08	30.40
4	194 x 58 x 26	2.923×10^{-4}	581.20	30.72

The load cells used can be visualized in Figure 6.3, along with the lowered tray section of the wind tunnel. The load cells are of Scaime brand; model AG1, with a maximum capacity of 1.25 kg and an experimentally measured excitation rating of approximately ± 1.9×10^{-6} mV/V. The lowered tray section was constructed to allow the brick samples to be placed flush with the main plexiglass flow

development section. The three rectangular holes cut into the tray permit the weighing of the three samples by the load cells, which are placed under each specimen.

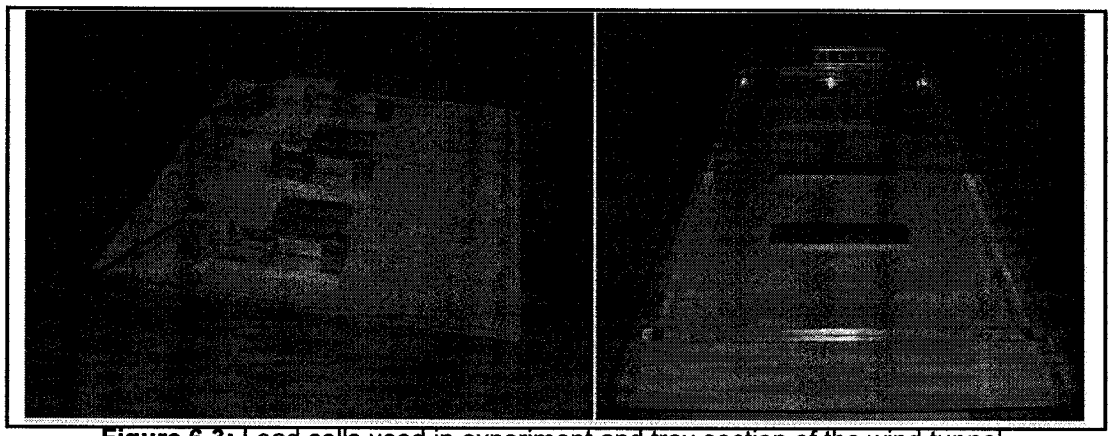

Figure 6.3: Load cells used in experiment and tray section of the wind tunnel.

The tray section of the wind tunnel was furnished with loose-fitted polyethylene sheets above each hole to prevent air leakage but to maintain the free movement of the measurement samples on top of the load cells. Figure 6.4 shows the hermetic covering of the three spaces, as well as the addition of the permanent brick samples which surround the 4 samples slated for measurements. The permanent brick samples were not wetted during the experiment; their purpose is to maintain the rugosity of the air space surrounding the four measurement samples.

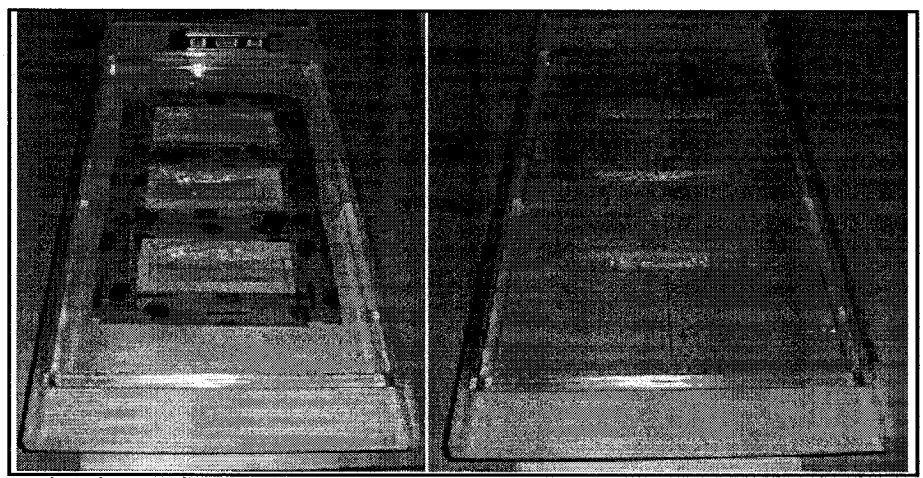

Figure 6.4: Loose-fitted polyethylene on sample holes and surrounding brick samples.

Aside from load cells and the thermocouple, the data acquisition system also receives readings from three relative humidity sensors, which provide the temperature and relative humidity of the air over time. RH sensors are placed at the inlet and outlet of the brick samples, while a third sensor is placed at another location in the laboratory to measure ambient conditions. Finally, an anemometer (same one used in the experimental work of Chapter 4), is placed before the inlet in the flow field to measure the air velocity at the center of the tunnel. The anemometer is not connected to the data acquisition system, but is always operating during experimentation to ensure that the air velocity is constant. A side view of the tray portion of the tunnel before and after the data measurement devices are connected as seen in figure 6.5.

Figure 6.5: Lowered tray portion of the wind tunnel before and after connection of the fan and data measurement devices

As can also be observed in figure 6.5, two small plugs are placed on either side of the anemometer on the far right-hand side. These plugs can be removed one by one with the anemometer placed inside them to evaluate the air velocity at all points along the transverse side of the air flow. It was observed by experimentation that the plugs to the immediate left and right of the center demonstrated air velocities very similar to those at the center. The velocity at the location of the plugs close to the side of the tunnel area showed a sharp drop off, however since the samples are located at the center of the flow field, it can be assumed that the flow field is uniform. The flow field is created by a fan that is encased in a steel rectangular box. The fan itself is composed of two spinning wheels with small vanes on either side of the motor. The wheels are located

below open vents where the air is blown out of the box. The suction air velocity is drawn through the bottom of the steel box, which is completely open but sealed to the air redirection box below it. The air velocity is modulated by means of a voltage regulation meter which is placed in series between the fan and the power outlet. The fan and regulation meter can be visualized in figure 6.6. The voltage supplied by the power outlet was found not stable, and as such the air velocity must be monitored and adjusted occasionally to ensure it remains within reasonable range.

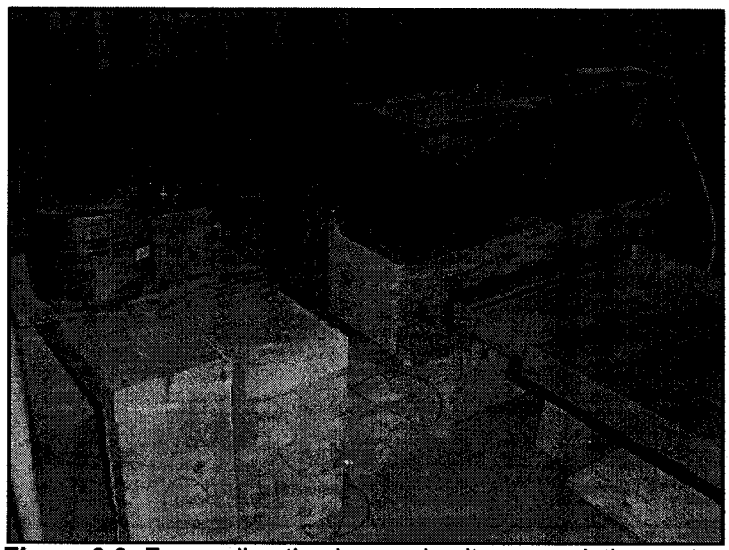

Figure 6.6: Fan, redirection box and voltage regulation meter.

The redirection box was built specifically to ensure the uniform flow field described previously. The box draws air through a slot that is cut exactly to the size of the cavity of the wind tunnel. The box abuts the wind tunnel with flexible foam weather stripping, which prevents the air from exfiltrating through the joint. The box is sealed to the fan on the top, however the air is only drawn in a 50 mm wide slot on the top side. The air is then redirected by means of a shelf placed between the two slots of the box. The interior of the box, as well as a view of the entire setup can be visualized in figure 6.7. In figure 6.7, a polyethylene covered frame can be seen at the inlet of the wind tunnel to prevent ambient air velocities from affecting those within the tunnel.

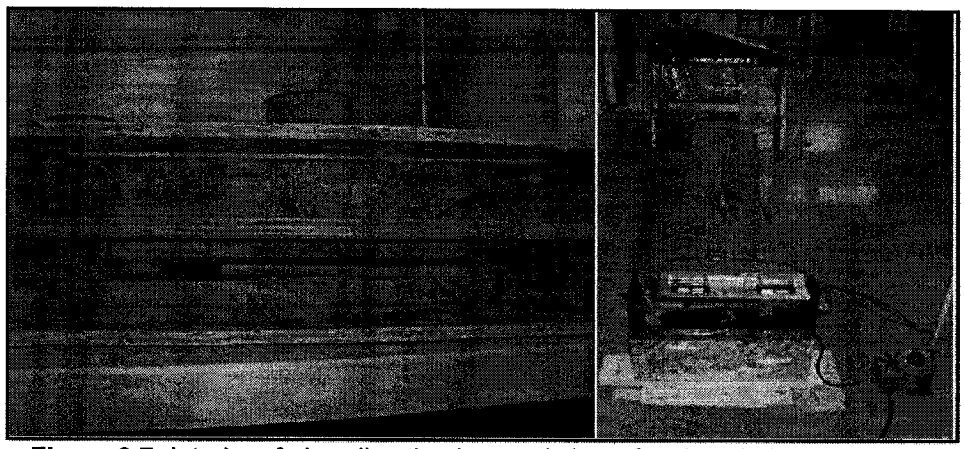

Figure 6.7: Interior of air redirection box and view of entire wind tunnel setup.

6.3 Experimental Procedure

The surface coefficients were determined for a variety of air velocities in the wind tunnel. For each test, only the velocity of air was altered, all other conditions were remained, as much as possible, identical. Previous experimentation had shown air cavity velocities in wall assemblies ranging from 0 to 0.25 m/s. Therefore, it was determined that five tests of three hours duration for air velocities of 0.05, 0.10, 0.15, 0.20 and 0.25 m/s were required. To help ensure accuracy and to offer a broader range of data, two additional tests were conducted. A second three-hour test at 0.20 m/s was conducted to verify repeatability of results. A third test at 0.20 m/s was conducted for a test duration of six hours. Finally, once the results were compiled, it was determined that a new set of data was required for reasons that will be outlined below. As such, four additional tests of one-hour duration were conducted at air velocities of 0.10, 0.20, 0.30 and 1.00 m/s. Thus, a total of 11 tests were conducted to determine the mass and heat transfer coefficients for air passing over the surface of wetted brick. In all cases, the data acquisition system took readings every 20 seconds. Also for all tests, as the air velocity varied due to the unstable voltage supply, an error range of ± 0.02 m/s was made necessary. However, it is reasonable to assume that the average velocity measured over the course of three hours would be the one specified for the test, as the air velocity would vary almost evenly above and below. Only when the air velocity reading would fall outside of the

error range would the test monitor manually adjust the voltage to return the value to the specified one. The experimental procedure for each test is described in the following:

- From the measurements, the volume of each sample is calculated, and the moisture mass required for saturation is determined based on 105 kg of moisture per m^3 of brick;
- The brick samples are weighed with a scale to determine their dry mass;
- Before all experiments, four brick samples are measured precisely, and coated on all four sides with paraffin wax to ensure moisture intake from only the top and bottom of the sample. A thermocouple is attached to the fourth brick sample;
- The wind tunnel is checked to be level.
- The access panel over the tray is removed to access the testing area;
- The four brick samples (three for mass determination, one attached to the thermocouple for surface temperature) are placed in a bath of water at room temperature. They are removed and the excess moisture on the top is wiped with a J cloth. They are then weighed on the scale every few seconds to ensure they attain their expected total mass for 50% saturation with an allowed variation of ± 0.5 g. This process generally takes about one minute per sample. The initial wet mass is noted for comparison with the load cells at the end of the test;
- The samples are placed in position in the tray with their flat uncut surface facing upwards to be in contact with the air flow;
- The data acquisition system is turned on and synchronized;
- The access panel is placed back and the fan system is tested. When the desired air velocity for the test is attained, the system is turned off with the settings retained;
- The four wet samples are placed in their respective positions on top of the load cells and in the area reserved for the thermocouple;
- The access panel is put back into position and the fan is turned on;

- The data acquisition system is launched;
- Readings are taken every 20 seconds for the one-, three- or six- hour duration;
- When the experiment is complete, the access panel and samples are removed;
- The brick samples are weighed so that their post-experimental mass may be known and compared to that noted by the load cells.

6.4 Errors and Limitations

Several sources of error and some limitations needed to be corrected or minimized to maintain the accuracy of the experiment. The four most pervasive are discussed here.

6.4.1 Exfiltration of Air

While every effort was made to avoid exfiltration of air from the wind tunnel during the design stage, it was inevitable that some losses would occur through the joints between the air redirection box and the tray section, as well as between the tray section and the flow development section. Exfiltration could also technically occur between the bottom of the tunnel and the access panel on the top. It is generally also recognized that exfiltration is of concern for experiments using negative pressure such as this one. Despite these minute losses, it is reasonable to assume the air velocity measured at the inlet of the tray section would be relatively stable along the wind tunnel.

6.4.2 Vibrations

Another potential source of error lies in the vibrations created by both the fan and the air movement over the bricks. As will be observed in the results section, the load cell readings of the mass of the samples are quite variant above and below the actual mass. This is especially true for sample number 3 which is closest to the fan and therefore it is reasonable to assume the fan's operation causes significant vibrations on the system. A phenomenon, known as back propagation

of air disturbance, may have caused small fits of turbulence in the region of the tunnel closest to the fan. This turbulence would accentuate vibrations. For all the samples, however, the air passing over the top of the bricks causes some variation, however, upon comparison, it appears that the lower the air velocity, the less effect of vibration on the measurements. Despite this error, adequate trend lines can still be established to observe the change in mass over the course of the experiment. Further, the initial and final masses of the brick have been accurately measured on a scale for comparison with the load cell readings.

6.4.3 Relative Humidity of the Air

A limitation of the experiment was that the air was not treated before it entered the wind tunnel. As such, the experiment was limited to air at the relative humidity of the laboratory. Since for the most part, the RH of the laboratory was measured to be in the vicinity of 50% (well below that of the surface of the brick, assumed to be at 100%), the experiment was able to run effectively. However, in any future experimentation, it would be of relevance to evaluate the effects of the RH of the air upon the surface coefficients.

6.4.4 Other Factors

Finally, other factors, such as the variation of voltage from the power supply as well as the ambient air velocity of the laboratory air can affect the air flow in the tunnel. It was attempted to minimize the former error by having a constant manual monitoring of the voltage variation meter to maintain the air velocity within the stated allowable error of ± 0.02 m/s. The latter error was minimized by providing a loose blocking of the air velocity of the laboratory with a polyethylene-covered frame. As such, it was attempted to maintain a relatively stagnant environment in the vicinity of the wind tunnel inlet. This proved to be most effective to maintain stability of the lowest air velocities in the tunnel.

6.5 Experimental Results

A sample of the data produced by the load cells is depicted in figure 6.8. The test results shown are for test 1, which measured the loss of moisture due to air passing at a velocity of 0.20 ± 0.02 m/s. It is coincidental that the mass of the three brick samples is lower for each successive sample. The samples were t cut in order for their mass to be approximately the same. The empirical values provided by the load cells are slightly higher than the total mass of the brick sample because a 50 mm thick piece of polystyrene was placed as a booster between the sample and the load cell to ensure the sample would sit flush with the surrounding bricks. It is more relevant to therefore simply observe the loss in moisture mass over the 3-hour, or 10 800 second, duration of the test. The top line represents Brick 1, which was closest to the inlet, followed by Bricks 2 and 3, in order to the outlet. Brick 4, closest to the outlet, was not measured by the load cells and was not directly in the flow field of the other 3 bricks, therefore it was used simply as a means of determining the surface temperature of the bricks when they were wet, as the thermocouple was placed right at the centre of the flow field.

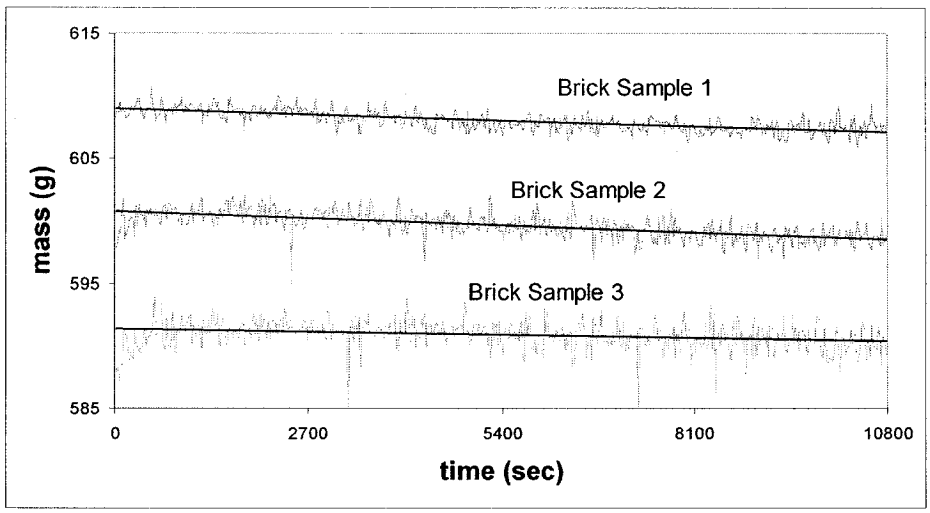

Figure 6.8: Measured loss of moisture mass by brick samples due to air velocity of 0.20 m/s.

It is relevant to note the variations caused by the vibrations of the air and fan, therefore trend lines were introduced to measure the overall losses. The full set

of experimental data with measurements and calculations of moisture mass, relative humidity, temperature and surface coefficients may be found in Appendix E. Since the mass of moisture loss was determined, and the vapor pressure of the air and surface of the brick are known, the mass transfer coefficients for the spectrum of air velocity from 0 to 0.25 m/s can be determined by equation 6.1. Table 6.2 depicts the expected error for the results at each stated air velocity, given that measurements were conducted with a stated allowable variation of ± 0.02 m/s. Figure 6.9 plots surface coefficients at the three locations in the tunnel from inlet to outlet for the five tested air velocities. Given that the five air velocity tests were conducted at approximately the same ambient air temperature and relative humidity conditions, figure 6.10 shows the difference in relative humidity observed from the inlet to the outlet of the brick sample tray. This demonstrates the relative proportion of humidity absorbed by the air after it has passed over the four wetted brick samples for each of the six air velocities tested. In figure 6.11, the results for the mass transfer coefficients of the four tests at velocities of 0.10, 0.20, 0.30 and 1.00 m/s for duration of one hour each are shown. The additional tests conducted at an air velocity of 0.20 ± 0.02 m/s were designed to verify the repeatability of the experiment, and the results may be seen in figure 6.12. Finally, it is relevant to observe the evolution of the mass transfer coefficients over the entire period of the tests. As a result, mass loss measurements at 30 minute intervals during the six-hour test were transferred into their equivalent mass transfer coefficients, and the profile of this evaluation may be observed in figure 6.13. Comparative model results for the mass transfer coefficients for a 10-day testing period may be seen in figure 6.14. In figure 6.15, the assumption of a 100% saturation of the surface of the brick is evaluated. Analysis of the figures is conducted in the next section. A brief discussion of the experimental error is in order. The mass measurements were taken to an accuracy of ±0.1 g, for an error of 0.03%. The relative humidity (and thus air vapor pressure) measurements were taken to an accuracy of ±3%, for an error of 8.57%. Finally, the sample measurements were taken to an accuracy of 0.05 mm, for total error of 0.37% for the three dimensions. The overall uncertainty of the experiment is

thus approximately 9%. The error bars are added to Figures 6.9 and 6.10. For clarity, errors bars are not added in the remaining graphs.

Table 6.2
Expected Error for Test Air Velocities

Air Velocity (m/s)	Expected Error
0.05	40%
0.10	20%
0.15	13%
0.20	10%
0.25	8.0%
0.30	6.7%
1.00	2.0%

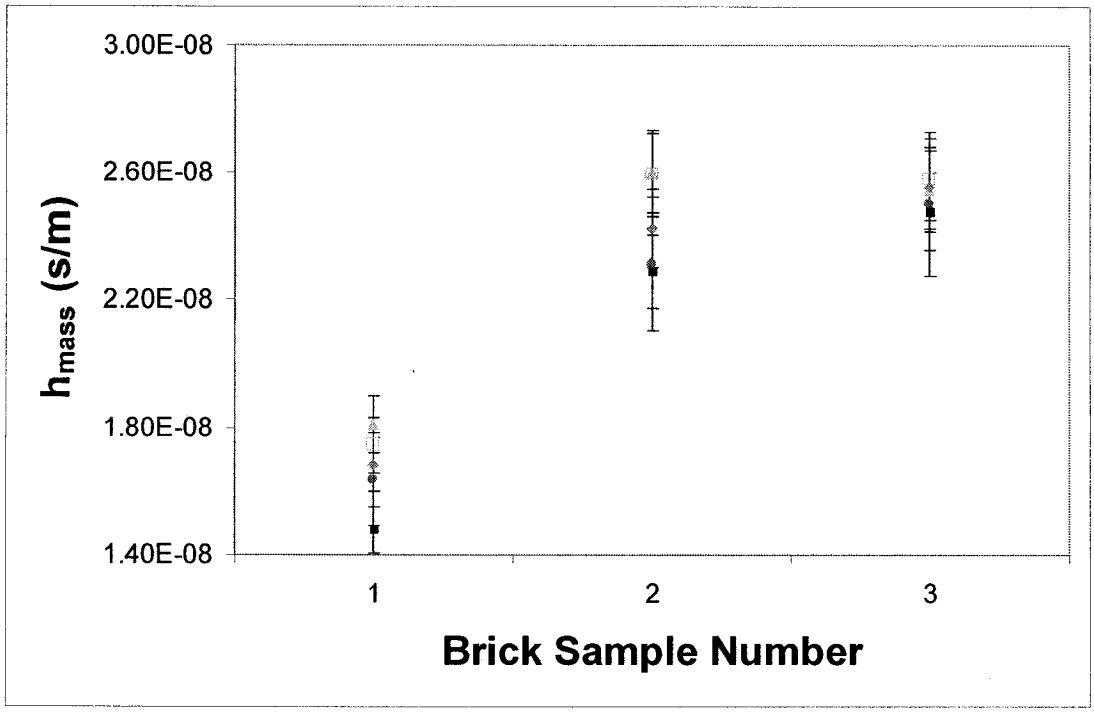

Figure 6.9: Mass transfer coefficients for tested air velocities (± 0.02 m/s) over the brick samples (3-hour tests) with error on h_{mass} determination.

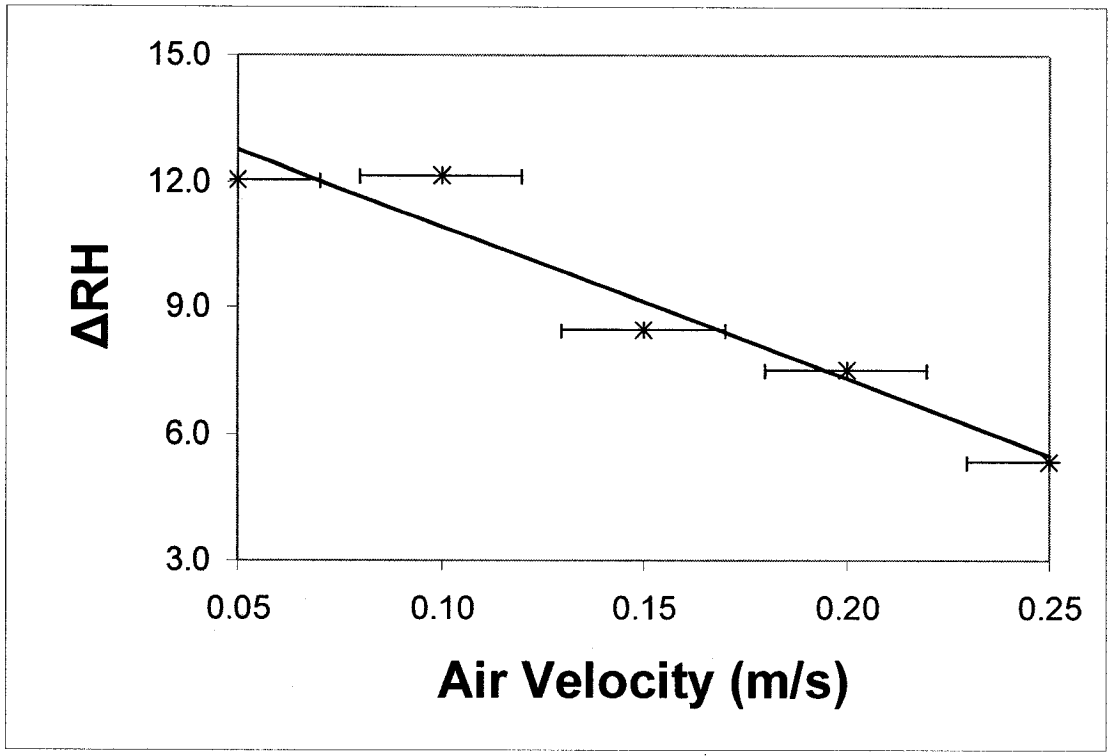

Figure 6.10: Relative humidity difference from the inlet to the outlet for tested air velocities (3-hour tests).

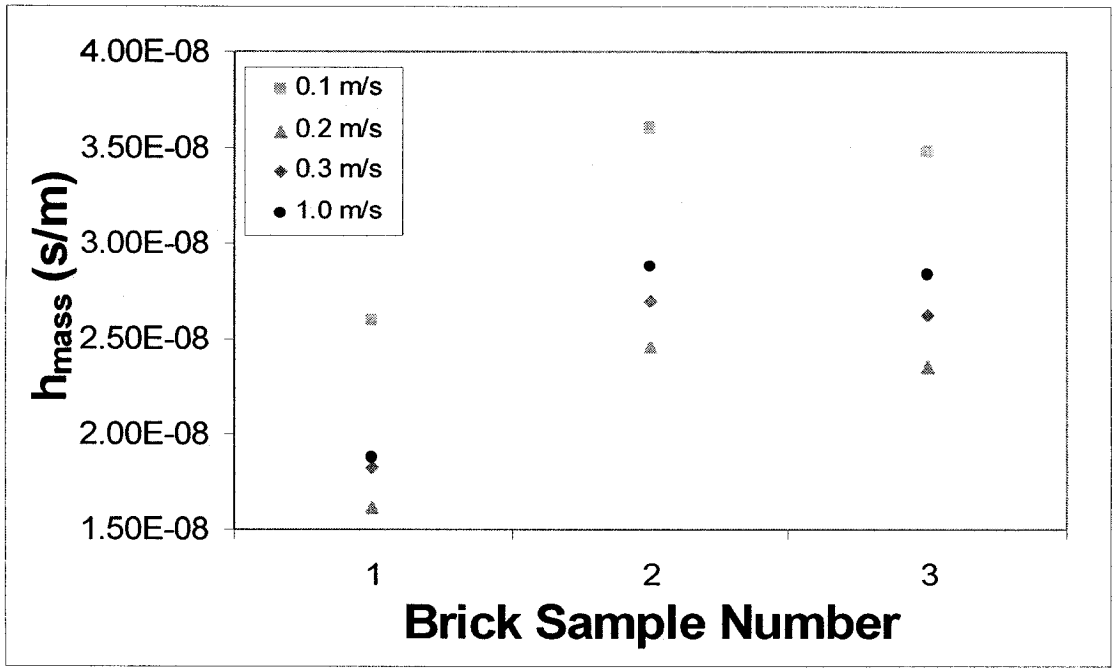

Figure 6.11: Relative humidity difference from the inlet to the outlet for tested air velocities (1-hour tests).

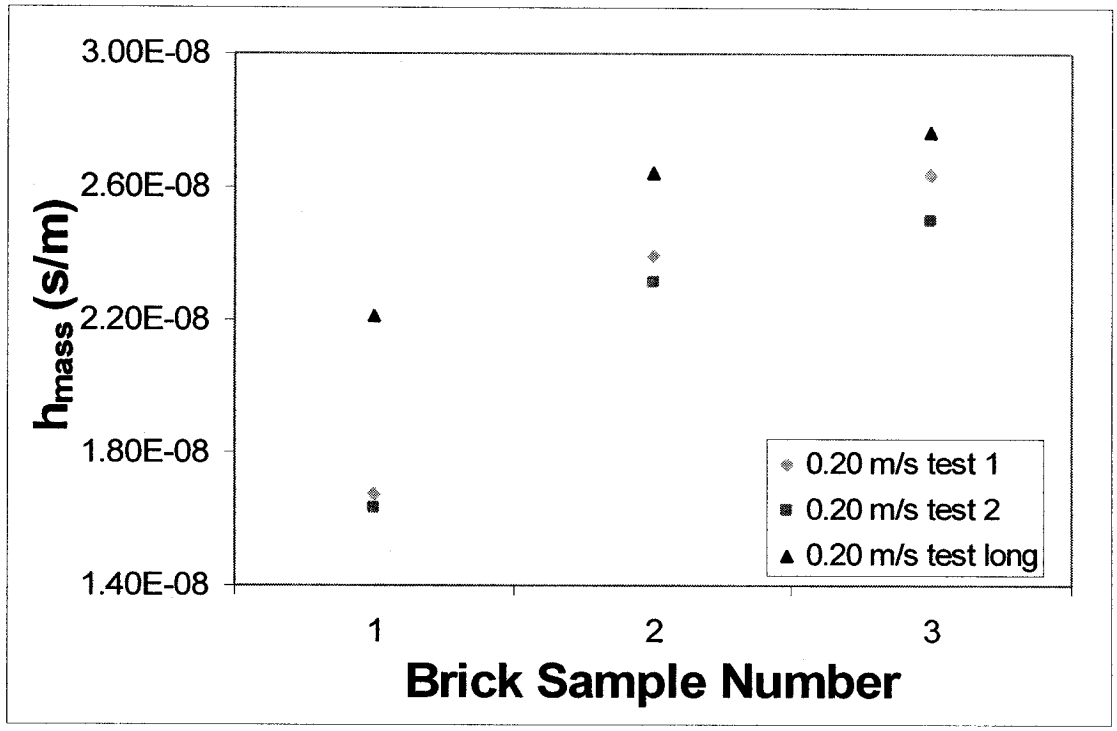

Figure 6.12: Mass transfer coefficients over brick samples for the repeatability test and the six-hour test.

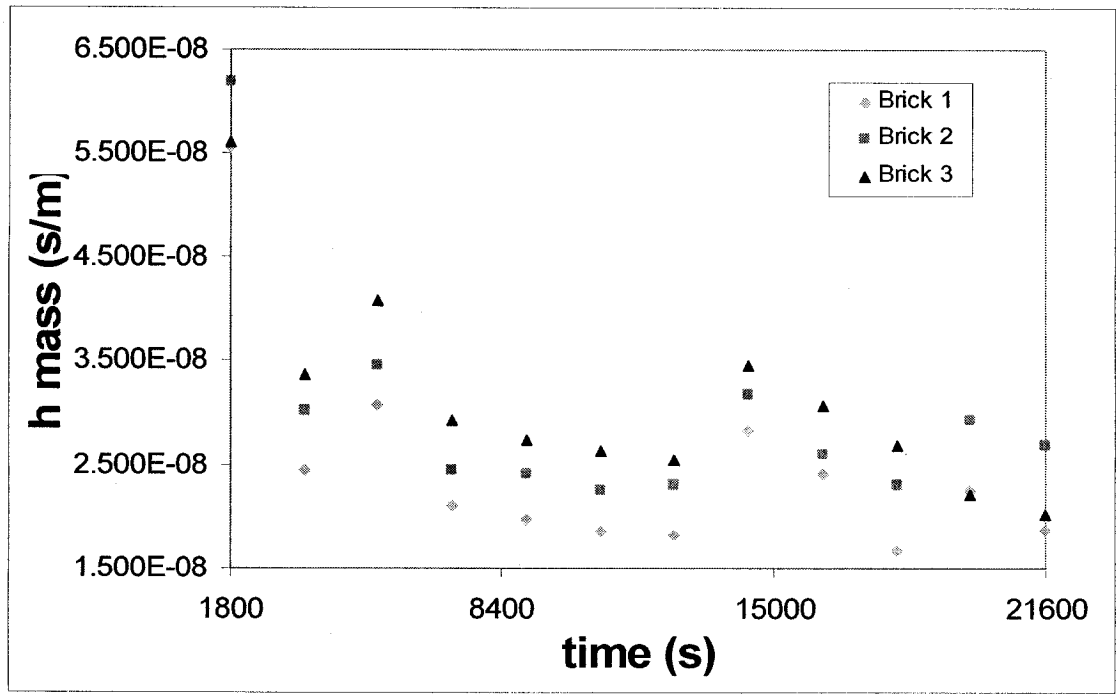

Figure 6.13: Mass transfer coefficients at 30 minute intervals for six-hour test at air velocity of 0.20 m/s.

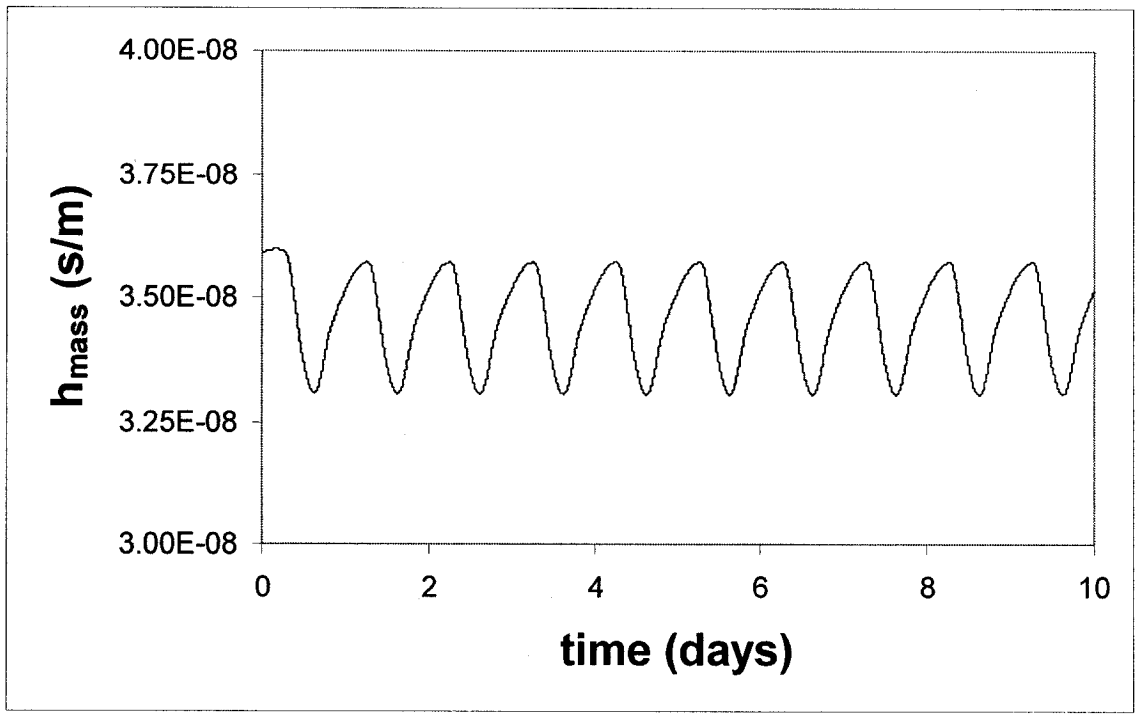

Figure 6.14: Profile of mass transfer coefficients considered by the model for a 10-day period at a typical interior brick wall surface node

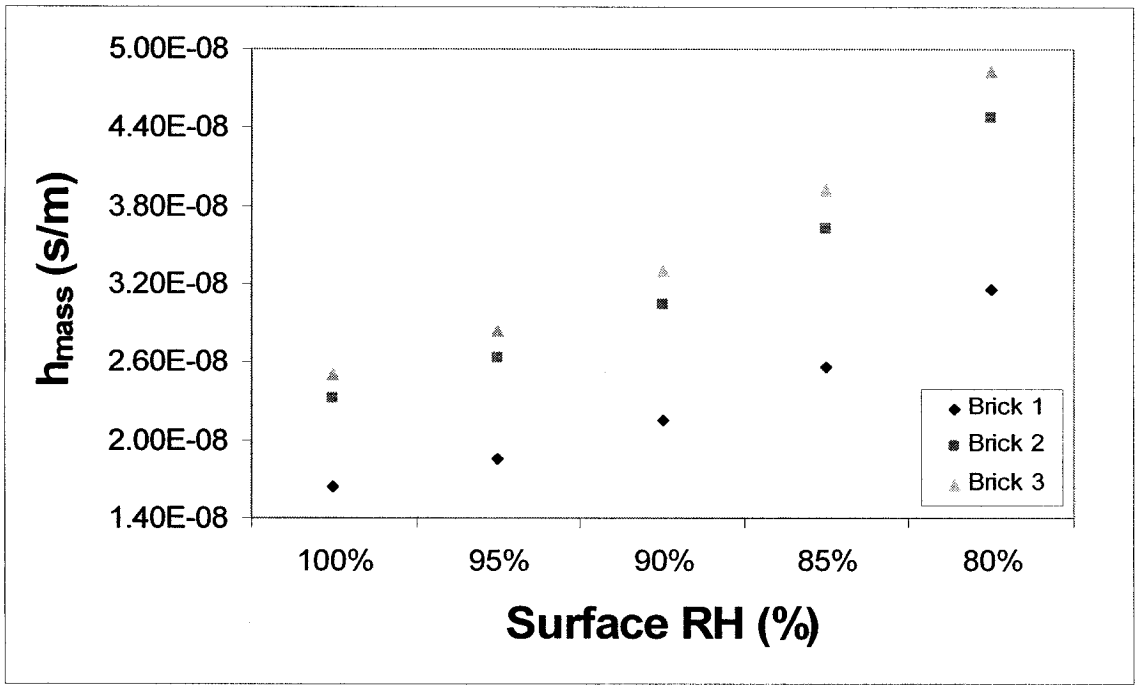

Figure 6.15: Evaluation of the effect of the assumption of 100% relative humidity of the surface of the brick for an air velocity of 0.20 m/s.

As proposed previously, the mass transfer coefficients may be correlated to the heat transfer coefficients for the development length of the air flow path. As such, the heat transfer coefficients were calculated and may be visualized in table 6.3.

Table 6.3

Convective Heat Transfer Coefficients (W/m^2K) for air velocities

Brick	0.05 m/s	0.10 m/s	0.15 m/s	0.20 m/s	0.25 m/s
1	2.52	2.61	2.43	2.36	2.13
2	3.75	3.76	3.50	3.34	3.31
3	3.72	3.67	3.69	3.61	3.58

6.6 Analysis of Results

The first conclusion that may be drawn from figure 6.9 is that the lower the moisture content of the air, the more moisture may be transferred, at least until a plateau is reached. The flow development suggests that there is a significant increase in the mass transfer coefficients at the beginning of the brick samples, but that there appears to be a slower increase over the subsequent samples. This is consistent with the figures provided by the model in Chapter 3, where the relative humidity is seen to increase in height as the air takes in the moisture from the brick. The most striking observation from figure 6.9 is that the experimental data suggests that, within limits for experimental error, the lower the air velocity passing over brick, the greater the mass transfer coefficient. This observance is corroborated by evaluation of figure 6.10. It would appear that for similar temperature and relative humidity conditions of the air entering the inlet, lower air velocities seem to cause the greatest increase in relative humidity from inlet to outlet. This would suggest that the moisture would require more time to be transferred to the air, and appears to be counter-intuitive to the notion that the more air passes through the cavity, the greater the amount of moisture may be evacuated. The main factor that may explain this finding is that, at lower air velocities, the buoyancy of the air is more significant. As well, the roughness of the brick causes turbulent flow at the surface of the brick. These two sources of

turbulence are more apparent when the air velocity is low. A mixed flow, no longer laminar, may explain the greater surface coefficient results for the vey low air velocities. Further, as was seen in Table 6.2, lower velocity of air causes less stable conditions and greater error. Also the duration of the test of 3 hours may also result in very different surface conditions during the test. Therefore, four additional tests were conducted at velocities of 0.10, 0.20, 0.30 and 1.00 m/s, with the testing time reduced to one hour. As can be seen in figure 6.11, aside from the lowest air velocity, the shorter time period reveals that, as the air velocity increases from 0.20 to 1.00 m/s, the greater the air velocity, the greater the mass transfer coefficients. This conclusion is more in line with expectations. The shorter tests may be considered to be more reliable in that the majority of the mass transfer occurs in the period immediately after the wetting, as can be seen in figure 6.13. The behavior at lower velocities may be explained by at least two factors. First, that buoyant force has a greater role to play at lower velocities, thus transferring more moisture to the air. Second, that lower air velocities are difficult to maintain experimentally, and due to that instability, the acceleration and deceleration of the air would have an effect on the mass transfer of moisture to the air.

Figure 6.12 demonstrates that there is repeatability of the results in principle for the experiment, as the two three-hour tests at an air velocity of 0.20 ± 0.02 m/s demonstrate good agreement between the mass transfer coefficient profiles. The six-hour test shows results slightly higher than those of the two three-hour tests. This could be the result of a small unforeseen increase in moisture transfer late in the experiment. This is confirmed by figure 6.13, which demonstrates a small increase in the mass transfer coefficient near the 14 000 second-mark. This could be due to an acceleration of the air velocity of about 0.02 m/s during that period, causing the increase in mass transfer. Overall, figure 6.13 demonstrates that there is a large initial drop in the mass transfer coefficients over the time of the experiment, but that this drop is mitigated by a

less steep slope that will continue to decrease presumably until there may be no more moisture uptake from the bricks to be evacuated by the air.

The mass transfer coefficient values do not exactly reflect those used in the model, as the model does not take into account the flow development over the length of the 2.4 or 3 meter heights of the wall. The magnitude of the average mass transfer coefficients ranges from 3.3×10^{-8} to 3.6×10^{-8} s/m over the course of a 10-day testing period, as can be seen in figure 6.14. These values are almost a direct function of the temperature of the air in the cavity. As a result, the values taken for the wind tunnel experiment could not be used for comparative analysis, because the air temperature is maintained approximately constant throughout the eight tests. The general magnitude of the values used in the model are slightly above the range determined in the experiment.

The heat transfer coefficients in table 6.2 demonstrate the same trend as the mass transfer coefficients of figure 6.9 as they are a direct function of one another as reflected in the Chilton-Colburn correlation (Chilton and Colburn, 1934). This is interesting in that it is not generally regarded that heat transfer is a function of the development of the air over the development length. Rather, an average is usually taken for an entire surface at given conditions. In the case of the model, the average taken is 4 W/m^2K, which is within the magnitude of the results displayed in the table. This value is taken due to the low velocities prevailing in the cavity, thus resulting in low Reynolds Numbers and very low heat transfer. As the air reaches the development plateau after a very short length, the majority of the values of heat transfer measured experimentally occur in a range just below 4 W/m^2K, thus the heat transfer coefficients in the model are in good agreement.

As can be seen in figure 6.15, the assumption of 100% relative humidity on the surface of the brick was an acceptable assumption, but can be the cause of errors and a better means of assessing surface conditions should be devised in

the future. A decrease of just 20% can cause an increase in the mass transfer coefficients of a factor of 2. Since the same assumption is used for all the tests, they are comparable to one another. However, this boundary condition should be evaluated more closely in future testing to obtain accurate empirical values.

A final note should be made to further understand the results of the surface coefficient experiment. The development section of the setup was designed to allow the air flow to become fully developed and laminar. However, once the air reaches the tray section, the roughness of the bricks may have caused a readjustment of the air velocity profile with a possible presence of turbulence. As such, the exact type of flow in that section cannot be assumed until it is further studied using PIV.

6.7 Conclusion

The effect of air velocity on surface coefficients has been examined and better understood in this chapter. In general, it appears as though the rate of transfer of moisture from bricks to air is heavily influenced by the location of the brick along the development length, the development length itself, the time elapsed after saturation, and of course the air velocity. In chapter 7, a synthesis of the knowledge obtained in chapters 4, 5 and 6 will be made by means of parametric analyses to determine how the variation of certain parameters of the model's base case can influence the profiles of temperature, relative humidity and air velocity in the cavity.

Chapter 7: Parametric Analysis

This chapter presents the results of model simulations conducted to observe the response of the model to variations of its basic parameters. In the base case of the model, many assumptions were made to obtain the results that were subsequently validated. However, it is relevant to determine how even slight variations of these parameters affect the final model results. The parameters chosen to observe are:

- the thickness of the cavity,
- the emissivity of the backwall,
- the initial relative humidity in the brick,
- the intensity of the solar radiation incident on the wall,
- the size of the weephole vents and
- the addition of wind pressure.

Figures containing summaries of the simulations are presented, analysis of the figures are performed and conclusions are drawn. In all figures of simulations, the base case is denoted by a black line, while the variations are drawn in shades of gray or with dashed lines. In most cases, the impact of the given parameter is shown on the air velocity and temperature of the cavity. Due to the length of computation, the relative humidity profile is presented for only the three most relevant cases of the six. However, as will be shown, this is sufficient to draw pertinent conclusions.

7.1 Cavity Thickness

The first parameter to be observed is the thickness of the cavity. In the base case of the model, the cavity thickness is taken to be 25 mm. A larger or smaller cavity could affect the flow of the air due to restriction or relative unrestriction of the upward air flow. As such, a smaller cavity thickness, 15 mm, and two larger cavity thicknesses, 35 mm and 50 mm, are observed. The effect of varying the cavity thickness is first determined on the velocity of the air in the cavity in figure

7.1. It is then measured for the temperature of the air in the cavity in figure 7.2. The parametric analysis is conducted over a testing period of five (5) days, with the results shown for the mid-point of the cavity, i.e. at a height of 1.50 meters. In the simulations, the first day's results tend to be slightly lower than the results of the following days. This is a result of the residual heat of solar radiation from the previous day not being applied as an initial boundary condition at the start. Once it is taken into consideration, the results repeat normally for every subsequent day of simulation.

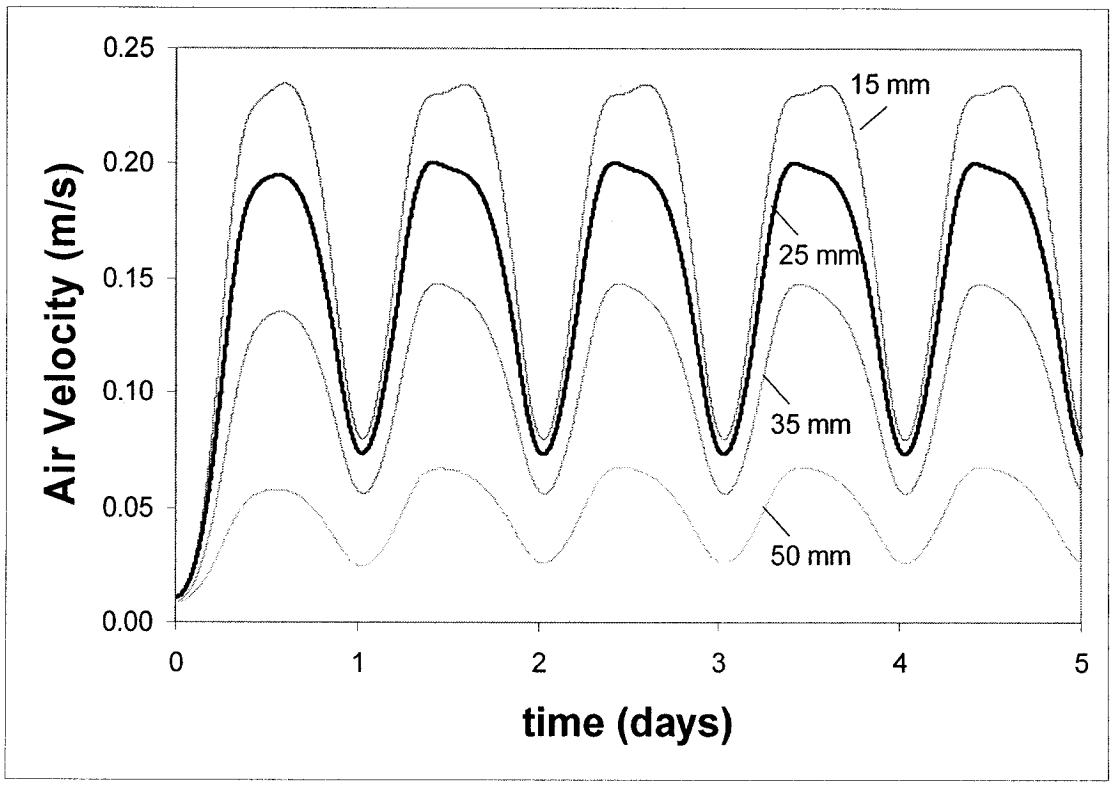

Figure 7.1: Cavity air velocity at height 1.50 m for varying cavity thicknesses.

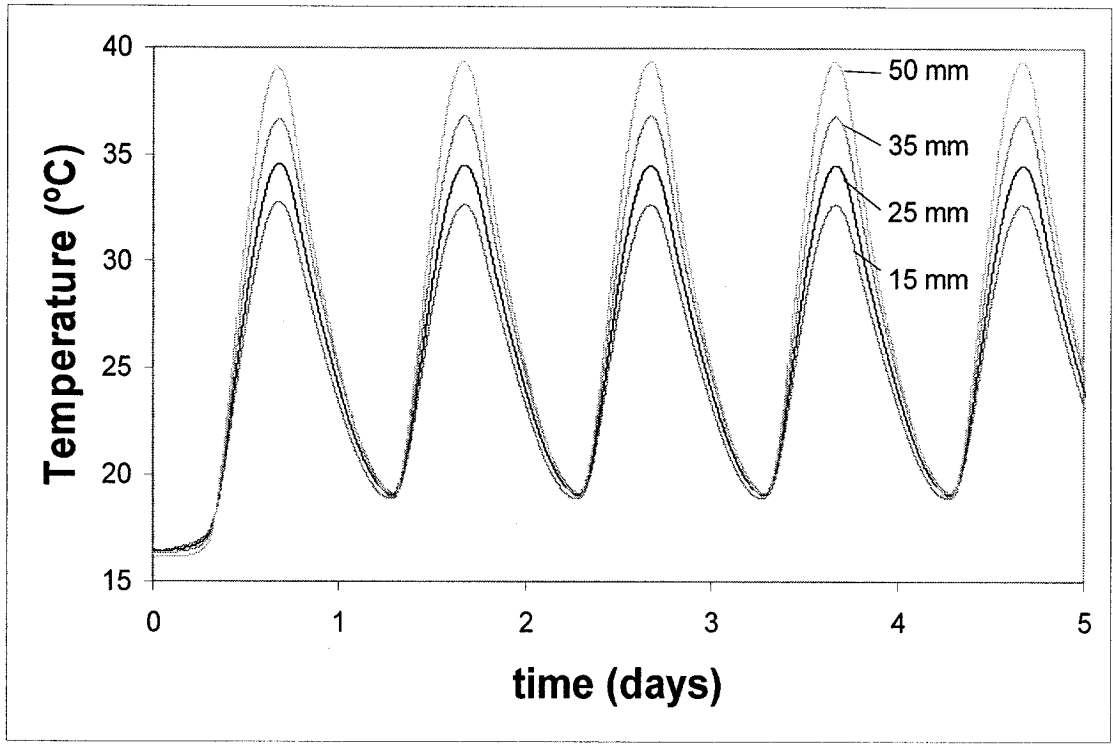

Figure 7.2: Cavity air temperature at height 1.50 m for varying cavity thicknesses.

As can be seen in figure 7.1, the modeled results suggest that, under identical conditions, the greater the cavity thickness, the lower the air velocity. This would appear logical in that when the same mass of air is forced through a smaller opening, its velocity must increase to maintain conservation of mass, and vice-versa for larger openings. Analytically, this finding also holds. When the hydraulic diameter term d_H of equation 2.16 is increased, the resulting pressure difference is decreased, which in turn decreases the cavity velocity by equation 2.14. The magnitude of the increase or decrease is of interest in that, for example, doubling the thickness of the cavity from 25 to 50 mm will result in an approximately threefold decrease in peak air velocity, from 20 m/s to 6.5 m/s. The relationships for the other two cases (15 mm and 35 mm) are similar. In figure 7.2, the natural extension of the previous phenomena is observed as a larger cavity thickness will result in a greater air temperature in the cavity. This would suggest that with a lower air velocity in the cavity, less heat may be evacuated and therefore the air temperature may rise. The magnitude of the rise of the peak cavity temperature between a cavity of thickness 15 mm and that of

thickness 50 mm is approximately 6°C for the given conditions, which is considerable but not overly significant. It would also seem unlikely that cavities greater than 50 mm would be considered in construction due to increased costs. It would appear, therefore, that increasing the thickness of the cavity provides an excellent means of reducing the air velocity within the cavity without overly affecting the air temperature. This, however, is in contrast with the CFD findings of Stovall and Karaziogis (2005), who found no such increase within that range of cavity thicknesses. This parameter should therefore be further analyzed.

7.2 Emissivity of the Backwall

The second parameter observed is the emissivity value of the backwall. Only on the backwall side of the cavity, i.e. the fiberboard surface, is the emissivity increased, as it would be unfeasible to manufacture brick with greater emissivity. Surface emissivity, as observed previously, governs the heat transferred by radiation exchange between the two parallel walls of the cavity. While it would appear impractical or expensive to produce brick with lower emissivity, the emissivity of the backwall could easily be altered via choice of material or even by paint. The emissivity of both the brick and the backwall in the base case is taken to be 0.9. For the parametric analysis, two other emissivities are observed, one close, at 0.8, and one much lower, at 0.3, to the base case. The effects on cavity air velocity (figure 7.3) and temperature (figure 7.4) are demonstrated.

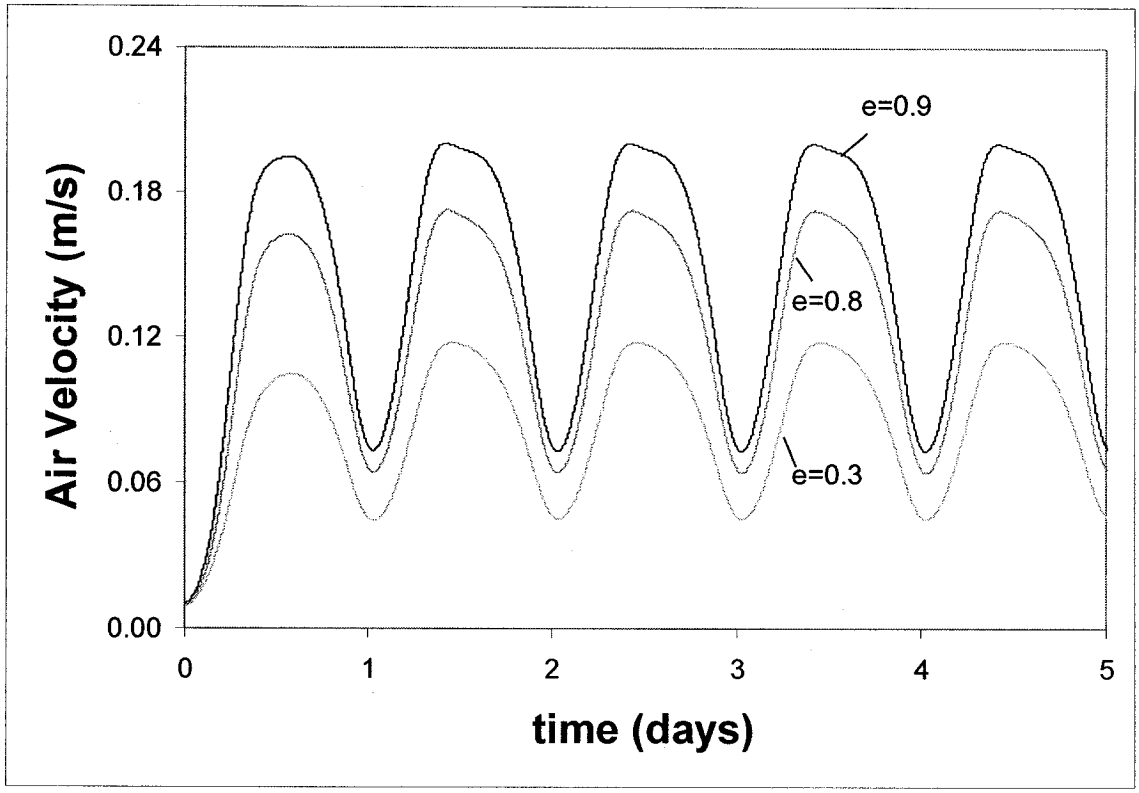

Figure 7.3: Cavity air velocity at height 1.50 m for varying backwall emissivity.

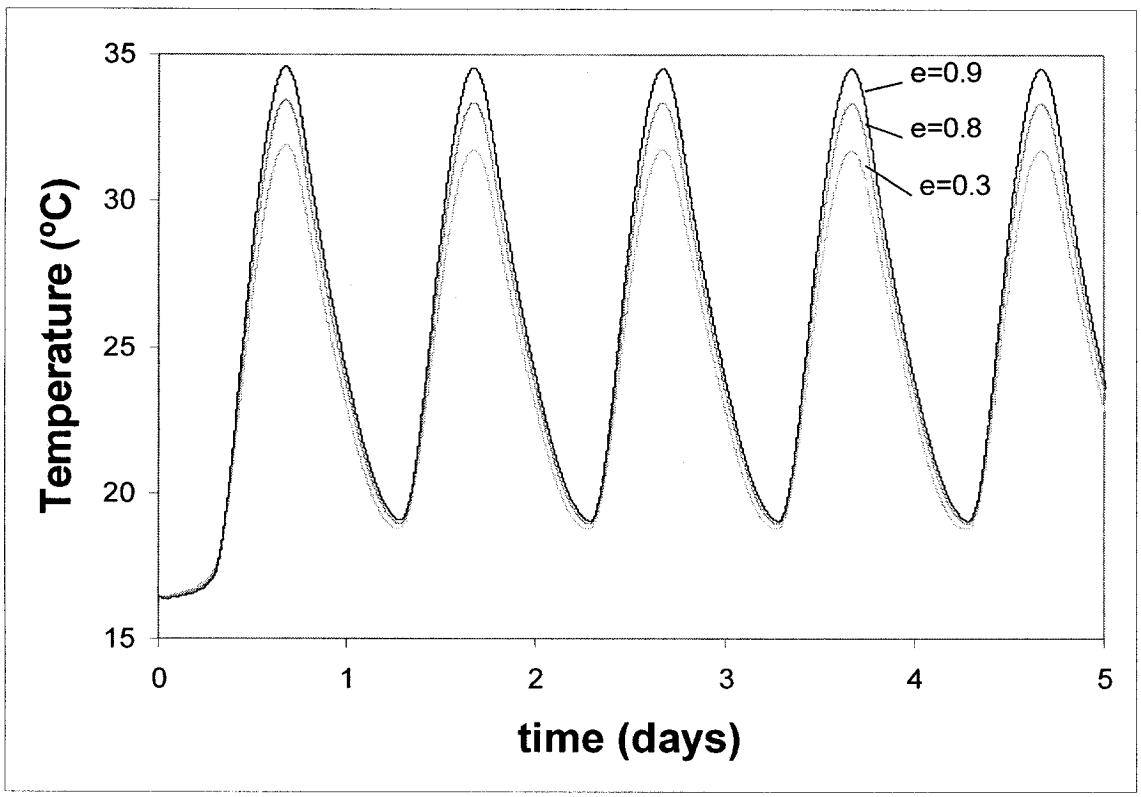

Figure 7.4: Cavity air temperature at height 1.50 m for varying backwall emissivity.

In figure 7.3, it would appear that the lower the emissivity of the backwall, the lower the air velocity in the cavity. This could indicate an opposite reaction between air temperature and velocity to what was observed in the previous section for cavity thickness. In that case, an increased cavity thickness seemed to decrease the air velocity, which, in turn, caused an increase in temperature. However, in this case, the lower emissivity results in less radiation exchange between the two surfaces, thus lowering their temperatures. As the air flow is driven by temperature gradient, the lower brick wall temperature causes a lower air velocity. Figure 7.4 confirms this assertion, as the lower emissivity does cause a lower air temperature within the cavity. Within that context, however, a decrease of the emissivity of the backwall by two-thirds, from 0.9 to 0.3, appears to cause a peak cavity temperature decrease of only approximately 2°C. Therefore, it would seem that decreasing the emissivity of the backwall will also have the effect of decreasing cavity air velocity without a proportional nor significant change in the air temperature behavior.

7.3 Initial Relative Humidity in the Brick

The brick wall is assumed to be saturated by rain water to a relative humidity throughout of 99.93% in the base case. For this to occur, however, a significant, uniform and somewhat prolonged driving rain would have to wet the cladding. It is therefore relevant to study the effects of a lesser, yet still high, relative humidity in the brick as the initial condition for the model. A relative humidity of 95%, 90% and 85% is considered. The effects of reducing the initial relative humidity in the wall, while maintaining all other conditions, is observed versus the number of days required for drying of the wall. The model simulation in each case is conducted for a testing period of 15 days, with the results shown in figure 7.5. While not shown, the cavity air velocity is not affected by the change of this parameter. The results shown are for the central brick node, at the centre of the 90 mm brick cladding thickness and at a height of 1.50 meters.

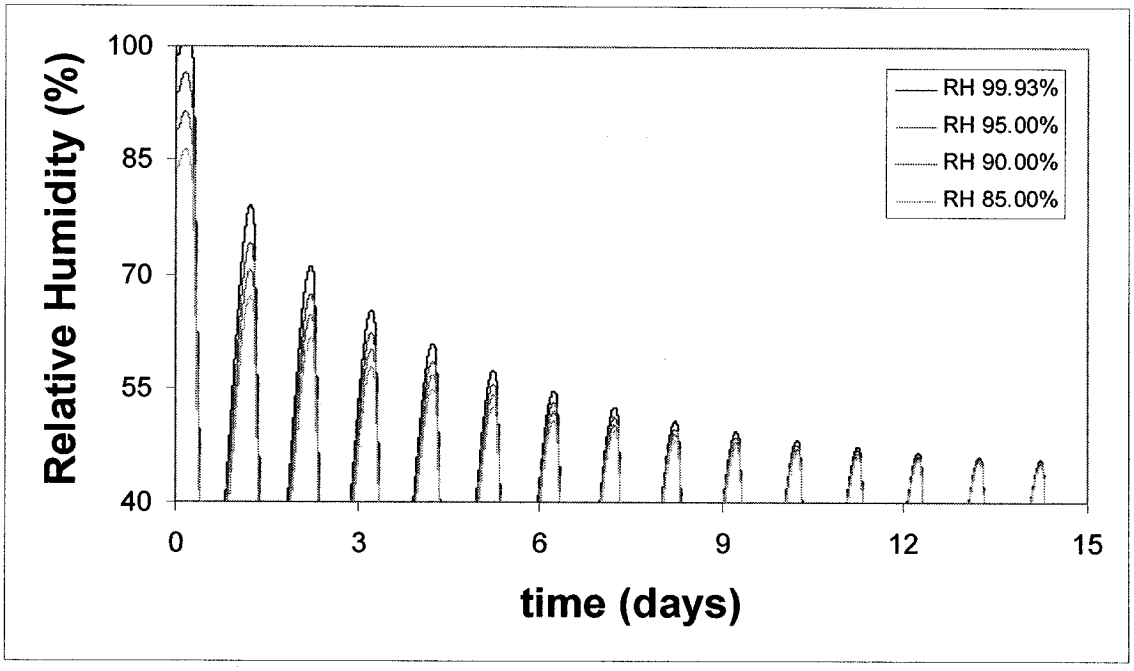

Figure 7.5: Relative humidity of central brick node for varying initial relative humidity.

As can be observed in figure 7.5, the initial drying rate is lower as lower starting RH. From about 45% , the RH in the brick is almost the same in all cases. As for the time required to reach stability, there appears to be about a 3-day difference between the simulation with 85% (by the 10^{th} day) and that of 99.93% (the 13^{th} day). More studies, in terms of moisture content and phase of moisture of the brick versus time are required before making conclusions for the effect of this parameter. Also, further comparison with literature is premature.

7.4 Solar Radiation Intensity

As the buoyancy of the air is highly dependent on the temperature gradient of the brick cladding, any factors driving the gradient should therefore greatly affect both the temperature and velocity of the air in the cavity. While the variation of the outdoor temperature will have a predictably proportional effect on the air cavity temperature, the variation of the intensity of solar radiation incident on the cladding could cause more pronounced results. In the base case, a solar

radiation intensity profile in the form of a sine wave peaking at noon on a testing day is used. The peak intensity is taken to be 1000 W/m^2, with values of 0 W/m^2 assumed for overnight when the sine wave would fall below zero. It is deemed relevant to observe the effects of increasing the peak solar radiation by 20% and 40% to represent more extreme conditions or climates. It should be noted, however, that the outdoor temperature profile was maintained the same with a maximum of 26°C during the afternoon and a minimum of 15°C at night in all cases. Figure 7.6 demonstrates the effect of the increased solar radiation on the temperature of the outside surface of the brick. Figure 7.7 shows the same for the air temperature in the cavity. Figure 7.8 presents the effect on the velocity of the air in the cavity. Finally, figure 7.9 demonstrates the ventilation drying of the central brick volume of the cladding over a 15-day testing period. As usual in this thesis, the values are taken for the mid-point of the height of the computational domain, 1.50 meters.

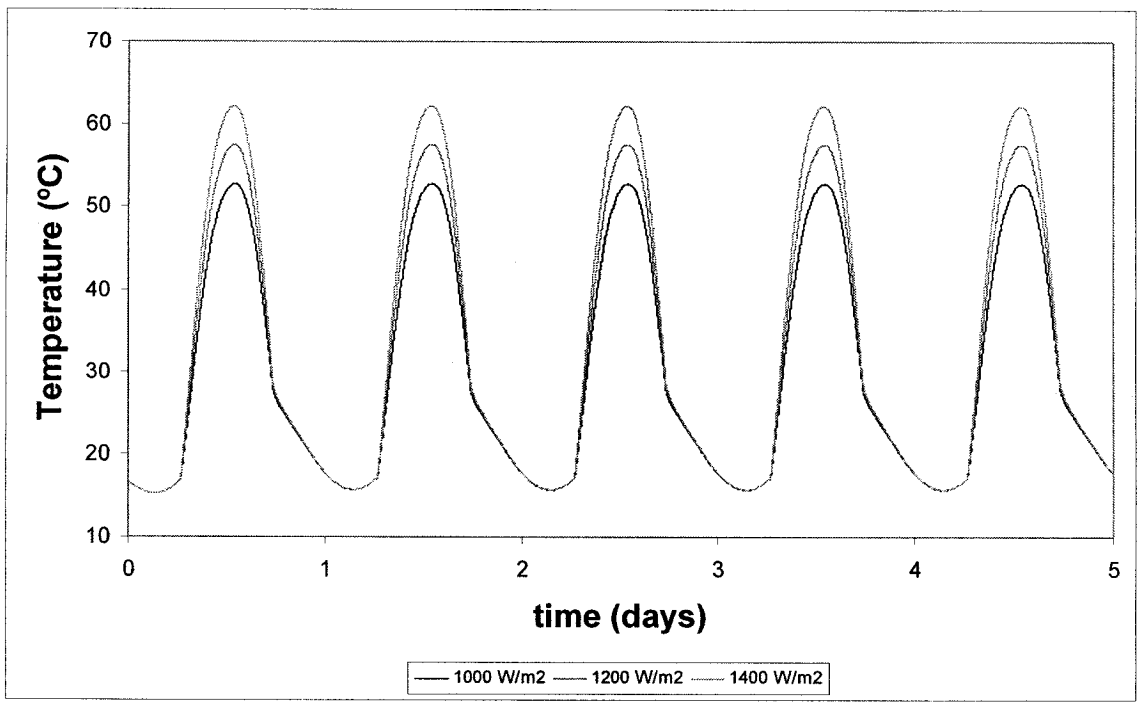

Figure 7.6: Outside brick surface temperature at 1.5 m for varying peak solar radiation intensity.

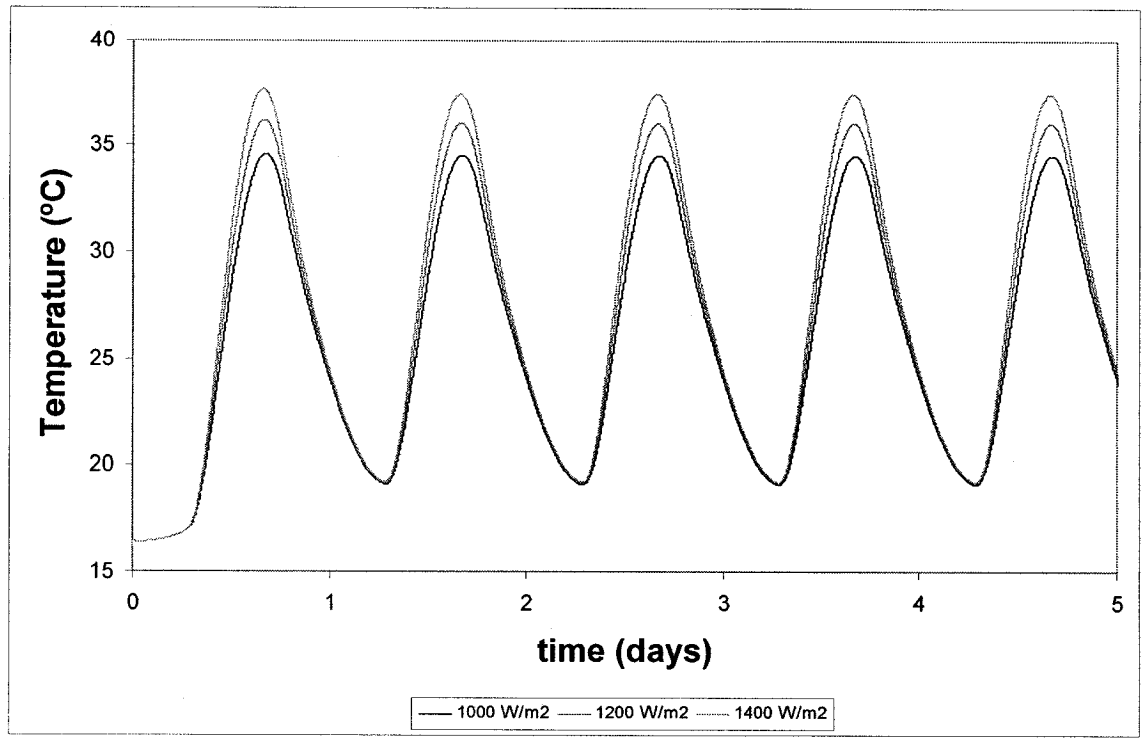

Figure 7.7: Cavity air temperature at height 1.5 m for varying peak solar radiation intensity.

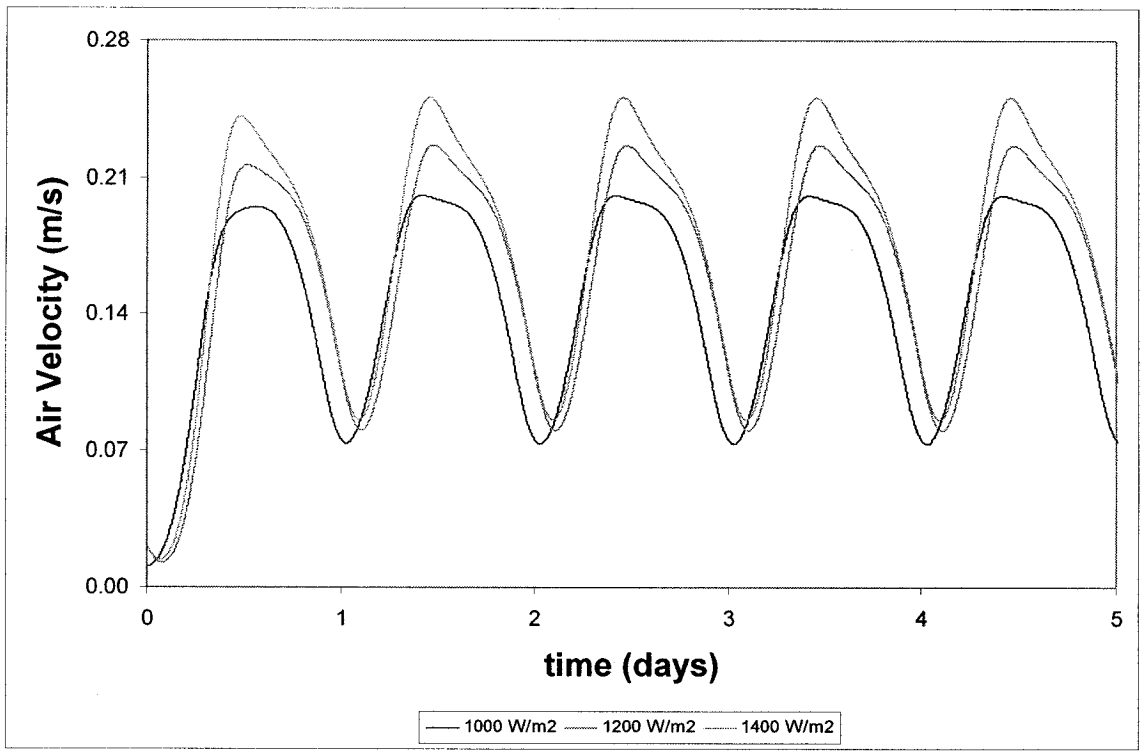

Figure 7.8: Cavity air velocity for varying peak solar radiation intensity.

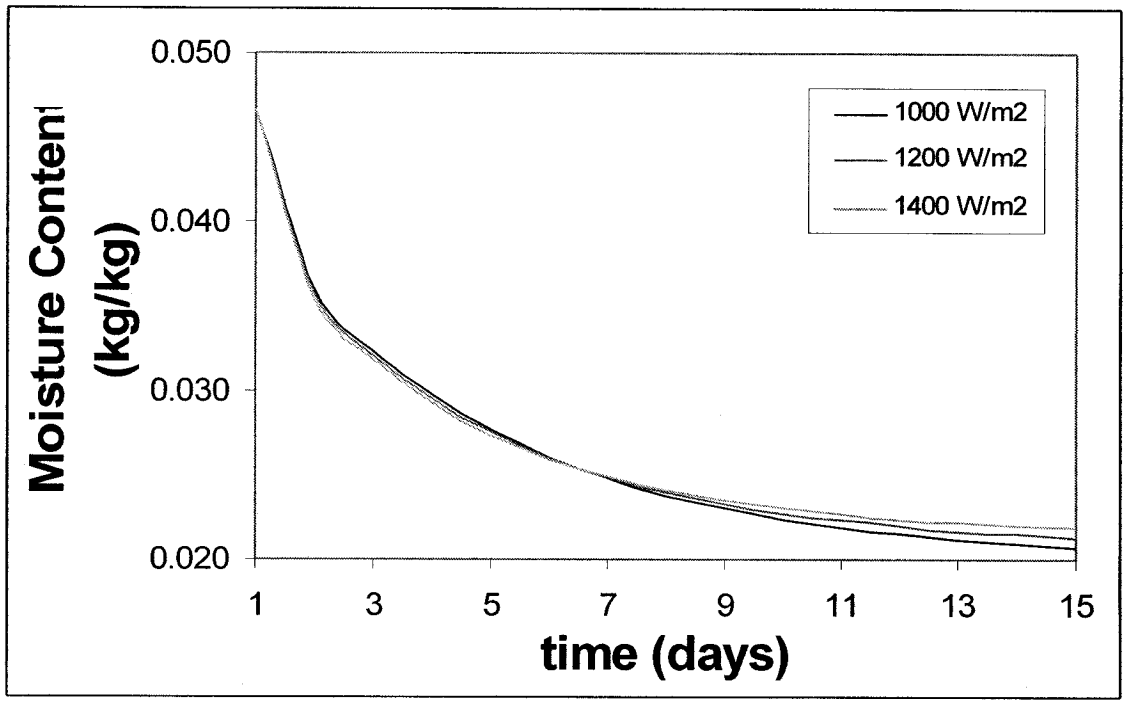

Figure 7.9: Moisture Content profile for 15-day testing period at central brick node for varying solar radiation intensity

From figure 7.6, the effect of the increased solar radiation on the outside brick surface is a rise of its peak temperature by over 10°C from the base case of the peak of 1000 W/m^2 to the 40% increase case of 1400 W/m^2. This is in accordance with the findings of Straube and Burnett (1998), who found increases in surface temperature due to solar radiation to be within 10°C and 30°C. Of course, due to the thermal storage of the brick, the increase of the peak temperature air in the cavity is mitigated to about 4°C between the two cases, as shown in figure 7.7. The cavity air velocity is greatly affected by this temperature increase, moving from the peak of 0.20 m/s in the base case to about 0.25 m/s in the extreme case, as demonstrated in figure 7.8. This is due to two factors: the increase in driving pressure due to the heating of the outside of the cladding, and the heating of the air itself in contact with the warm brick on the inside of the cladding. As such, an increase of the intensity of solar radiation has a marked effect on the air temperature in the cavity and a substantial effect on the velocity of the air. Figure 7.9 shows an interesting trend: the larger the solar radiation intensity, the less time required for drying of the brick. This is logical in that the

extra heat will definitively dry out the brick wall at a quicker pace. It is also of note that the higher wall temperature in this case will therefore require less moisture to be driven out to attain a stable moisture condition.

7.5 Weephole Size

As discussed in the literature review, studies have shown weephole size to significantly alter the velocity of the air in the cavity. As such, it is of relevance to observe this effect with model simulations. To simplify the methodology, only the weephole height is changed, the width is maintained at 10 mm for all tests. The base case makes use of a weephole height of 55 mm, therefore, one smaller (25 mm) and two larger (85 mm, 125 mm) weephole heights are simulated. The results may be visualized in figure 7.10. The velocities are measured for the central cavity node at 1.50 meters in height, however, this should be indicative of the overall cavity air velocity as it should remain about the same due to conservation of mass.

Figure 7.10 demonstrates that the smaller the weephole size, the greater the air velocity in the cavity. This could be due to the fact that air is drawn into the cavity within a more restrained area. The same mass flow in a more restrained area results in a greater air velocity by the law of conservation of mass. The effect shown here is similar to that determined for the cavity thickness, but it less pronounced because the upper and lower weepholes represent only a very small fraction of the overall path of the air through the wall assembly. Nevertheless, increasing the weephole height by a factor of 5, from 25 mm to 125 mm (keeping in mind the width of 10 mm), the velocity of the air decreases from approximately 0.21 m/s to 0.16 m/s for the given conditions, or almost 25%.

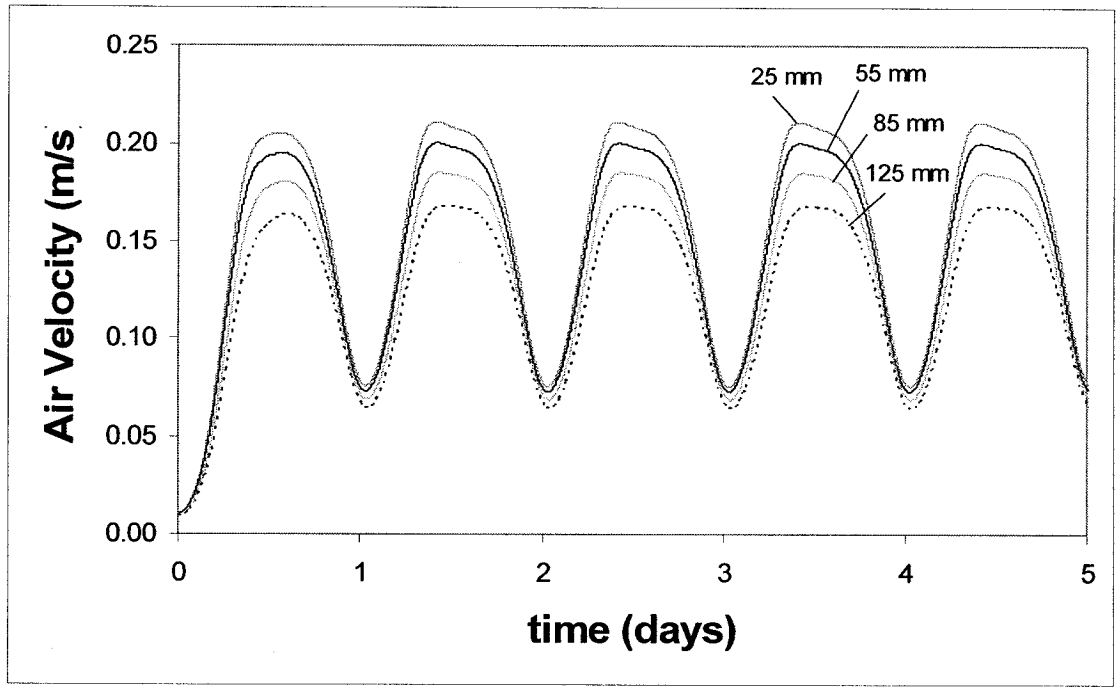

Figure 7.10: Cavity air velocity for varying weephole height dimensions.

7.6 Wind Pressure

While the stated objective of this study is to observe air movement in the cavity due to buoyancy, it would not be complete without some study of the effects of wind pressure on the wall assembly. As stated previously, wind pressure is exceedingly difficult to model due to its complexity and spontaneity. As a result, the base case considered no wind pressure, or 0 Pa. However, many factors, including the height of the building, its cardinal orientation and geographical location, among others, cause varying amounts of wind pressure on a wall. In the case of a brick wall with a rainscreen, one of the main objectives of design is the equalization of the air pressure on the cladding. As such, small constant air pressure differentials are considered to determine their effect on cavity air velocity. It should be noted that a constant wind pressure on a wall over a testing period of five days would be next to impossible, but it is still relevant to determine its theoretical effect. Generally, wind pressure profiles increase from the bottom to the top of the wall, but due to surroundings and obstructions, the opposite can occur. Therefore, the air pressure is considered to act only upon the inlet of the

air flow path, as such the pressures considered could also be seen as the difference between the wind pressure exerted from the outlet to the inlet. The constant wind pressures considered are 2 Pa, 5 Pa, 10 Pa and 20 Pa. This is the equivalent of mild winds ranging from 1.8 to 5.8 m/s, or about 6 to 20 km/h. The results of the simulations may be observed in figure 7.11. The effect of wind pressure on the drying of the brick wall was discussed in the literature review, where wind speeds of 0 to 8 m/s translated into cavity air velocities of 0.2 to 0.6 m/s (Schwarz, 1973). Figure 7.12 demonstrates the drying of the central brick volume over a 15-day testing period.

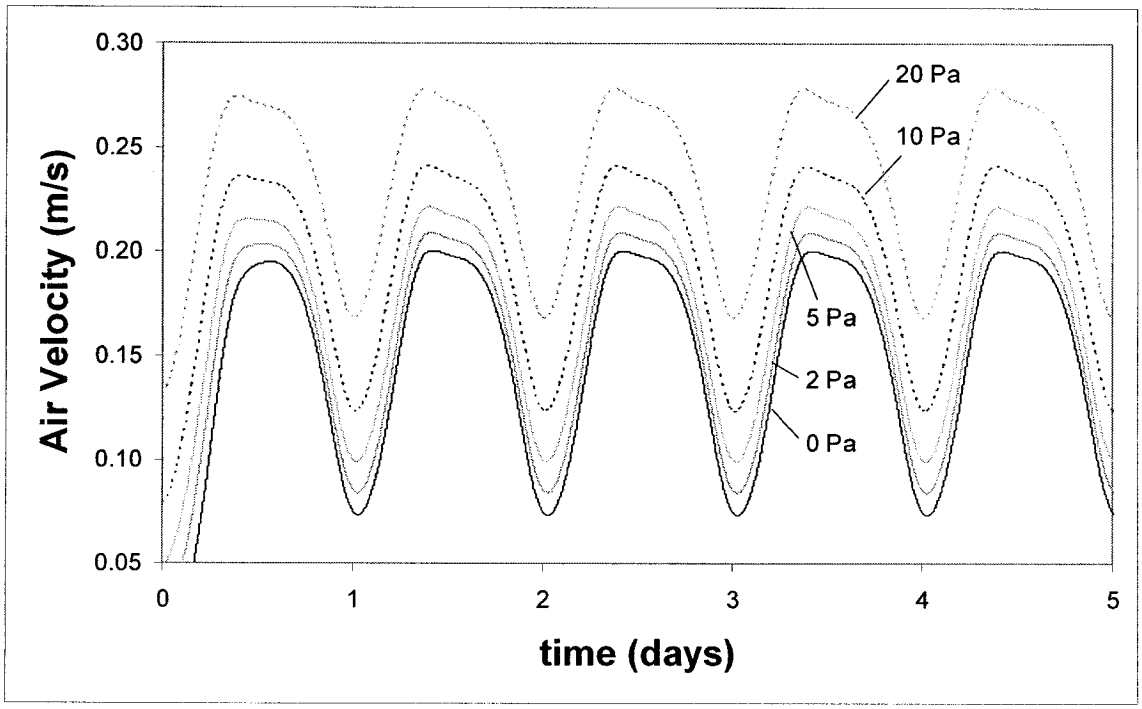

Figure 7.11: Cavity air velocity for increased constant wind pressure on the wall.

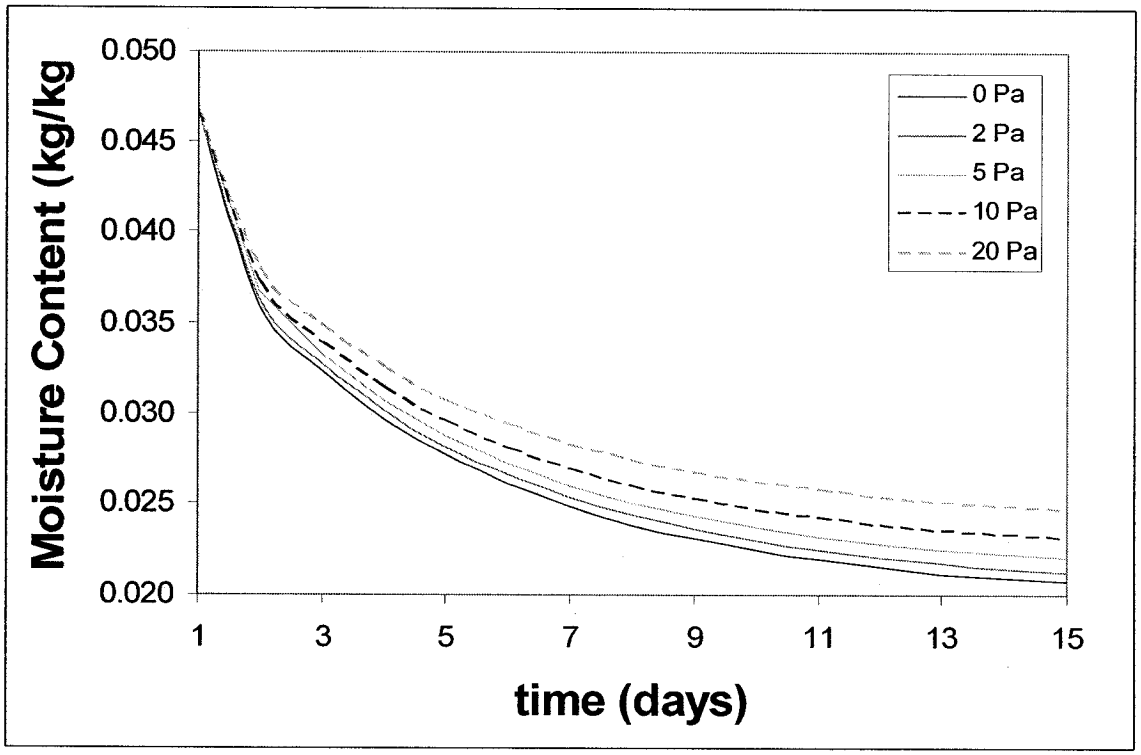

Figure 7.12: Moisture content of central brick node for increased wind pressure on the wall.

In figure 7.11, the main trend to be seen is the notable increase of the air velocity in the cavity from the base case of 0 Pa to a wind pressure of 20 Pa. The magnitude of the peak velocity increases from about 0.20 m/s to 0.28 m/s for that wind pressure differential. It is expected, therefore, as can be seen in the literature, that wind pressure would a significant role to play in the air movement in brick wall cavities. However, the precise effects of wind pressure are best measured in a field study with real conditions and measurements. Such evaluations may take into account the nuances of the arbitrary behavior of wind pressure. In figure 7.12, the results suggest that the lower the wind pressure, and therefore the lower the cavity air velocity, the lower the moisture content at stability. That said, the rate of drying appears to be unaffected by wind pressure, as all curves become stable by the 15^{th} day of testing at about the same rate, albeit at different final moisture contents.

7.7 Conclusion

In this chapter, six basic model parameters were varied to better understand their effects on the results that the model provides. Each of the cases simulated has a significant impact on model results, and, most specifically, most demonstrated significant outcomes on the air velocity and movement in the cavity. Analysis of the results confirmed conclusions from the experimental chapters of this study, as well as the previous studies from the literature review. As a result of this parametric analysis, any model simulations conducted must define the parameters used so that there are no errors when comparative studies between projects are made. The next chapter will conclude the thesis and provide some insight for future projects.

Chapter 8: Conclusion

This chapter concludes the study of measurements and modeling of air and heat flow in a brick wall cavity. In the preceding chapters, a literature review pertinent to this topic was presented, a numerical model was proposed, validation of the model both analytically and experimentally was done, the surface coefficients of the study were better understood and a parametric analysis allowed for complimentary knowledge of the subject. In this chapter, a summary of the findings of the previous chapters is conducted. This is followed by the contributions of this study to the research. Finally, recommendations for future connected projects are made.

8.1 Conclusions

The objectives of the project sought the better understanding of the role of the air cavity in heat and mass transfer through the wall assembly. The validated model results provided a good starting point for this. Air movement in the cavity results in a temperature rise from the top to the bottom, which is the combined result of buoyancy and the convective heat transfer from the brick. This fact was validated by comparison to analytically-derived equations. Much of this heat appears to be evacuated from the assembly as the fiberboard layer on the inside of the cavity is scarcely warmer than the air temperature under most conditions. The air movement in the cavity also plays a significant role in the drying of the wall after quasi-saturation of the brick cladding by rain water. While a certain drying rate may be obtained by the convective heat transfer from the outside air conditions, that rate is clearly accentuated by the presence of air movement on the inside.

Under standard summer conditions for Montreal, the air velocity in the cavity was found to have an approximate peak of 0.20 m/s. This was corroborated by experimental projects on a large-scale wall assembly with the uni-directional anemometer and particle image velocimetry. While the laboratory conditions

were different from the model conditions, when the latter were modified to match the former, there was good agreement in results, which coincidently also demonstrated a peak air velocity of approximately 0.20 to 0.21 m/s.

Also in the particle image velocimetry experiment, it was concluded that the movement of air as it enters the weepholes and begins its ascent in the cavity is quite complex. Images of small vortices were found in the first few centimeters of the flow development, which demonstrates the presence of turbulent flow. This turbulence is the result of the air being released from the confinement of the weephole vent into the vaster expanse of the air cavity as well as the flow separation. Losses that may occur were factored into the model calculations for such a scenario. This flow appears to be short-lived, as quasi-laminar conditions are often found to prevail after less than 10 centimeters of flow development. The air was also found to follow a very narrow path between the lower and upper weepholes, rarely deviating from a pathway that seems to measure only a few centimeters. This confirms equations developed in the literature and validates the assumption that the air flow may be modeled as a series of tubes.

In an experiment to determine the mass transfer coefficients for varying air velocities passing over bricks in a horizontal tunnel, surface coefficients above brick surface are dependent on the air velocity, i.e. that the greater the air velocity in the cavity, the greater the convective mass transfer coefficients. However, a different relationship was observed for velocities at or below 0.10 m/s, and may be due to the difficulty of maintaining such low air velocities with a fan and the increased effect of buoyancy. It is advisable that further experimentation be done to ensure this conclusion is maintained through experimental averages. Also studied was the rate of mass transfer over time, which demonstrates a very high rate of transfer at the beginning of the air flow passing over the brick, with an almost immediate steep decline and finally a slowly dropping plateau until the wall has been dried.

Finally, in a parametric analysis, the variance of six parameters using the model yielded interesting results. Larger cavity diameters and weepholes openings caused the velocity of the air in the cavity to decrease. It was found that by decreasing the surface emissivity of the fiberboard of the backwall, the air velocity of the cavity would also be decreased without a significant change to the air temperature. In terms of the effects of the parameters on the drying rate of the brick cladding, it was first found, predictably, that the intensity of solar radiation had a significant role in the drying rate of the wall. This had more to do with the heat transferred than the air velocity in the cavity, which was nevertheless increased noticeably. The initial relative humidity of the brick is influence the rate of drying of the wall. However, since there is less moisture to evacuate, the case with the lower initial RH had the fastest drying time. Finally, wind pressure was considered for its effects on the cavity air velocity and drying rate of the wall. With a theoretically constant pressure differential applied to the inlet, the air velocity in the cavity was increased with a higher wind pressure. However, the drying time of the brick was mostly unaffected, save for the fact that the moisture content of the wall stabilizes at a higher point when a greater wind pressure differential is applied.

8.2 Contributions of the Research

This study provides several elements that could prove useful to future research in the area of measurements and modeling of air movement in brick wall cavities:

- A working numerical model has been developed and is operational for a wide-range of conditions and parameters;
- A methodology has been proposed for numerical models dealing with air movement in enclosed areas and subject to buoyancy;
- Air flow conditions in the cavity have been predicted and measured.

- Detailed experimental procedures have been discussed for research in the areas of particle image velocimetry and large-scale wind tunnels for cavity flow;
- Images and velocity data for air flow in and just above the inlet of an air cavity are provided;
- An experimental facility for measurements of mass transfer convective coefficients above brick has been developed. A series of tests performed leading to asset of determined heat and mass surface coefficients for wet porous materials exposed to low velocity air flow.
- Experimental data and graphs of the behavior of moisture when air is passed over wetted bricks are provided;
- Comparative data for variation of parameters in the model results, including cavity thickness, solar radiation and wind pressure;
- Analysis and conclusions in the field of air movement in brick wall cavities which can be built upon. This includes, for example, a possible study in PIV of the full height of the cavity.

8.3 Recommendations for Future Research

There are some recommendations that may be made in this area. Since many numerical models for heat, air and moisture flow already exist or are in development, these recommendations will be limited to experimental projects that could be used to validate model results and further the knowledge of this phenomenon.

First and foremost, there appears to be a great need for large-scale field testing to corroborate certain findings of this study, particularly for evaluation of the real effects of wind pressure and solar radiation. In laboratory conditions, it is near impossible to evaluate wind pressure on a large-scale wall, which makes it difficult to validate numerical models. As for solar radiation, it is difficult to replicate its uniform, transient nature with heat lamps. A large-scale field study

could also be useful for the study of moisture content differential due to these conditions.

Refinement of the particle image velocimetry experiment would be greatly beneficial. If the seeding problems of the flow may be solved, it would be of great interest to observe the continuing flow development of the air through the entire cavity and to the outlet, not just at the inlet and slightly above as this study was limited to. As well, if a way could be found to produce images from the bottom of the cavity looking up, the flow development of the air in the z-direction may be seen and the full development of the "air flow tubes" may be visualized and understood. This study could be extended for a variety of environmental conditions and parameters.

Finally, a further experimental analysis of surface coefficients is in order. It would be of interest to continue to the work begun in this study to understand more fully the finding that lower air velocity results in higher convective mass transfer coefficients at very low velocities and study the effect on type of flow, from laminar to transient to turbulent, and type of convection from forced to mixed to natural. There is also a need to determine better approximations of convective mass transfer coefficients for use in modeling and problem-solving. Since the experimental results tend to vary slightly within the limits of acceptable error from one experiment to the next, it would be advisable to conduct several tests at each velocity to evaluate this finding based on experimental averages. Also, if an improvement in design could limit or negate the vibrations on the load cells, the experimental results would have a greater degree of accuracy. This study could also be extended to observe air passing at different relative humidity, or to use bricks that are heated to different temperatures.

References

Adrian, R. J., "Twenty Years of Particle Image Velocimetry", Experiments in Fluids 39, Springer-Verlag, pp.159-169, 2005.

Athienitis, A., "Building Thermal Analysis", MathCAD Electronic Books, Mathsoft Inc, Chapter 7.1, 1993.

BEESL: Building Energy and Environmental Systems Laboratory at Syracuse University (2007), *Champs in Building Envelope Systems,* Retrieved August 1, 2007, from http://beesl.syr.edu/champs.htm

Canadian Real Estate Association (2006), *MLS Online Property Search*, Retrieved April 25, 2005, from http://www.mls.ca/

Chabot, L. and Grooten, K., "Air Velocity in the Cavity", Stage Report for BCEE Department, Concordia University, Montreal, 2006.

Chilton, A., Colburn, A.P., "Mass Transfer (Absorption) Coefficients", Industrial and Engineering Chemistry 26, 1934.

Dantec Dynamics A/S, "Principles of Particle Image Velocimetry (PIV)", Presentation to Concordia University, Montreal, 2005.

Edelstein, J., "Solar-Driven Vapor Transport in Lightweight Walls in a Hot and Humid Climate", M.A.Sc. Thesis, Montreal: Concordia University, 2007.

Energy Information Administration (2000), *Trends in Residential Air Conditioning Usage from 1978 to 1997*, Retrieved April 25, 2005, from http://www.eia.doe.gov/emeu/consumptionbriefs/recs/actrends/recs_ac_trends.html

Fazio, P. and Kontopidis, T., "Cavity Pressure in Rain Screen Walls", Building and Environment Vol. 23, No. 2, pp. 137-143, 1988.

Grau, K. and Rode, C., "A Model for Air Flow in Ventilated Cavities Implemented in a Tool for Whole-Building Hygrothermal Analysis." IEA, Annex 41, Florianopolis, Brazil, 2007.

Guy, R.W. and Stathopoulus, T., "Mechanisms of Pressure Differences Across Building Facades," First Canadian Conference on Building Science and Technology, London, Ont., March 4-5, 1982.

Hansen, M., Nicolajsen, A., and Stang, B., "On the influence of ventilation on moisture content in timber framed walls" Building Physics 2002 – 6th Nordic Symposium, 2002.

Hens, H. and Fatin, A., "Heat-Air-Moisture Design of Masonry Cavity Walls: Theoretical and Experimental Results and Practice", ASHRAE Transactions, CH-95-3-2, pp. 607-626, 1995.

Hutcheon, N.B., "Fundamental Considerations in the Design of Exterior Walls for Buildings," NRC Paper No. 3087, DBR No. 37. Ottawa: Division of Building Research, 1953.

Hutcheon, N. B., Handegord, G., "Building Science for a Cold Climate", National Research Council Canada, Third Printing, Chapters 9 and 11, 1995.

Janssens, A., "Reliable Control of Interstitial Condensation in Lightweight Roof Systems", Ph.D. thesis: Université Catholique de Leuven, 1998.

Kreith, F., Bohn, M.S. "Principles of heat transfer." 6th Edition, Brooks/Cole, 2001.

Kumar, S., "Pressure Equalized Rainscreen Approach to Wall Design: Past Accomplishments and Future Challenges", Technical Report Fago 98.25.K, Faculteit Bouwkunde, Chapter 1, p. 1-5, 1998.

Kumaran, M., "A Thermal and Moisture Transport Database for Common Building and Insulating Materials", Final Report from ASHRAE Research Project 1018-RP, 2002.

Künzel, H., Mayer, E., "Untersuchung über die notwendige Hinterlüftung an Außenwandbekeidung aus großformatigen Bauteilen", Schriftenreihe Bundesminister für Raumordnung, Bauwesen, und Städtebau, 1983.

Landon, M. and Campo, A.,"Optimal Shape for Natural Convective Cavities Containing Air and Heated From the Side", Int. Comm. Heat Mass Transfer, Vol. 26, No. 3, pp. 389-398, 1999.

Lauriat, G. and Desrayaud, G., "Effect of Surface Radiation on Conjugate Natural Convection in Partially Open Enclosures", International Journal of Thermal Sciences 45, pp. 335-346, 2006.

Lienhard IV, J.H., Lienhard V, J.H. "A Heat Transfer Textbook", Phlogiston Press, 2006.

Melling, A., and Whitelaw, J. H., "Seeding of gas flows for laser anemometry", DISA Information 15, pp. 5-14, 1973.

Melling, A., "Tracer Particles and Seeding for particle image velocimetry, Measurements", Science and Technology 8, IOP Publising, pp. 1406-1416, 1997.

Morton, K., and Mayers, D., "Numerical solution of partial differential equations : an introduction", Cambridge University Press, Cambridge, UK, 1994.

Salonvaara, M. H., Ojanen, T., Kokko, E. and Karagiozis, A. N., "Drying capabilities of wood frame walls with wood siding", Thermal Performance of the Exterior Envelopes of Buildings VII, Clearwater, Florida, pp. 165-177, 1998.

Sandin, Kenneth, "Moisture Conditions in Cavity Walls with Wooden Framework", *Building Research and Inf.*, vol 21, no. 4, 1993.

Schwarz, B., "Witterungsbeansphruchung von Hochhausfassaden," HLH Bd. 24, Nr. 12, pp. 376-384, 1973.

Straube, J. and Burnett, E., "Vents, Ventilation, and Pressure Moderation", Building Engineering Group Report for Canada Mortgage and Housing Corporation, Ottawa, 1995.

Straube, J. F. and Burnett, E. F. P., "Drainage, ventilation drying and enclosure performance", Thermal Performance of the Exterior Envelopes of Buildings VII, Clear water Beach, Florida, pp. 189, 1998.

Straube, J., and Burnett, E., "Vents, Ventilation and Masonry Veneer Wall Systems", Procedures of the Eighth Canadian Masonry Symposium, Jasper, Alberta, pp. 194-207, 1998.

Stovall, T. and Karaziogis, A., "CFD Analysis of a Ventilated Brick Cavity", Oak Ridge National Laboratory, Annex 41 Meeting, Lyon, 2005.

TenWolde, A., and Carll, C., "Effect of cavity ventilation on moisture in walls and roofs", Proceedings of the Thermal Performance of the Exterior Envelopes of Buildings V, Clearwater Beach, Florida, December 710, pp. 555-562, 1992.

TenWolde, A. and Mei, H.T., "Moisture movement in walls in a warm, humid climate," Presented at ASHRAE/DOE/BTECC Conference in Clearwater Beach, Florida, 1986.

Zheng et al., "An evaluation of highly insulated cold zinc roofs in a moderate humid region – part I: hygrothermal performance", Catholic University of Leuven, Belgium and Elsevier Science Ltd, p. 49-59, 2003.

Appendix A

Determination of solar radiation

The calculation method for solar radiation was elaborated by Athienitis (1993) and assumes angles and magnitudes corresponding to those in figure A.1. The transient nature of the solar position requires a specific set of conditions that are dependent upon the location of the wall, its position, the time of year, etc. Most importantly, many are dependant on the time of day, in which case they will be listed as a function of *t*, which is the number of seconds passed on the day of measurement starting at midnight.

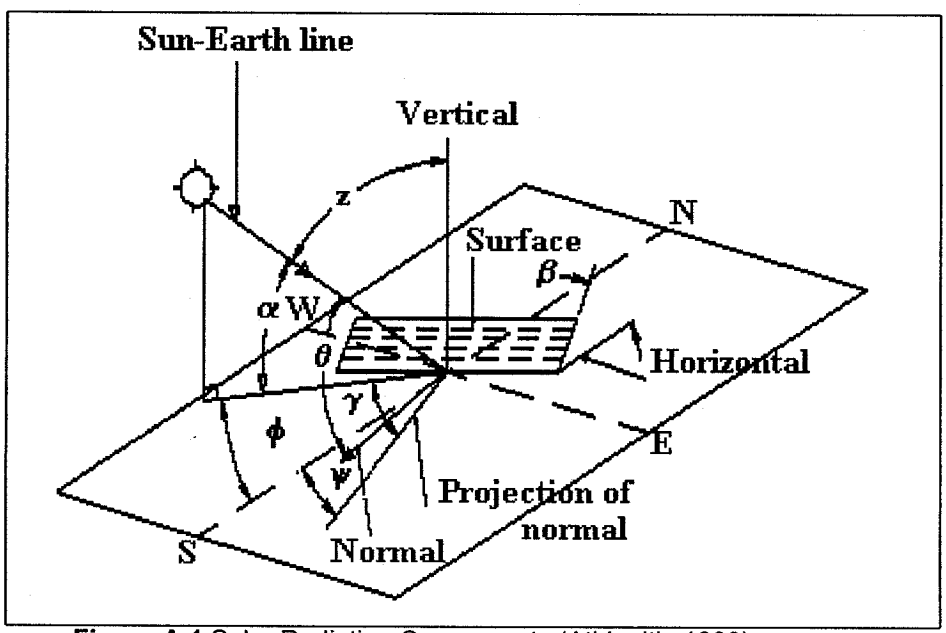

Figure A.1 Solar Radiation Components (Athienitis 1993)

The declination angle δ is the angle of the sun [rad] dependent on the time of the year, and is given by equation A.1, where *dm* is the numerical day of the year out of 365.

$$\delta = 0.4093 \cdot \sin\left[2\pi \cdot \left(\frac{284 + dm}{365}\right)\right] \qquad \text{(A.1)}$$

The hour angle *h(t)* [rad] in equation A.2 indicates the number of seconds to or from solar noon multiplied by the number of radians per second for the 24-hour testing period, *rs*, which is calculation via equation A.3.

$$h(t) = (t - 43200) \cdot rs \tag{A.2}$$

$$rs = \frac{2\pi}{24h \cdot 60m \cdot 60s} \tag{A.3}$$

The solar altitude $\alpha(t)$ in equation A.4 is the angle [rad] of the sun to the ground dependent upon the declination angle, hour angle and latitude of the location.

$$\alpha(t) = \sin^{-1}\left(\cos(lat) \cdot \cos(\delta) \cdot \cos(h(t)) + \sin(lat) \cdot \sin(\delta)\right) \tag{A.4}$$

The solar azimuth $\phi(t)$ is the angle [rad] of the projection of the solar altitude on the ground with the South cardinal point. It is determined by equation A.5.

$$\phi(t) = \cos^{-1}\left(\frac{\sin(\alpha(t)) \cdot \sin(lat) - \sin(\delta)}{\cos(\alpha(t)) \cdot \cos(lat)}\right) \cdot \frac{h(t)}{|h(t)|} \tag{A.5}$$

We define the zenith angle, *z(t)*, in [rad], as the angle between the solar altitude and the vertical.

$$z(t) = \frac{\pi}{2} - \alpha(t) \tag{A.6}$$

The surface solar azimuth angle, $\gamma(t)$ in [rad] is depicted in equation A.7. It represents the difference between the solar azimuth and the surface azimuth angle, Ψ, which itself is the angle difference between a projection of the normal to the wall and the South cardinal point. However, since Ψ is set to zero as the wall is South-facing, $\gamma(t)$ is effectively equal to $\phi(t)$.

$$\gamma(t) = \phi(t) - \psi \tag{A.7}$$

We now define the incidence angle $\theta(t)$, which indicates the difference in [rad] between the solar altitude and the actual normal of the wall. The wall is modeled to be vertical therefore the tilt angle β in [rad] is set to be (π/2).

$$\theta(t) = \cos^{-1}\left(\cos(\alpha(t)) \cdot \cos(|\gamma(t)|) \cdot \sin(\beta) + \sin(\alpha(t) \cdot \cos(\beta))\right) \quad \text{(A.8)}$$

The transmittances for beam and diffuse radiation must be determined. These are dimensionless ratios that determine the proportion of direct, reflected and diffuse radiation that will be transmitted to the brick wall. The transmittance for beam radiation, $\tau_b(t)$, is described by equation A.9, while the transmittance for diffuse radiation, $\tau_d(t)$, is given by equation A.10.

$$\tau_b(t) = \left(a_o + a_1 \cdot \exp\left(\frac{-\kappa}{\cos(\alpha(t))}\right)\right) \quad \text{(A.9)}$$

$$\tau_d(t) = 0.2710 - 0.2939 \cdot \tau_b(t) \quad \text{(A.10)}$$

Where:

$$a_o = r_o \cdot \left[0.4237 - 0.00821 \cdot (6 - alt)^2\right]$$
$$a_1 = r_1 \cdot \left[0.5055 + 0.00595 \cdot (6.5 - alt)^2\right]$$
$$\kappa = r_\kappa \cdot \left[0.2711 + 0.01858 \cdot (2.5 - alt)^2\right]$$

The terms r_o, r_1 and r_κ are location factors for mid-latitude in the summer months. They are set to values of r_o=0.97, r_1=0.99 and r_κ=1.02.

The extraterrestrial solar radiation [W] is the magnitude of heat transferred by the sun that will form the basis for the components of total solar radiation that affects the brick wall. The following equation, A.11, is given to describe I_{on} for Montreal:

$$I_{on} = 1353 \cdot \left(1 + 0.033 \cdot \cos\left(2\pi \cdot \frac{dm}{365}\right)\right) \quad \text{(A.11)}$$

There are three components of total solar radiation, all of which are expressed in [W]. Firstly, the beam direct component, I_b, is the radiation caused by the rays directly incident on the wall, and is defined by equation A.12. Secondly, the ground reflected component, $I_{dg}(t)$, describes the rays that reflect on the wall after

having first deflected off the ground. $I_{dg}(t)$ is defined by equation A.13. For this component, we define a reflection ratio, *SR*, which defines the proportion of the beams that will not be absorbed by the ground and thus will reflect onto the wall. *SR* is assumed to be 0.32. Finally, the diffuse sky radiation is the radiation that has been scattered from the direct solar beam by molecules and other suspended particles in the Earth's atmosphere. $I_{ds}(t)$ is defined by equation A.14.

$$I_b(t) = I_{on} \cdot \tau_b(t) \cdot \cos(\theta(t)) \tag{A.12}$$

$$I_{dg}(t) = I_{on} \cdot \sin(\alpha(t)) \cdot (\tau_b + \tau_d) \cdot SR \cdot \frac{1-\cos(\beta)}{2} \tag{A.13}$$

$$I_{ds}(t) = I_{on} \cdot \sin(\alpha(t)) \cdot \tau_d \cdot \frac{1+\cos(\beta)}{2} \tag{A.14}$$

The instantaneous solar radiation, $I_t(t)$, that is incident on the brick wall may finally be defined as the total of its three constituent components, as per equation A.15. It is expressed in [W] and is dependent on the number of seconds *t* that have elapsed since the start of the testing period.

$$I_t(t) = I_b(t) + I_{ds}(t) + I_{dg}(t) \tag{A.15}$$

Appendix B

Friction Factors Used in this Study

Table B.1

Friction factor f (Hens 2005)

Reynolds number [1]	Flow	Friction Factor f
$Re \leq 2500$	laminar	96/Re
$2500 \leq Re \leq 3500$	critical	$\frac{0,038\,(3500 - Re) + f_{T,Re=2500}(Re - 2500)}{1000}$
$Re > 3500$	turbulent	f_T [2]
$Re >> 3500$	stable turbulent	$f_T = C^{te}$, single function of the relative roughness

[1] $Re = \frac{v\, d_H}{\nu}$ where v is the average flow velocity, ν the kinematic viscosity and d_H the hydraulic radius, given by:

for a circular section: d_H is the diameter of the circle

for a rectangular section: $d_H = \frac{2ab}{a+b}$, where a and b are the sides of the rectangular

for a cavity: $d_H = 2b$, where b is the width of the cavity

Re can also be written as: $Re \approx 56000 g_a d_H$ with g_a the air flow rate

[2] $f_T = \left[2\log\left(-4,793\log\frac{\frac{10}{Re} + \frac{0,2\varepsilon}{d_H}}{Re} + 0,2698\frac{\varepsilon}{d_H} \right) \right]^{-2}$ where ε is the roughness (see fig. 2.6).

Table B.2

Factor of local loss ξ (Hens 2005)

<table>
<tr><th>Local resistance</th><th colspan="5">ξ</th></tr>
<tr><td>Entering an opening</td><td colspan="5">0.5</td></tr>
<tr><td>Going out an opening</td><td colspan="5">1.0</td></tr>
<tr><td rowspan="4">Widening
$\sigma=A_0/A_1$
A_0 small section
A_1 large section</td><td>$Re \leq 1000$</td><td colspan="4">$-0{,}036+9{,}6\cdot10^{-5}Re+\Delta\xi$</td></tr>
<tr><td>$1000<Re\leq3000$</td><td colspan="4">$1{,}28\cdot10^{-5}Re^{1{,}223}+\Delta\xi$</td></tr>
<tr><td>$Re>3000$</td><td colspan="4">$0{,}21\,Re^{0{,}012}+\Delta\xi$</td></tr>
<tr><td>$\sigma\leq0{,}5$
$\sigma>0{,}5$</td><td colspan="4">$\Delta\xi=0{,}78-1{,}56\sigma$
$\Delta\xi=0{,}48-0{,}96\sigma$</td></tr>
<tr><td rowspan="4">Narrowing
$\sigma=A_0/A_1$
A_0 large section
A_1 small section</td><td>$Re\leq1000$</td><td colspan="4">$0{,}98\,Re^{-0{,}03}+A$</td></tr>
<tr><td>$1000<Re\leq3000$</td><td colspan="4">$10{,}59\,Re^{-0{,}37}+A$</td></tr>
<tr><td>$Re>3000$</td><td colspan="4">$0{,}57\,Re^{-0{,}01}+A$</td></tr>
<tr><td colspan="5">$A=0{,}0373\sigma^2-0{,}067\sigma$</td></tr>
<tr><td>Leak</td><td colspan="5">2,85</td></tr>
<tr><td rowspan="5">Angle or curve

b_0; width admission channel
b_1; width of channel after the curve
$_0$; refers to the admission channel
f_0 ; friction factor in admission channel</td><td colspan="5">$\frac{k_{Re0}\xi_g k_0}{(d_H)_0}$ where $\xi_g=0{,}885\left(\frac{b_1}{b_0}\right)^{-0{,}86}$ and</td></tr>
<tr><td>ε</td><td colspan="2">$3000\leq Re<40000$</td><td colspan="2">$Re\geq40000$</td></tr>
<tr><td></td><td>k_{Re0}</td><td>$k_0/(d_H)_0$</td><td>k_{Re0}</td><td>$k_0/(d_H)_0$</td></tr>
<tr><td>0</td><td>$45f_o$</td><td>1</td><td>1.1</td><td>1</td></tr>
<tr><td>0-0.001</td><td>$45f_o$</td><td>1</td><td>1.0</td><td>$1+0{,}5\ 10^3a$</td></tr>
<tr><td>>0.001</td><td>$45f_o$</td><td>1</td><td>1.1</td><td>1</td></tr>
</table>

Appendix C

Detailed Description of Equations Developed for Boundary/Discontinuous Conditions

C.1 Heat Transfer - Brick Surface Node Bordering Cavity

The brick surface node bordering the cavity is important in calculations as this is where heat is transmitted from the brick into the air of the cavity. The equations of heat transfer by convection and conduction can be found in Chapter 2. There are four thermal conduction terms for the four adjacent nodes, three brick nodes and one air cavity node. There is thermal convection from the cavity, and the thermal storage term for the right-hand side of the heat balance. A graphical representation of the situation may be visualized in figure C.1. We obtain therefore:

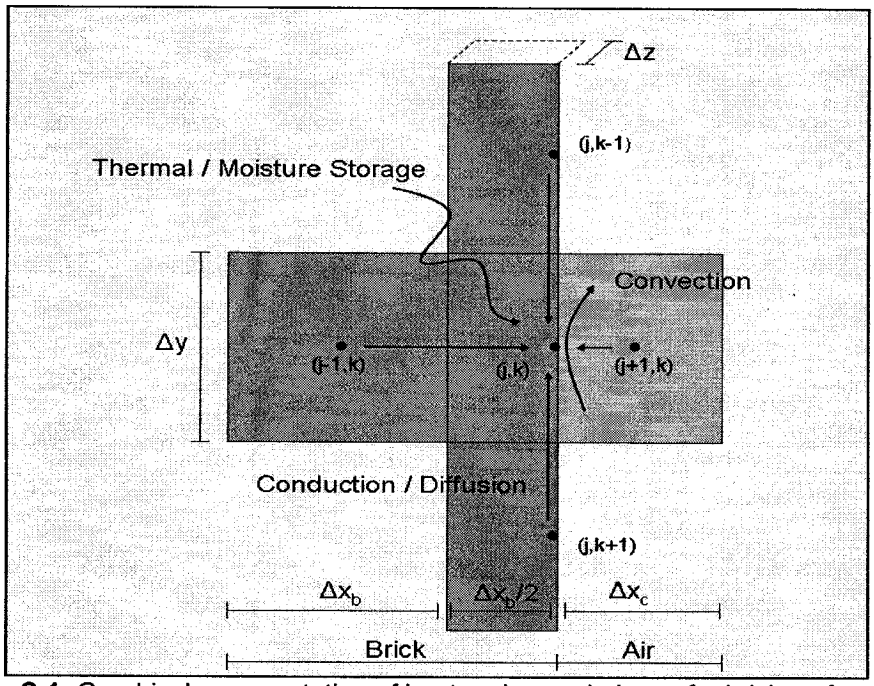

Figure C.1: Graphical representation of heat and mass balance for brick surface node

Conduction from (j-1,k) to (j,k) + Conduction from (j,k+1) to (j,k)
+ Conduction from (j,k-1) to (j,k) + Conduction from (j+1,k) to (j,k)
+ Convection from (j+1,k) to (j,k) = Thermal storage from (n) to (n+1)

$$\frac{k_b \Delta y \Delta z}{\Delta x_b}(T^{n+1}_{(j-1,k)} - T^{n+1}_{(j,k)}) + \frac{k_b \Delta x_b \Delta z}{2\Delta y}(T^{n+1}_{(j,k+1)} - T^{n+1}_{(j,k)}) + \frac{k_b \Delta x_b \Delta z}{2\Delta y}(T^{n+1}_{(j,k-1)} - T^{n+1}_{(j,k)})$$

$$+ \frac{k_a \Delta y \Delta z}{\Delta x_b}(T^{n+1}_{(j+1,k)} - T^{n+1}_{(j,k)}) + h_{cv} \Delta y \Delta z (T^{n+1}_{(j+1,k)} - T^{n+1}_{(j,k)}) =$$

$$\frac{\rho_b c_b \Delta x_b \Delta y \Delta z}{2\Delta t}(T^{n+1}_{(j,k)} - T^{n}_{(j,k)})$$

This may be simplified in a way to add all constant terms into coefficients which multiply the individual temperature components. The right-hand side of the equation assembles all known components and temperatures. We obtain thus:

$$[- \frac{k_b \Delta y \Delta z}{\Delta x_b} - 2\frac{k_b \Delta x_b \Delta z}{2\Delta y} + h_{cv} \Delta y \Delta z - \frac{\rho_b c_b \Delta x_b \Delta y \Delta z}{2\Delta t}] T^{n+1}_{(j,k)}$$

$$+ [\frac{k_b \Delta x_b \Delta z}{2\Delta y}] T^{n+1}_{(j,k-1)} + [\frac{k_b \Delta x_b \Delta z}{2\Delta y}] T^{n+1}_{(j,k+1)} + [- h_{cv} \Delta y \Delta z] T^{n+1}_{(j+1,k)}$$

$$+ [\frac{k_b \Delta x_b \Delta z}{2\Delta y}] T^{n+1}_{(j-1,k)} = - \frac{\rho_b c_b \Delta x_b \Delta y \Delta z}{2\Delta t} T^{n}_{(j,k)}$$

Rearranging these coefficients, we may obtain the [C] and [R] matrices for all nodes of the network that correspond to this situation (column 4 of figure 3.7). Therefore,

$$C_1 = - \frac{k_b \Delta y \Delta z}{\Delta x_b} - 2\frac{k_b \Delta x_b \Delta z}{2\Delta y} + h_{cv} \Delta y \Delta z - \frac{\rho_b c_b \Delta x_b \Delta y \Delta z}{2\Delta t}$$

$$C_2 = \frac{k_b \Delta x_b \Delta z}{2\Delta y} \qquad C_3 = \frac{k_b \Delta x_b \Delta z}{2\Delta y} \qquad C_4 = - h_{cv} \Delta y \Delta z$$

$$C_5 = \frac{k_b \Delta x_b \Delta z}{2\Delta y} \qquad R = - \frac{\rho_b c_b \Delta x_b \Delta y \Delta z}{2\Delta t} T^{n}_{(j,k)}$$

C.2 Moisture Transfer - Brick Surface Node Bordering Cavity

The brick surface node bordering the cavity is important in calculations as this is where moisture is transmitted from the brick into the air of the cavity, thereby drying the brick. The equations of moisture transfer by convection and diffusion can be found in Chapter 2. There are four vapor diffusion terms for the four

adjacent nodes, three brick nodes and one air cavity node. There is moisture convection from the cavity, and the moisture storage term for the right-hand side of the mass balance. A graphical representation of the situation may be visualized in figure C.1. We obtain therefore:

Diffusion from (j-1,k) to (j,k) + Diffusion from (j,k+1) to (j,k)
+ Diffusion from (j,k-1) to (j,k) + Diffusion from (j+1,k) to (j,k)
+ Convection from (j+1,k) to (j,k) = Moisture storage from (n) to (n+1)

$$\frac{\delta_b(\phi)\Delta y\Delta z}{\Delta x_b}(p^{n+1}_{v(j-1,k)} - p^{n+1}_{v(j,k)}) + \frac{\delta_b(\phi)\Delta x_b\Delta z}{2\Delta y}(p^{n+1}_{v(j,k+1)} - p^{n+1}_{v(j,k)}) +$$
$$\frac{\delta_b(\phi)\Delta x_b\Delta z}{2\Delta y}(p^{n+1}_{v(j,k-1)} - p^{n+1}_{v(j,k)}) + \frac{\delta_b(\phi)\Delta y\Delta z}{\Delta x_b}(p^{n+1}_{v(j+1,k)} - p^{n+1}_{v(j,k)}) +$$
$$h_m\Delta y\Delta z(p^{n+1}_{v(j-1,k)} - p^{n+1}_{v(j,k)}) = \frac{\rho_b\xi_b(\phi)\Delta x_b\Delta y\Delta z}{2\Delta t\cdot p^n_{v,sat}}(p^{n+1}_{v(j,k)} - p^n_{v(j,k)})$$

This may be simplified in a way to add all constant terms into coefficients which multiply the individual temperature components. The right-hand side of the equation assembles all known components and temperatures. We obtain thus:

$$[-\frac{\delta_b(\phi)\Delta y\Delta z}{\Delta x_b} - 2\frac{\delta_b(\phi)\Delta x_b\Delta z}{2\Delta y} + h_m\Delta y\Delta z - \frac{\rho_b\xi_b(\phi)\Delta x_b\Delta y\Delta z}{2\Delta t}]\ p^{n+1}_{v(j,k)}$$
$$+ [\frac{\delta_b(\phi)\Delta x_b\Delta z}{2\Delta y}]\ p^{n+1}_{v(j,k-1)} + [\frac{\delta_b(\phi)\Delta x_b\Delta z}{2\Delta y}]\ p^{n+1}_{v(j,k+1)} + [-h_m\Delta y\Delta z]\ p^{n+1}_{v(j+1,k)}$$
$$+ [\frac{\delta_b(\phi)\Delta x_b\Delta z}{2\Delta y}]\ p^{n+1}_{v(j-1,k)} = -\frac{\rho_b\xi_b(\phi)\Delta x_b\Delta y\Delta z}{2\Delta t\cdot p^n_{v,sat}}\ p^n_{v(j,k)}$$

Rearranging these coefficients, we may obtain the [G] and [S] matrices for all nodes of the network that correspond to this situation (column 4 of figure 3.7). Therefore,

$$G_1 = -\frac{\delta_b(\phi)\Delta y\Delta z}{\Delta x_b} - 2\frac{\delta_b(\phi)\Delta x_b\Delta z}{2\Delta y} + h_m\Delta y\Delta z - \frac{\rho_b\xi_b(\phi)\Delta x_b\Delta y\Delta z}{2\Delta t}$$

$$G_2 = \frac{\delta_b(\phi)\Delta x_b\Delta z}{2\Delta y} \qquad G_3 = \frac{\delta_b(\phi)\Delta x_b\Delta z}{2\Delta y} \qquad G_4 = -h_m\Delta y\Delta z$$

$$G_5 = \frac{\delta_b(\phi)\Delta x_b \Delta z}{2\Delta y} \qquad S = - \frac{\rho_b \xi_b(\phi)\Delta x_b \Delta y \Delta z}{2\Delta t \cdot p^n_{v,sat}} \, p^n_{v(j,k)}$$

C.3 Heat Transfer - Air Cavity Nodes

The air cavity nodes are central to this study and therefore their accurate modeling is of great interest. There are four thermal conduction terms for the four adjacent nodes - one brick node, two air cavity nodes and one fiberboard node. There is thermal convection affecting both the brick and fiberboard surfaces. The movement of air causes heat transfer, as does the radiation exchange between the two facing surfaces. As before, there is a thermal storage term for the right-hand side of the heat balance. A graphical representation of the situation may be visualized in figure C.2. The heat balance will therefore take the following form:

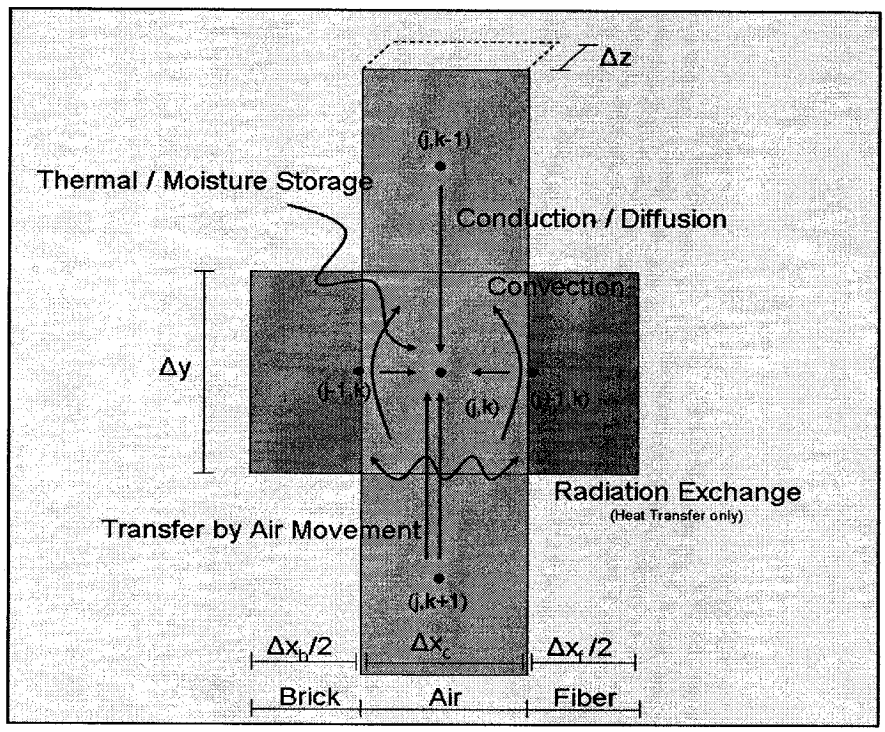

Figure C.2: Graphical representation of heat and mass balance for air cavity node

Conduction from (j-1,k) to (j,k) + Conduction from (j,k+1) to (j,k)
+ Conduction from (j,k-1) to (j,k) + Conduction from (j+1,k) to (j,k)
+ Convection from (j-1,k) to (j,k) + Convection from (j+1,k) to (j,k)

+ Air Movement heat transfer from (j,k+1) to (j,k)
+ Radiation exchange between (j-1,k) and (j+1,k)
= Thermal storage from (n) to (n+1)

$$\frac{2k_a\Delta y\Delta z}{\Delta x_c}(T^{n+1}_{(j-1,k)}-T^{n+1}_{(j,k)}) + \frac{k_a\Delta x_c\Delta z}{\Delta y}(T^{n+1}_{(j,k+1)}-T^{n+1}_{(j,k)}) + \frac{k_a\Delta x_c\Delta z}{\Delta y}(T^{n+1}_{(j,k-1)}-T^{n+1}_{(j,k)})$$

$$+ \frac{2k_a\Delta y\Delta z}{\Delta x_c}(T^{n+1}_{(j+1,k)}-T^{n+1}_{(j,k)}) + h_{cv}\Delta y\Delta z(T^{n+1}_{(j-1,k)}-T^{n+1}_{(j,k)}) + h_{cv}\Delta y\Delta z(T^{n+1}_{(j+1,k)}-T^{n+1}_{(j,k)})$$
$$+ \rho_a c_a v_c\Delta x_c(T^{n+1}_{(j,k+1)}-T^{n+1}_{(j,k)}) + h_{rad}\Delta y\Delta z(T^{n+1}_{(j-1,k)}-T^{n+1}_{(j+1,k)})$$
$$= \frac{\rho_a c_a\Delta x_c\Delta y\Delta z}{\Delta t}(T^{n+1}_{(j,k)}-T^{n}_{(j,k)})$$

In the simplified coefficient form, we obtain:

$$[-\frac{4k_a\Delta y\Delta z}{\Delta x_c} - \frac{2k_a\Delta x_c\Delta z}{\Delta y} - 2h_{cv}\Delta y\Delta z - \rho_a c_a v_c\Delta x_c - h_{rad}\Delta y\Delta z -$$
$$\frac{\rho_a c_a\Delta x_c\Delta y\Delta z}{\Delta t}]T^{n+1}_{(j,k)} + [\frac{k_a\Delta x_c\Delta z}{\Delta y}]T^{n+1}_{(j,k-1)} + [\frac{k_a\Delta x_c\Delta z}{\Delta y} + \rho_a c_a v_c\Delta x_c]T^{n+1}_{(j,k+1)}$$
$$+[\frac{2k_a\Delta y\Delta z}{\Delta x_c} + h_{cv}\Delta y\Delta z + h_{rad}\Delta y\Delta z]T^{n+1}_{(j+1,k)}$$
$$+[\frac{2k_a\Delta y\Delta z}{\Delta x_c} + h_{cv}\Delta y\Delta z - h_{rad}\Delta y\Delta z]T^{n+1}_{(j-1,k)} = -\frac{\rho_a c_a\Delta x_c\Delta y\Delta z}{\Delta t}T^{n}_{(j,k)}$$

And therefore for the coefficient matrix [C], we obtain:

$$C_1 = -\frac{4k_a\Delta y\Delta z}{\Delta x_c} - \frac{2k_a\Delta x_c\Delta z}{\Delta y} - 2h_{cv}\Delta y\Delta z - \rho_a c_a v_c\Delta x_c - h_{rad}\Delta y\Delta z - \frac{\rho_a c_a\Delta x_c\Delta y\Delta z}{\Delta t}$$

$$C_2 = \frac{k_a\Delta x_c\Delta z}{\Delta y} \qquad C_3 = \frac{k_a\Delta x_c\Delta z}{\Delta y} + \rho_a c_a v_c\Delta x_c$$

$$C_4 = \frac{2k_a\Delta y\Delta z}{\Delta x_c} + h_{cv}\Delta y\Delta z + h_{rad}\Delta y\Delta z \qquad C_5 = \frac{2k_a\Delta y\Delta z}{\Delta x_c} + h_{cv}\Delta y\Delta z - h_{rad}\Delta y\Delta z$$

$$R = -\frac{\rho_a c_a\Delta x_c\Delta y\Delta z}{\Delta t}T^{n}_{(j,k)}$$

C.4 Moisture Transfer - Air Cavity Nodes

Moisture transfer within the cavity is central to this study. There are four thermal diffusion terms for the four adjacent nodes - one brick node, two air cavity nodes and one fiberboard node. There is moisture convection affecting both the brick and fiberboard surfaces and the movement of air in the cavity also causes moisture transfer. As before, there is a moisture storage term for the right-hand side of the heat balance. A graphical representation of the situation may be visualized in figure C.2. The mass balance will therefore take the following form:

Diffusion from (j-1,k) to (j,k) + Diffusion from (j,k+1) to (j,k)
+ Diffusion from (j,k-1) to (j,k) + Diffusion from (j+1,k) to (j,k)
+ Convection from (j-1,k) to (j,k) + Convection from (j+1,k) to (j,k)
+ Air Movement mass transfer from (j,k+1) to (j,k)
= Moisture storage from (n) to (n+1)

$$\frac{2\delta_a(\phi)\Delta y\Delta z}{\Delta x_c}(p^{n+1}_{v(j-1,k)} - p^{n+1}_{v(j,k)}) + \frac{\delta_a(\phi)\Delta x_c\Delta z}{\Delta y}(p^{n+1}_{v(j,k+1)} - p^{n+1}_{v(j,k)})$$
$$+ \frac{\delta_a(\phi)\Delta x_c\Delta z}{\Delta y}(p^{n+1}_{v(j,k-1)} - p^{n+1}_{v(j,k)}) + \frac{2\delta_a(\phi)\Delta y\Delta z}{\Delta x_c}(p^{n+1}_{v(j+1,k)} - p^{n+1}_{v(j,k)}) +$$
$$h_m\Delta y\Delta z(p^{n+1}_{v(j-1,k)} - p^{n+1}_{v(j,k)}) + h_m\Delta y\Delta z(p^{n+1}_{v(j+1,k)} - p^{n+1}_{v(j,k)}) +$$
$$\rho_a\xi_a v_c\Delta x_c(p^{n+1}_{v(j,k+1)} - p^{n+1}_{v(j,k)}) = \frac{\rho_a\xi_a\Delta x_c\Delta y\Delta z}{\Delta t\cdot p^n_{v,sat}}(p^{n+1}_{v(j,k)} - p^n_{v(j,k)})$$

In the simplified coefficient form, we obtain:

$$[-\frac{4\delta_a(\phi)\Delta y\Delta z}{\Delta x_c} - \frac{2\delta_a(\phi)\Delta x_c\Delta z}{\Delta y} - 2h_m\Delta y\Delta z - \rho_a\xi_a v_c\Delta x_c - \frac{\rho_a\xi_a\Delta x_c\Delta y\Delta z}{\Delta t\cdot p^n_{v,sat}}]\ p^{n+1}_{v(j,k)}$$
$$+[\frac{\delta_a(\phi)\Delta x_c\Delta z}{\Delta y}]\ p^{n+1}_{v(j,k-1)} + [\frac{\delta_a(\phi)\Delta x_c\Delta z}{\Delta y} + \rho_a\xi_a v_c\Delta x_c]\ p^{n+1}_{v(j,k+1)}$$
$$+[\frac{2\delta_a(\phi)\Delta y\Delta z}{\Delta x_c} + h_m\Delta y\Delta z]\ p^{n+1}_{v(j+1,k)} + [\frac{2\delta_a(\phi)\Delta y\Delta z}{\Delta x_c} + h_m\Delta y\Delta z]\ p^{n+1}_{v(j+1,k)}$$
$$= -\frac{\rho_a\xi_a\Delta x_c\Delta y\Delta z}{\Delta t\cdot P^n_{v,sat}}\ p^n_{v(j,k)}$$

Rearranging these coefficients, we may obtain the [G] and [S] matrices:

$$G_1 = -\frac{4\delta_a(\phi)\Delta y\Delta z}{\Delta x_c} - \frac{2\delta_a(\phi)\Delta x_c\Delta z}{\Delta y} - 2h_m\Delta y\Delta z - \rho_a\xi_a v_c\Delta x_c - \frac{\rho_a\xi_a\Delta x_c\Delta y\Delta z}{\Delta t\cdot p^n_{v,sat}}$$

$$G_2 = \frac{\delta_a(\phi)\Delta x_c\Delta z}{\Delta y} \qquad G_3 = \frac{\delta_a(\phi)\Delta x_c\Delta z}{\Delta y} + \rho_a\xi_a v_c\Delta x_c$$

$$G_4 = \frac{2\delta_a(\phi)\Delta y\Delta z}{\Delta x_c} + h_m\Delta y\Delta z \qquad G_5 = \frac{2\delta_a(\phi)\Delta y\Delta z}{\Delta x_c} + h_m\Delta y\Delta z$$

$$S = -\frac{\rho_a\xi_a\Delta x_c\Delta y\Delta z}{\Delta t\cdot P^n_{v,sat}}\, p^n_{v(j,k)}$$

Appendix D

Particle Image Velocimetry Results

The five testing periods from 3.0 hours of heat lamp exposure to 7.0 hours of heat lamp exposure are presented in this appendix in Tables D.1 to D.5. The vector maps shown below the images represent the visible seeded area only, and not the dark region above it.

Table D.1: Test Period 1

3.0 Hours of Heat Lamp Exposure

	Exterior Brick	Interior Brick	Cavity Backwall
Surface Temperature	56.81°C	44.77°C	35.65°C

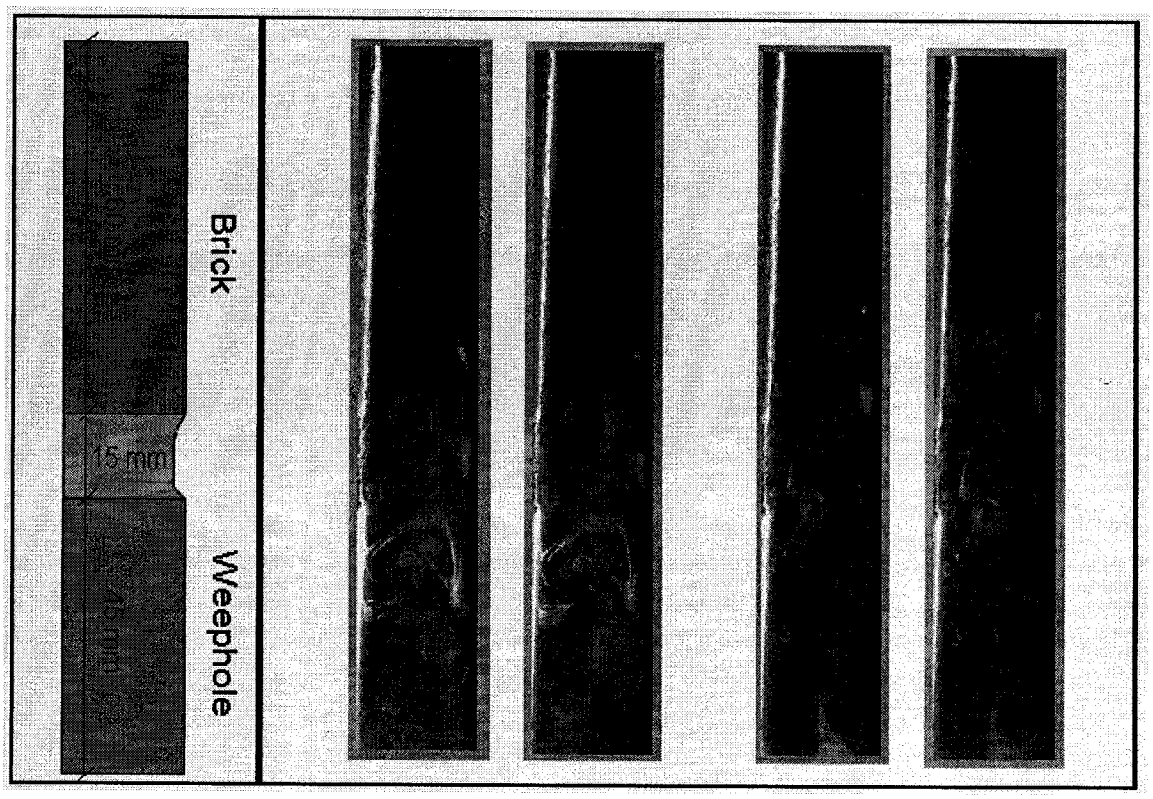

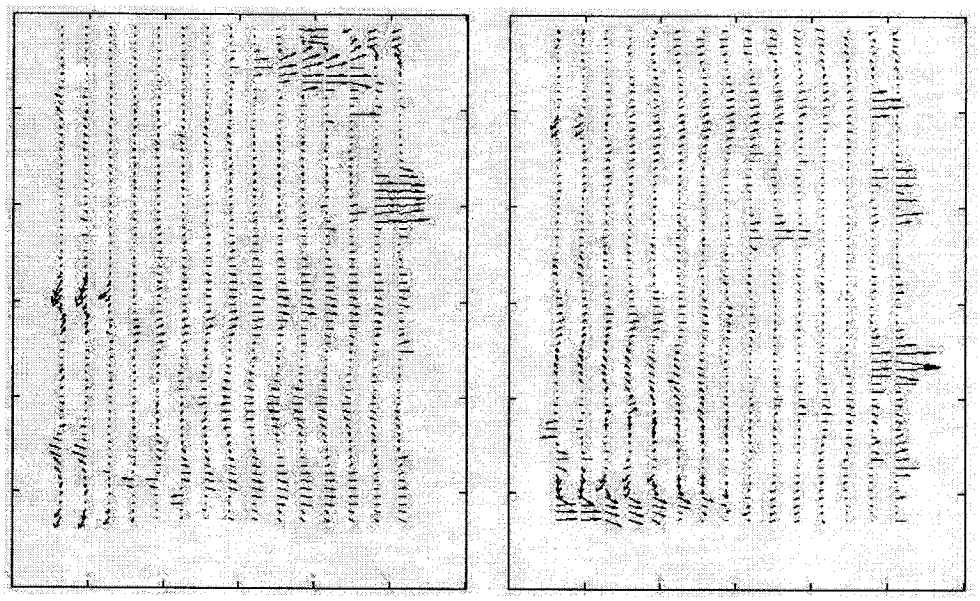

Table D.2: Test Period 2

4.0 Hours of Heat Lamp Exposure

	Exterior Brick	Interior Brick	Cavity Backwall
Surface Temperature	58.62°C	48.75°C	37.04°C

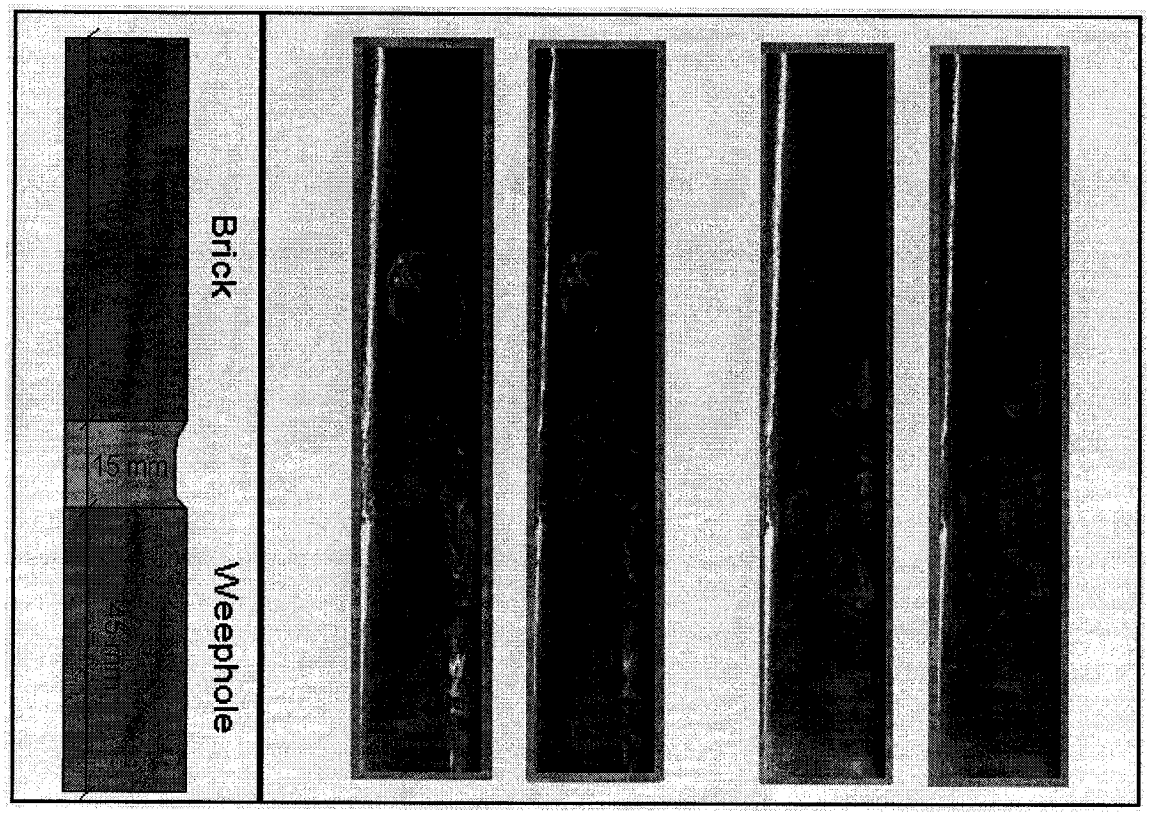

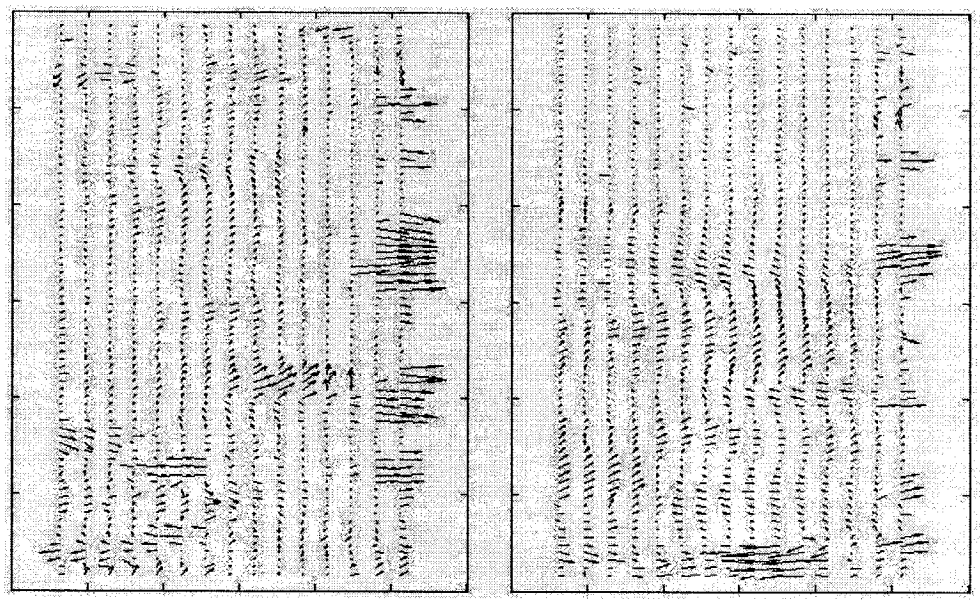

Table D.3: Test Period 3

5.0 Hours of Heat Lamp Exposure

	Exterior Brick	Interior Brick	Cavity Backwall
Surface Temperature	59.93°C	51.87°C	38.05°C

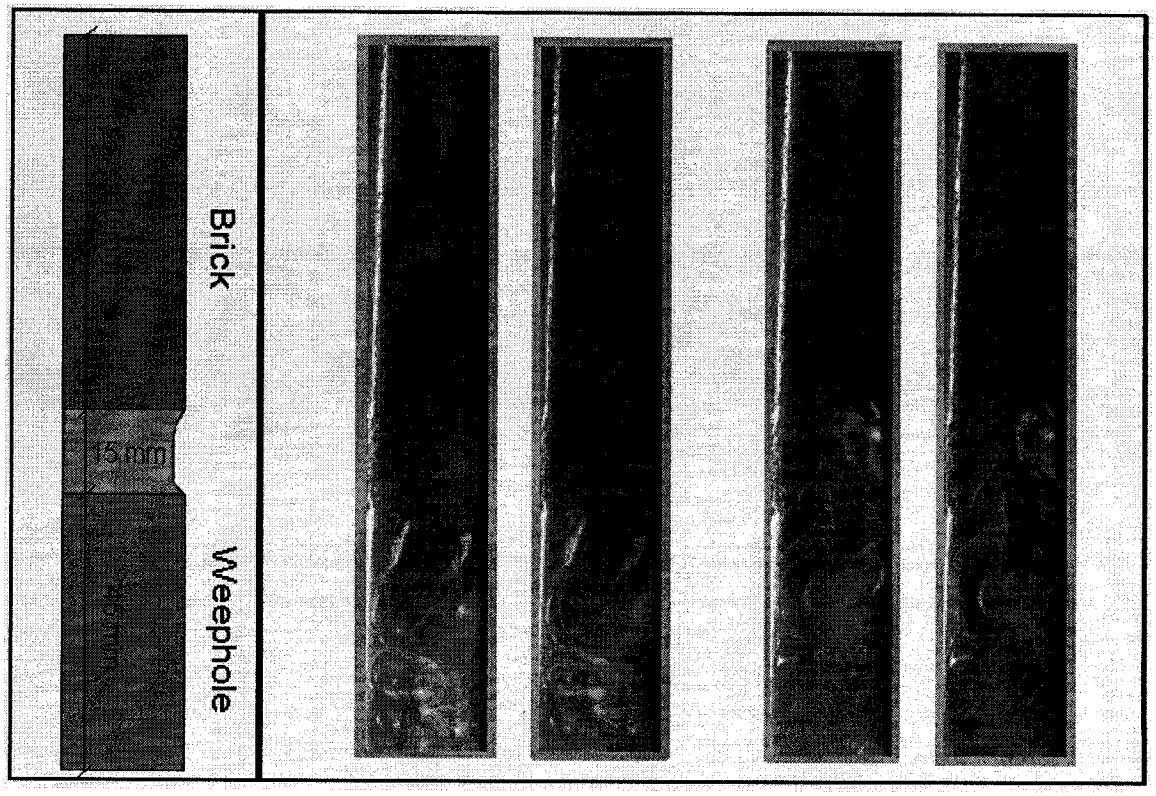

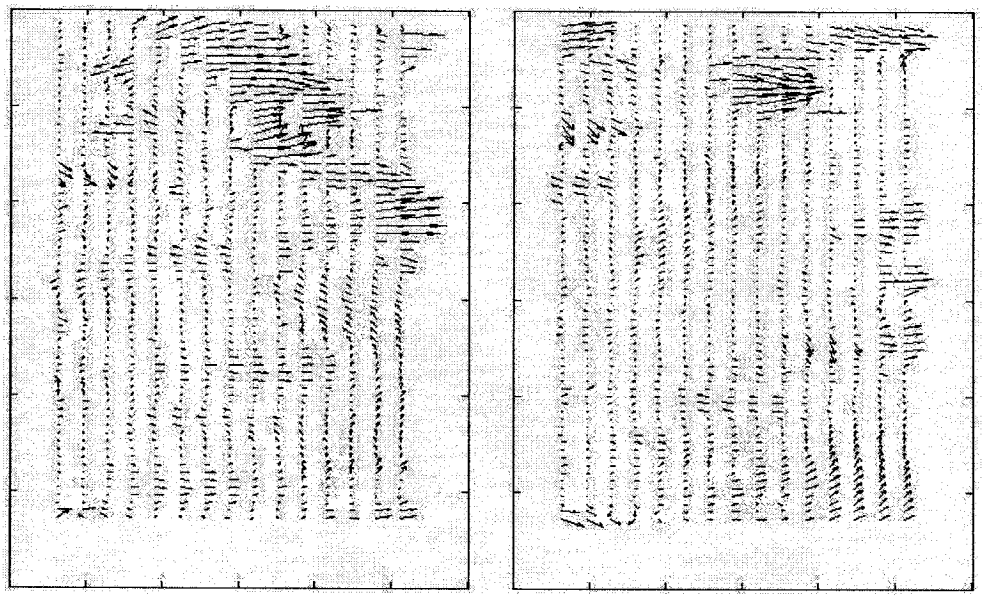

Table D.4: Test Period 4

6.0 Hours of Heat Lamp Exposure

	Exterior Brick	Interior Brick	Cavity Backwall
Surface Temperature	60.94°C	54.15°C	38.52°C

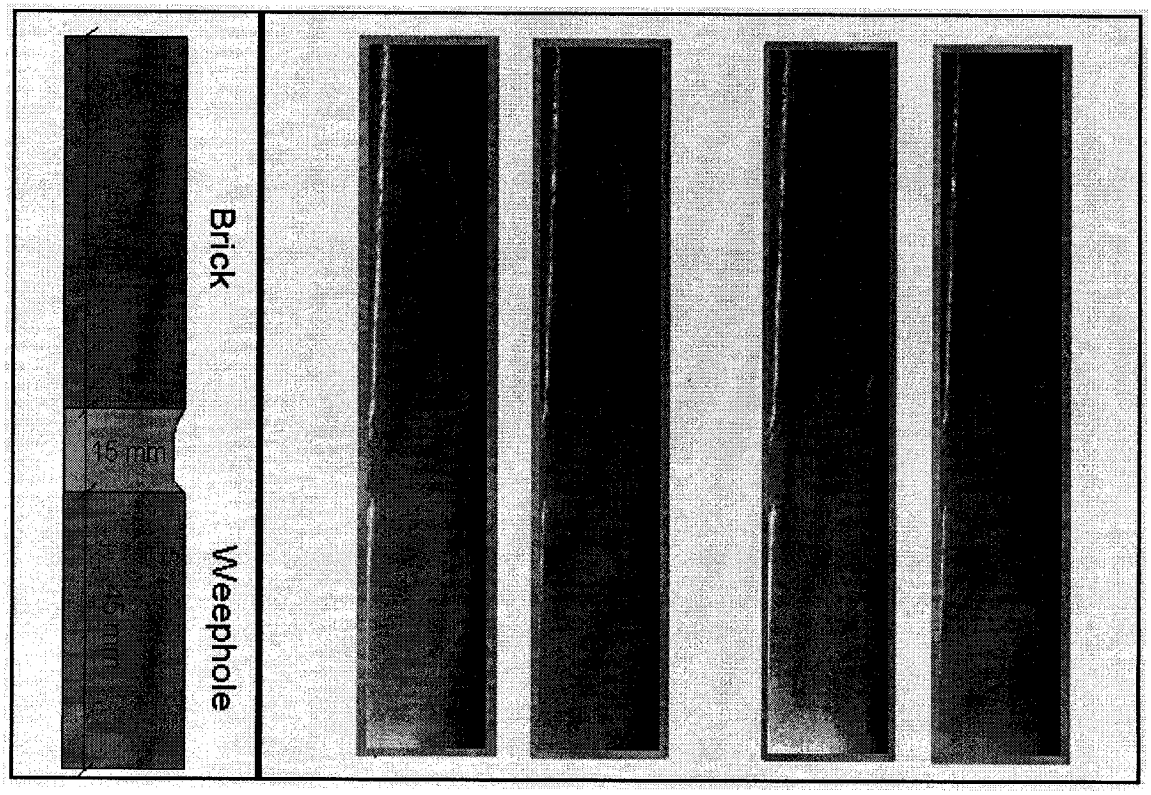

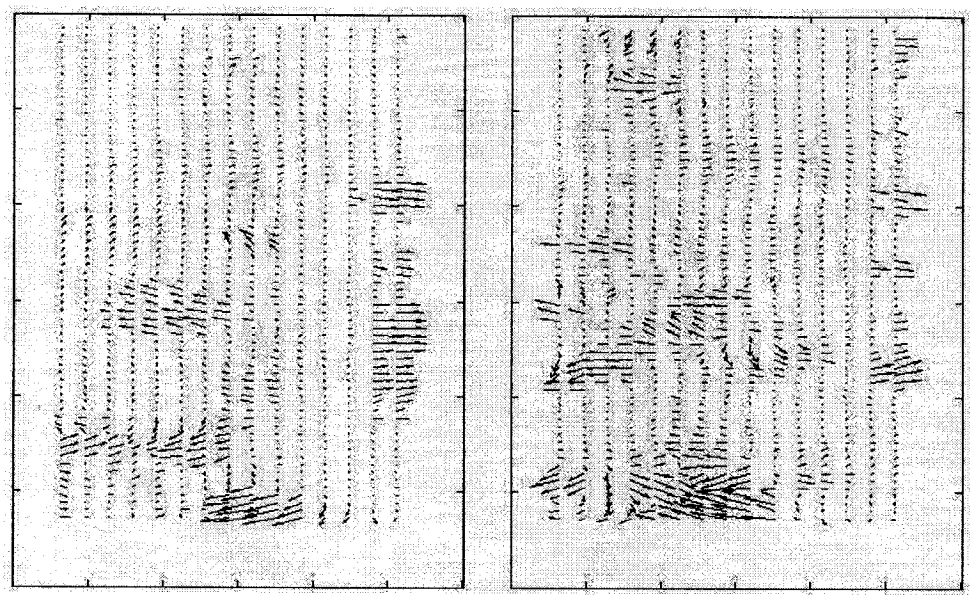

Table D.5: Test Period 5

7.0 Hours of Heat Lamp Exposure

	Exterior Brick	Interior Brick	Cavity Backwall
Surface Temperature	61.39°C	55.99°C	39.01°C

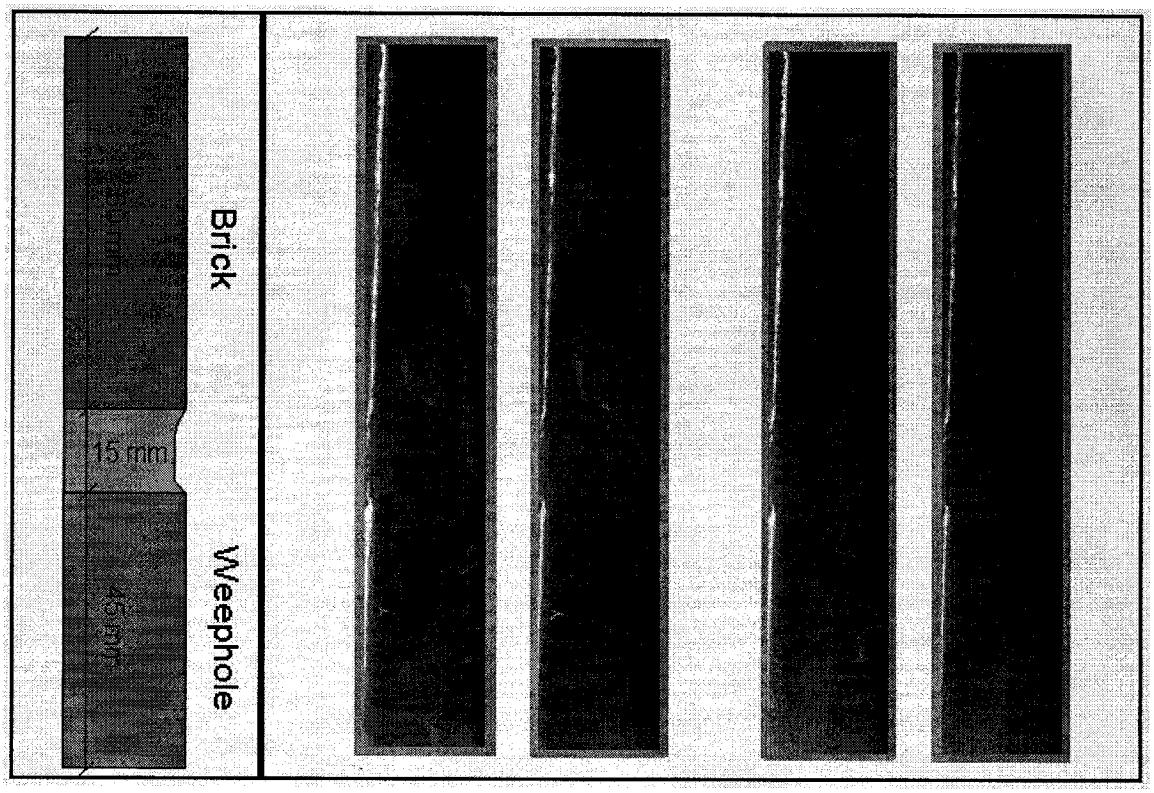

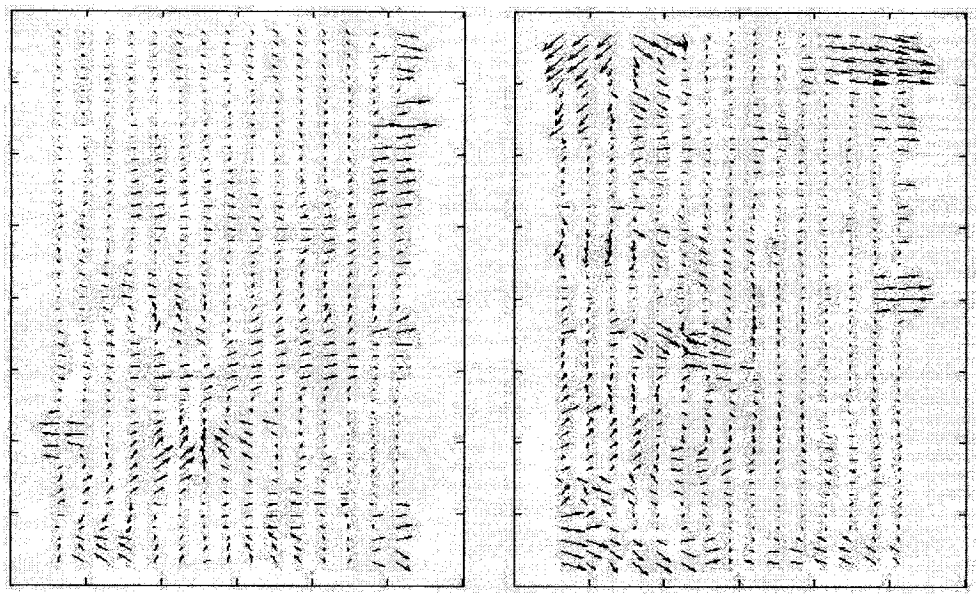

Appendix E

Surface Coefficient Experiment Results

Table E.1: Surface Coefficient Experimental Results for Test 1

Test #	Velocity [m/s]	Time [sec]	Air T [°C]	Air RH [%]	Air P [Pa]
1	0.20	10800	24.12	53.53	1611.97

Surface T [°C]	Surface RH [%]	Surface P [Pa]	ΔP [Pa]	ΔRH [%]
22.13	100.00	2670.40	1058.43	8.11

Brick #	Mass Loss [kg]	Gy [kg/s]	h_m [s/m]	h_{cv} [W/m^{2}K]
1	0.00216	2.000E-07	1.680E-08	2.156
2	0.00308	2.852E-07	2.395E-08	3.074
3	0.00339	3.139E-07	2.636E-08	3.383

Table E.2: Surface Coefficient Experimental Results for Test 2

Test #	Velocity [m/s]	Time [sec]	Air T [°C]	Air RH [%]	Air P [Pa]
2	0.20	10800	24.11	51.66	1554.45

Surface T [°C]	Surface RH [%]	Surface P [Pa]	ΔP [Pa]	ΔRH [%]
22.05	100.00	2656.77	1102.32	7.5

Brick #	Mass Loss [kg]	Gy [kg/s]	h_m [s/m]	h_{cv} [W/m^{2}K]
1	0.00219	2.028E-07	1.635E-08	2.099
2	0.00310	2.870E-07	2.315E-08	2.971
3	0.00335	3.102E-07	2.501E-08	3.210

Table E.3: Surface Coefficient Experimental Results for Test 3

Test #	Velocity [m/s]	Time [sec]	Air T [°C]	Air RH [%]	Air P [Pa]
3	0.10	10800	24.02	50.67	1516.45

Surface T [°C]	Surface RH [%]	Surface P [Pa]	ΔP [Pa]	ΔRH [%]
21.70	100.00	2600.65	1084.20	12.17

Brick #	Mass Loss [kg]	Gy [kg/s]	h_m [s/m]	h_{cv} [W/m^{2}K]
1	0.00238	2.204E-07	1.807E-08	2.319
2	0.00343	3.176E-07	2.604E-08	3.342
3	0.00335	3.102E-07	2.543E-08	3.264

Table E.4: Surface Coefficient Experimental Results for Test 4

Test #	Velocity [m/s]	Time [sec]	Air T [°C]	Air RH [%]	Air P [Pa]
4	0.05	10800	24.32	56.29	1715.21

Surface T [°C]	Surface RH [%]	Surface P [Pa]	ΔP [Pa]	ΔRH [%]
22.67	100.00	2758.79	1043.58	12.07

Brick #	Mass Loss [kg]	Gy [kg/s]	h_m [s/m]	h_{cv} [W/m^{2}K]
1	0.00221	2.046E-07	1.743E-08	2.237
2	0.00329	3.046E-07	2.595E-08	3.330
3	0.00327	3.028E-07	2.579E-08	3.310

Table E.5: Surface Coefficient Experimental Results for Test 5

Test #	Velocity [m/s]	Time [sec]	Air T [°C]	Air RH [%]	Air P [Pa]
5	0.15	10800	24.23	53.90	1633.55

Surface T [°C]	Surface RH [%]	Surface P [Pa]	ΔP [Pa]	ΔRH [%]
22.14	100.00	2671.37	1037.82	8.46

Brick #	Mass Loss [kg]	Gy [kg/s]	h_m [s/m]	h_{cv} [W/m^{2}K]
1	0.00212	1.963E-07	1.681E-08	2.158
2	0.00306	2.833E-07	2.427E-08	3.115
3	0.00322	2.981E-07	2.554E-08	3.277

Table E.6: Surface Coefficient Experimental Results for Test 6

Test #	Velocity [m/s]	Time [sec]	Air T [°C]	Air RH [%]	Air P [Pa]
6	0.25	10800	24.23	50.89	1542.33

Surface T [°C]	Surface RH [%]	Surface P [Pa]	ΔP [Pa]	ΔRH [%]
22.22	100.00	2684.41	1142.08	5.33

Brick #	Mass Loss [kg]	Gy [kg/s]	h_m [s/m]	h_{cv} [W/m^{2}K]
1	0.00205	1.898E-07	1.477E-08	1.896
2	0.00318	2.944E-07	2.292E-08	2.941
3	0.00344	3.185E-07	2.479E-08	3.182

Table E.7: Surface Coefficient Experimental Results for Test 7

Test #	Velocity [m/s]	Time [sec]	Air T [°C]	Air RH [%]	Air P [Pa]
7	0.20	21600	24.42	51.07	1565.49

Surface T [°C]	Surface RH [%]	Surface P [Pa]	ΔP [Pa]	ΔRH [%]
22.46	100.00	2723.86	1158.37	4.96

Brick #	Mass Loss [kg]	Gy [kg/s]	h_m [s/m]	h_{cv} [W/m^{2}K]
1	0.00623	2.884E-07	2.213E-08	2.841
2	0.00745	3.449E-07	2.647E-08	3.397
3	0.00778	3.602E-07	2.764E-08	3.547

Time [sec]	Brick #1 [g]	Brick #2 [g]	Brick #3 [g]
0	623.27	627.04	616.95
1800	622.11	625.75	615.78
3600	621.60	625.12	615.08
5400	620.96	624.40	614.23
7200	620.52	623.89	613.62
9000	620.11	623.39	613.05
10800	619.72	622.92	612.50
12600	619.34	622.44	611.97
14400	618.75	621.78	611.25
16200	618.25	621.24	610.61
18000	617.90	620.76	610.05
19800	617.43	620.15	609.59
21600	617.04	619.59	609.17

Time [sec]	Brick 1 [s/m]	Brick 2 [s/m]	Brick 3 [s/m]
1800	5.563E-08	6.187E-08	5.611E-08
3600	2.446E-08	3.021E-08	3.357E-08
5400	3.069E-08	3.453E-08	4.077E-08
7200	2.110E-08	2.446E-08	2.926E-08
9000	1.966E-08	2.398E-08	2.734E-08
10800	1.870E-08	2.254E-08	2.638E-08
12600	1.822E-08	2.302E-08	2.542E-08
14400	2.830E-08	3.165E-08	3.453E-08
16200	2.398E-08	2.590E-08	3.069E-08
18000	1.679E-08	2.302E-08	2.686E-08
19800	2.254E-08	2.926E-08	2.206E-08
21600	1.870E-08	2.686E-08	2.014E-08

Table E.8: Surface Coefficient Experimental Results for Test 8

Test #	Velocity [m/s]	Time [sec]	Air T [°C]	Air RH [%]	Air P [Pa]
8	0.10	3600	24.60	52.09	1614.03

Surface T [°C]	Surface RH [%]	Surface P [Pa]	ΔP [Pa]	ΔRH [%]
22.99	100.00	2812.77	1198.74	5.33

Brick #	Mass Loss [kg]	Gy [kg/s]	h_m [s/m]	h_{cv} [W/m^{2}K]
1	0.00126	3.500E-07	2.595E-08	3.331
2	0.00175	4.861E-07	3.605E-08	4.626
3	0.00169	4.694E-07	3.481E-08	4.468

Table E.9: Surface Coefficient Experimental Results for Test 9

Test #	Velocity [m/s]	Time [sec]	Air T [°C]	Air RH [%]	Air P [Pa]
9	0.20	3600	24.64	50.09	1555.77

Surface T [°C]	Surface RH [%]	Surface P [Pa]	ΔP [Pa]	ΔRH [%]
22.62	100.00	2750.44	1194.67	5.33

Brick #	Mass Loss [kg]	Gy [kg/s]	h_m [s/m]	h_{cv} [W/m^{2}K]
1	0.00078	2.167E-07	1.612E-08	2.069
2	0.00119	3.306E-07	2.459E-08	3.157
3	0.00114	3.167E-07	2.356E-08	3.024

Table E.10: Surface Coefficient Experimental Results for Test 10

Test #	Velocity [m/s]	Time [sec]	Air T [°C]	Air RH [%]	Air P [Pa]
10	0.30	3600	24.69	49.40	1538.92

Surface T [°C]	Surface RH [%]	Surface P [Pa]	ΔP [Pa]	ΔRH [%]
22.16	100.00	2674.63	1135.71	5.33

Brick #	Mass Loss [kg]	Gy [kg/s]	h_m [s/m]	h_{cv} [W/m^{2}K]
1	0.00084	2.333E-07	1.826E-08	2.344
2	0.00124	3.444E-07	2.696E-08	3.460
3	0.00121	3.361E-07	2.631E-08	3.376

Table E.11: Surface Coefficient Experimental Results for Test 11

Test #	Velocity [m/s]	Time [sec]	Air T [°C]	Air RH [%]	Air P [Pa]
11	1.00	3600	24.66	47.91	1489.83

Surface T [°C]	Surface RH [%]	Surface P [Pa]	ΔP [Pa]	ΔRH [%]
22.32	100.00	2700.79	1210.95	5.33

Brick #	Mass Loss [kg]	Gy [kg/s]	h_m [s/m]	h_{cv} [W/m^{2}K]
1	0.00092	2.556E-07	1.876E-08	2.408
2	0.00141	3.917E-07	2.875E-08	3.690
3	0.00139	3.861E-07	2.834E-08	3.637